

THE COLLAPSE OF HURRICANE FELICIA (2009)

A THESIS SUBMITTED TO THE GRADUATE DIVISION OF THE
UNIVERSITY OF HAWAI‘I AT MĀNOA IN PARTIAL FULFILLMENT
OF THE REQUIREMENTS FOR THE DEGREE OF

MASTER OF SCIENCE

IN

METEOROLOGY

DECEMBER 2014

By

Brandon P. Bukunt

Thesis Committee:

Gary M. Barnes, Chairperson
Yi-Leng Chen
Michael M. Bell

ACKNOWLEDGMENTS

I would like to first thank my parents Pete and Nancy for their endless support in helping me achieve my goals. Growing up in an ever-changing environment, from the east coast of the United States to a third-world country in South East Asia, exposed me to a diverse assortment of weather phenomena. I have no doubt that these unique opportunities molded me into the passionate atmospheric observer I am today. I would like to express more heartfelt thanks to the rest of my family; without your love and encouragement this accomplishment would not have been possible. I would also like to take this moment to thank my extended family and friends here in Hawai'i for the incredible camaraderie and rich, shared experiences.

With regard to academia, I would like to thank Dr. Gary Barnes for his guidance and punctual insight throughout this study of Hurricane Felicia. I cannot begin to express my gratitude for the countless hours he has spent with me ensuring I formulate my own conclusions and, ultimately, learn. I would also like to thank Dr. Michael Bell and Dr. Yi-Leng Chen for their advice and for serving on my thesis committee. I extend a warm thank you to my classmates for engaging discussions and assistance with programming. A special acknowledgement goes out to the Hurricane Research Division for the opportunity to explore a unique dataset in the eastern North Pacific, without which a detailed quantitative analysis of Felicia would have been unachievable.

ABSTRACT

In early August 2009 Hurricane Felicia threatened the Hawaiian Islands. The Central Pacific Hurricane Center in Honolulu requested NOAA to conduct synoptic scale surveillance missions around the hurricane to ascertain environmental winds, with the primary objective to improve the track forecast. The NOAA G-IV ferried out to the islands on 7 August and then conducted two circumnavigations, approximately 3-degrees latitude from the center of Felicia, on 8 and 9 August. During the ferry and the two subsequent circumnavigations, the G-IV crew deployed 72 Global Positioning System dropwindsondes (GPS sondes). Over these 3 days Felicia collapsed, with a minimum central pressure rising from 955 to 995 hPa.

The GPS sondes jettisoned from above 200 hPa provide a rare opportunity to investigate the role of two environmental factors that impact hurricane intensity, the vertical shear of the horizontal wind (VWS) and the presence of dry air in the midlevels. Near the Hawaiian Islands at this time of year climatological studies reveal that there is a tropical upper tropospheric trough (TUTT) which alters the location and strength of the subtropical jet stream (STJ). The STJ produces a region with strong VWS often located near or over the islands, and is thought of as the primary “defense” against strong landfalling hurricanes approaching from the east. The sea surface temperature (SST) gradients are aligned north-south and thus have far less impact on intensity than is commonly thought.

The GPS sondes are used to map the location of the TUTT and the STJ relative to the hurricane. The dataset allows me to determine when the STJ first interacts with the anticyclonic outflow channels of Felicia, and subsequently I can estimate when the STJ

reaches the inner core of the hurricane. The GPS sondes deployed in the circumnavigation portions of the two flights are also used to examine the role of dry midlevel air associated with the Pacific High. Midlevel relative inflow is too weak for this air to have an impact. Ultimately, this study reveals that the G-IV reconnaissance flights are useful for forecasts of intensity change, in addition to their proven value for track forecasts.

TABLE OF CONTENTS

Acknowledgements.....	ii
Abstract.....	iii
List of Tables	vii
List of Figures.....	viii
CHAPTER 1: INTRODUCTION.....	1
1.1 Tropical Cyclone Decay	1
1.2 G-IV Synoptic Surveillance.....	2
1.3 Sea Surface Temperature	3
1.3.1 Maximum Potential Intensity (MPI).....	4
1.4 The Effects of Cooler, Drier, Midlevel Air.....	5
1.5 Vertical Shear of the Horizontal Wind	6
1.6 The Tropical Upper Tropospheric Trough (TUTT).....	7
1.6.1 The TUTTs Influence on TC Intensity	8
1.7 Objectives	9
CHAPTER 2: DATA	11
2.1 Aircraft Utilized and Missions.....	11
2.2 GPS Dropwindsonde Instrumentation and Deployment.....	11
2.3 Estimating Sea Surface Temperatures	13
2.4 NCEP CFSR Fields.....	13
2.5 Satellite Imagery and Satellite Derived Products	13
CHAPTER 3: METHODOLOGY	15
3.1 Processing of GPS Sonde Data: ASPEN and Beyond.....	15
3.2 Analysis with the Sonde Data	17
3.2.1 Calculating Storm Relative Winds and Thermodynamic Variables ...	19
3.2.2 Calculating VWS, Divergence, and Vorticity.....	19
3.2.3 Circumnavigated Analysis Levels	20

CHAPTER 4: RESULTS	22
4.1 Formation and Intensification- Attendant Conditions	22
4.2 Actual Intensity versus Maximum Potential Intensity.....	24
4.3 SSTs and the Initial Decay.....	25
4.4 Outflow Channel Enhancement	25
4.4.1 Is the STJ Responsible for Felicia’s Re-Intensification?.....	26
4.5 Basic G-IV Analyses.....	28
4.6 Subcloud Layer Fields	30
4.7 Evidence of Dry Air Entrainment in the Midlevels.....	33
4.8 Evidence of the STJ’s Intrusion into the Inner Core.....	34
4.8.1 Quantifying the STJ’s Intrusion into the Inner Core	36
4.9 SHIPS Shear Evaluation of Felicia	37
 CHAPTER 5: CONCLUSIONS AND FUTURE WORK.....	 39
5.1 Summary and Discussion.....	39
5.2 Future Work.....	45
 TABLES	 48
 FIGURES	 49
 REFERENCES	 91

LIST OF TABLES

<u>Table</u>	<u>Page</u>
1. GPS dropwindsondes launched during the G-IV synoptic surveillance flights of Hurricane Felicia on 7-9 August 2009	48

LIST OF FIGURES

<u>Figure</u>	<u>Page</u>
1. The NOAA Gulfstream IV-SP (G-IV) Aircraft	49
2. NOAA G-IV mission in the Atlantic basin during TS Bonnie in July 2010.....	50
3. Schematic diagram demonstrating mean TC motion in the western North Pacific basin based upon composites of rawinsondes	51
4. Evaluation of the minimum attainable central pressure of a TC as a function of the surface air temperature and the weighted mean outflow temperature near the tropopause.....	52
5. Streamline analysis of mean flow at 200 hPa near the Hawaiian Islands during the month of August based on cloud-drift winds and upper air observations.....	53
6. Tropical upper tropospheric trough interaction with the anticyclonic outflow of a TC	54
7. Average August 850-200 hPa VWS values in $m\ s^{-1}$ from 1966-2005	55
8. NOAA G-IV surveillance mission of Felicia on 7 August 2009 and chronological deployment distribution of GPS sondes	56
9. NOAA G-IV surveillance mission of Felicia on 8 August 2009 and chronological deployment distribution of GPS sondes	57
10. NOAA G-IV surveillance mission of Felicia on 9 August 2009 and chronological deployment distribution of GPS sondes	58
11. Schematic diagram of the NCAR GPS dropwindsonde used during the G-IV surveillance missions of Hurricane Felicia	59
12. Example of a sensor wetting correction on a skew-T log-P diagram processed with ASPEN from 8 August deployment #11	60
13. Example of a layer of a skew-T log-P diagram demonstrating a slight departure from a saturated profile	61
14. The NHC's best track of Hurricane Felicia with center positions every 6 hours	62

15. VWS overlaid on GOES-WEST IR satellite imagery at 0900 UTC 6 August ...	63
16. NCEP CFSR total atmospheric precipitable water at 0000 UTC 7 August 2009	64
17. GOES-WEST 0000 UTC 6 August 2009 visible satellite imagery and 0600 h forecasted GFS model overlay of sea level pressure and winds	65
18. The evolution of Hurricane Felicia’s central pressure based on three approaches; NHC’s best track, CIMSS Advanced Dvorak Technique, and MPI theory	66
19. NOAA OIV2 weekly averaged satellite derived SSTs beginning 0000 UTC 5 August 2009 for the domain 180°W to 120°W, 0°N to 30°N	67
20. Color enhanced IR satellite imagery of Hurricane Felicia from 1500 UTC 7 August to 0000 UTC 8 August	68
21. Visible satellite imagery of Hurricane Felicia at 1800 UTC 7 August	70
22. GOES-WEST water vapor imagery at 2100 UTC 7 August and GFS 0900 h forecasted GFS model overlay of 250 heights and winds	71
23. NCEP CFSR 250 hPa winds at 1800 UTC 7 August 2009 with overlay of “separation distance” methodology	72
24. Separation distance and Felicia’s central pressure measured by CIMSS ADT as a function of time	73
25. Layer averaged vertical profiles of θ_e on 8-9 August for the environment to the NW of Felicia and the circumnavigations	74
26. Divergence associated with the 3-degree circumnavigation of Felicia	75
27. Relative vorticity associated with the 3-degree circumnavigation of Felicia	76
28. Storm relative tangential and radial flow along circumnavigation at 975 hPa	77
29. θ_e values along circumnavigation at 975 hPa	78
30. IR satellite image of Hurricane Felicia at 0900 UTC 8 August	79

31. Storm relative radial flow and θ_e at 700 hPa	80
32. NCEP CFSR 250 hPa winds for 1200 UTC 7 August, 1200 UTC 8 August, and 1200 UTC 9 August	81
33. GPS sonde measured storm relative wind flow at 200 hPa during the G-IV missions on 8 and 9 August	83
34. Storm relative tangential and radial flow along circumnavigation at 250 hPa	84
35. θ_e along circumnavigation at 250 hPa	85
36. VWS along circumnavigation from 850-225 hPa	86
37. IR satellite image of Hurricane Felicia at 1200 UTC 9 August	87
38. Evolution of the spatial extent (degrees ²) of cloud top temperatures less than -50°C associated with Felicia from 0000 UTC 8 August through 1800 UTC 9 August.	88
39. IR and visible satellite imagery of Hurricane Felicia at 0900 UTC 9 August and 1600 UTC 9 August, respectively	89
40. SHIPS 0-96 h forecasts for Hurricane Felicia 1200 UTC 6-9 August	90

CHAPTER 1

INTRODUCTION

1.1 Tropical Cyclone Decay

Although there are countless studies on the intensification of tropical cyclones (TCs), there has been little research on their decay. From an economic perspective, investigation of the decay of a TC is just as important. As an example, with coastal populations continuing to experience tremendous growth, accurate estimations of TC intensity are crucial to both economy and human life; if a given TC is accurately modeled to weaken substantially, millions of dollars can be saved in disaster mitigation and allow for a continuation of economic productivity. With TC decay in mind, the necessary but not sufficient ingredients for TC formation are reversed in order to reflect the investigation of a given TCs collapse. Therefore, TC intensity change may be defined as the deepening or filling of the central sea-level pressure, or an increase or decrease in the sustained wind speeds within the eyewall of the TC.

With regard to this paper, the rapid intensification of Hurricane Felicia (2009) to a category 4 hurricane in the eastern North Pacific basin prompted the National Oceanic and Atmospheric Administration (NOAA) and the Central Pacific Hurricane Center (CPHC) to mobilize the primary upper-level observational platform, the NOAA Gulfstream IV-SP (G-IV). Arriving soon after the maximum intensification stage of Felicia, the G-IV's in-situ sampling of Felicia on three consecutive days provides the rare opportunity to quantitatively assess environmental factors that may have contributed to the decay of a TC in the eastern and central North Pacific basin.

1.2 G-IV Synoptic Surveillance

As highlighted by Avila (1998) and Rogers et al. (2006), a fundamental reason for only subtle improvements in the accurate prediction of TC intensity change is insufficient observation networks. This issue is particularly true for the eastern and central North Pacific, where in-situ measurements and aircraft surveillance are both temporally and spatially limited. In fact, the rawinsondes launched from Hilo and Lihue in the Hawaiian Islands are the only consistent observations for the central and eastern North Pacific basin. Furthermore, the meager upper-level observation network results in a poor representation of upper-level troughs, features which may influence the intensity of TCs.

In order to fill a fragment of the much needed in-situ TC observations, the NOAA G-IV conducts synoptic surveillance missions around TCs as part of operational support for the National Hurricane Center (NHC) and CPHC (Fig. 1). The G-IV releases Global Positioning System dropwindsondes (GPS sondes) to attain vertical profiles of the atmosphere from a flight level of ~150 hPa to the surface. Such complete vertical profiles ensure the entire steering flow of the atmosphere is captured, thereby improving a TC's forecasted track. A typical G-IV flight mission involves sampling the synoptic environment in which the TC is expected to track towards, and then flying a circumnavigation around the storm at a radial distance of ~333 km (or 3-degrees latitude) (Fig. 2). Circumnavigation at this distance is a customary approach due to the results of comprehensive rawinsonde or dropwindsonde composite studies by Gray (1989) and Franklin (1990). Specifically, Gray (1989) used rawinsondes to calculate and present the differences of the storm motion relative to a steering flow layer of 850-350 hPa (Fig. 3). Using a variety of storm characteristics such as size, intensity, track direction, and storm

basins, the 2-4° latitudinal radial band showed the best overall agreement with storm motion. As a result, these tactical flight missions are conducted in both the Pacific and Atlantic basins with the primary objective to improve TC track. Specifically, a small portion of the invaluable G-IV data, in the form of quality controlled TEMP-DROP messages, is sent in real-time to both the National Centers for Environmental Prediction (NCEP) and NHC to be ingested into global and smaller-scale hurricane model runs. TC track forecast errors have improved 16-30% in the Atlantic basin through the implementation of these synoptic surveillance missions (Burpee et. al 1996).

1.3 Sea Surface Temperature

It is widely acknowledged that a necessary but not sufficient criterion for the development and maintenance of a TC is the transfer of energy from the warm tropical oceans to the atmospheric boundary layer (Miller 1958). Palmén (1948) established a minimum sea surface temperature (SST) threshold of 26°C in which overlying convection may develop into a TC. This minimum threshold for TC formation and maintenance has since been revised to 26.5°C, and is referenced throughout the literature (e.g., Gray 1968; Dengler 1997; Zhang 1993). Dare and McBride (2011) performed a statistical analysis of SST thresholds, and determined that 99.5% of TCs form above 25.5°C during a 24 h period, however, when a maximum SST is determined from a 48 h period 26.5°C is a more appropriate threshold value for cyclogenesis. Although there has been substantial research into the SSTs needed for TC formation, there has been little investigation into a SST threshold required for the maintenance of a TC. The lack of research into a SST decay threshold is compounded by the fact that as a TC induces wind stress on the ocean surface, it upwells cooler water through shear-induced mixing. Therefore, knowledge of

the vertical structure of the upper ocean, and not simply SST, is crucial in order to assess the heat fluxes ingested into a TC. Cione and Uhlhorn (2003) investigated changes in inner-core SST via Airborne Expendable BathyThermographs (AXBTs), ultimately concluding that even small changes in the inner-core SST may have a profound impact on the intensity change process a given TC undergoes. However, the general guideline is that if a TC crosses into water with a SST less than 26.5°C, the TCs intensity is adversely affected. It is important to reiterate that SST is simply one of several factors with regard to cyclogenesis; a given SST is relative to the other environmental parameters which, as a whole, create the necessary but not sufficient conditions for TC formation and maintenance.

Based upon the National Center for Environmental Prediction (NCEP) and National Center for Atmospheric Research (NCAR) reanalysis datasets, the climatological SST gradients in the eastern and central North Pacific are generally zonal, with the aforementioned SST threshold of 26.5°C at roughly 16-17°N. These SST fields are beneficial for a TC to maintain its intensity on a westward heading. Contrarily, a TC tracking toward the NW will cross over diminishing SSTs and suffer a sudden loss of ocean thermal energy. (Additional details about SST fields are discussed in the Data section to follow).

1.3.1 Maximum Potential Intensity (MPI)

Emanuel (1986) proposed the notion that a TC may operate akin to a simple Carnot heat engine in which latent and sensible heat are drawn from the near sea surface inflow layer at a temperature (T_s), and disposed in the upper-level outflow at a cold temperature (T_{out}). In short, the angular momentum of a given TC is treated as a function

of moist enthalpy. Therefore the thermodynamic efficiency of the atmosphere equivalent to that of a Carnot cycle is then $(T_s - T_{out})/T_s$. In this relationship, the lowest achievable surface pressure (TC deepening) increases with thermodynamic efficiency (Fig. 4). With this chart, the maximum potential intensity (MPI) of a TC can be estimated solely by the temperature near the surface (T_s) and the temperature at the tropopause (T_{out}). It is prudent to mention that this MPI methodology does not take into account entrainment of dry air or vertical shear of the horizontal wind (VWS). More recent work by Tang and Emanuel (2012) has considered the influence of environmental VWS and low entropy air in the midlevels alongside potential intensity by means of a ventilation index.

1.4 The Effects of Cooler, Drier, Midlevel Air

High amounts of midlevel moisture are beneficial for TC formation, intensification and maintenance (Malkus and Riehl 1960; Miller 1964; Gray 1968; McBride and Zehr 1981; Nolan 2007). Moreover, it is widely understood that the entrainment of dry air is detrimental to TC development and intensity (Dunion and Velden 2004; Wu 2007; Braun 2010). The presence of dry air can manifest and entrain into a TC core (henceforth “core” is defined as the region from the radius of maximum winds (RMW) to the center of circulation) in two known ways. The intrusion of environmental air associated with VWS may advect cooler, drier air into a TC (Simpson and Riehl 1958; Marin et al. 2009). Dolling and Barnes (2014) show how entrainment of dry air in the midlevels reduces the equivalent potential temperature (θ_e) of the eyewall column. Secondly, Barnes et al. (1983) and Powell (1990) used boundary layer aircraft observations to demonstrate that convective downdrafts within the TC itself can feasibly carry cooler and drier θ_e air to the surface that later may be ingested by the eyewall. Shu

and Wu (2009) assessed the impact of dry air, concluding that a TC will tend to weaken when dry air is within 380 km from the storm center. Contrarily, both observational studies by Dolling and Barnes (2014) and numerical simulations by Braun et al. (2012) highlighted that environmental dry air can only affect TC intensity when it is located proximate to the RMW.

Climatologically, the eastern and central Pacific basin is regulated by deep high pressure known as the Pacific High. Subsidence emanating from the Pacific High results in substantially lower moisture above the tradewind inversion. This dry air may negatively impact TC intensity. Thermodynamic profiles in the eastern and central North Pacific will be presented in the results section.

1.5 Vertical Shear of the Horizontal Wind

The environmental VWS is generally recognized to adversely affect the development and maintenance of a given TC (McBride and Zehr 1981; Zehr 1992). The environmental VWS acts to tilt the TC, thereby causing asymmetries in the overall structure. This alteration to a TC's overall structure may create the proper conditions for lower θ_e air associated with convective downdrafts to flush the inflow layer, and subsequently intrude and dilute the high θ_e surplus residing in the TC core (Powell 1990; Riemer et al. 2010; Tang and Emanuel 2012). Statistically, VWS is negatively correlated with TC deepening (DeMaria 1996; Gallina and Velden 2002). This strong statistical relationship between VWS and intensity clearly supports the prevalence of VWS as a predictor in various hurricane models such as the Statistical Hurricane Intensity Prediction Scheme (SHIPS) (DeMaria and Kaplan 1994).

During the summer months, the Hawaiian Islands reside just south of the axis of the North Pacific's tropical upper tropospheric trough (TUTT). The combination of the upper-level westerlies and lower level easterlies generates a climatological 850-200 hPa VWS of 22 m s^{-1} in the vicinity of Hawai'i during August (Fig. 7). Additionally, a strong climatological VWS gradient lies just southeast of the islands from 150°W to 140°W , with VWS trending from 18 m s^{-1} to less than 10 m s^{-1} respectively. The climatological "bull's-eye" of VWS over the Hawaiian Islands is thought of as the primary "defense" against strong landfalling TCs approaching from the east.

1.6 The Tropical Upper Tropospheric Trough (TUTT)

A TUTT, first described by Sadler (1967), is an upper-level trough which dominates the tropical oceanic basins during the summer months. In the North Pacific basin, the TUTT extends east-northeast to west southwest from roughly $35^{\circ}\text{N } 130^{\circ}\text{W}$ in the eastern Pacific to $\sim 15^{\circ}\text{N } 140^{\circ}\text{E}$ in the western Pacific. The TUTT was first identified by Sadler while constructing 200 and 300 hPa maps of wind climatology over the tropical oceans (Fig. 5). Although this digital version of Sadler's original 200 hPa streamline analysis of the central and eastern North Pacific is based on limited upper-level aircraft observations and cloud drift winds, its existence and coverage has been confirmed via model analyses and more current satellite products. The presence of the TUTT alters the location and strength of the subtropical jet (STJ). In the North Pacific, the STJ is characterized by a climatological westerly wind maximum of roughly 15 m s^{-1} located above the Hawaiian Islands.

1.6.1 *The TUTTs Influence on TC Intensity*

Proper evaluation of the strength, timing, and location of upper-level flow fields with respect to a given TC remains a prominent issue when forecasting TC intensity (Shieh et al. 2013). This is due in part to the near neutral inertial stability of the atmosphere near the tropopause of a TC, which allows environmental air to modulate the TC environment in the upper-levels (Holland and Merrill 1984). Specifically, case studies support the relationship of eddy flux convergence of angular momentum and TC intensity change (McBride and Zehr 1981; DeMaria et al. 1993; Bosart et al. 2000). Sadler (1967, 1976, 1978) proposed that a properly oriented TUTT cell to the N/NW of a TC can act to kick start or intensify the TC by enhancing one of the TC's upper-level outflow channels (Fig. 6). Such a configuration allows excess mass and heat associated with the TC's convection to be exhausted outward via an outflow channel in the northern sector and carried eastward by the large-scale westerly flow. Patla et al. (2009) highlight that a TUTT's separation distance, orientation, and intensity in relation to a TC are critical in determining the likelihood of a TUTT influencing the motion of a TC. One can deduce that this conclusion also applies to intensification.

Although the heightened wind zone associated with a TUTT cell may intensify a TC by enhancement of an upper-level outflow channel, the STJ may also boost the VWS to unfavorable levels for a TC once the strong upper-level flow reaches the inner core. Chen and Chou (1994) concluded that roughly 90% of TUTT cells are characterized by jet streaks of 20-30 m s⁻¹. Additionally, the southeastern sector of a TUTT cell is typically the strongest relative to the rest of the circulation due to merging with upper-level westerlies and the STJ as previously mentioned.

1.7 Objectives

According to NOAA's Hurricane Research Division (HRD), there have only been four TC-related G-IV deployments in the Pacific basin through 2009, and the G-IV synoptic surveillance missions conducted around Felicia (2009) were the most comprehensive. What follows is an investigation of the 65 successful sondes jettisoned from the G-IV during three consecutive days of synoptic surveillance on 7 to 9 August 2009. This is an unprecedented dataset with regard to in-situ observations around a TC in the data sparse region of the central and eastern North Pacific. The overall objective is to shed light on Felicia's rapid collapse, and determine the value of the G-IV circumnavigated flight route from an intensity standpoint. Satellite imagery and reanalysis data will also be used. I examine the following questions, with a focus on the value of the three consecutive days of G-IV data during the decay of Felicia.

- (1) Is there an indication of dry air being imported within the boundary layer or in the midlevels as evidenced by a combination of the relative radial flow and θ_e fields along the 3-degree circumnavigation from 8-9 August?
- (2) What is the role of the TUTT as a TC approaches? Is Sadler's assertion that a TUTT may contribute to TC intensification exemplified with Felicia?
- (3) Can the timing of the STJs intrusion into the inner core of Felicia be determined based on the winds observed along the circumnavigations performed on 8-9 August? What is the evolution of VWS along the circumnavigation?

(4) How successful is the 3-degree circumnavigation at determining factors contributing to the decay of Felicia? What are the advantages and disadvantages of utilizing a 3-degree circumnavigation for intensity forecasting?

CHAPTER 2

DATA

2.1 Aircraft Utilized and Missions

On 7 August 2009, the NOAA G-IV aircraft departed Long Beach, California to conduct a 3-day synoptic surveillance of Hurricane Felicia in the eastern North Pacific at a flight level of 150 hPa. During the ferry out to the Hawaiian Islands on 7 August, the G-IV deployed GPS sondes to the N and NW of the forecasted cyclone track (Fig. 8). The duration of the flight on the 7th was 5.05 h while an average of 6.85 h was invested on 8 and 9 August. On the 8th and 9th the G-IV sampled the synoptic environment to the W/NW of the TC, and then performed a circumnavigational surveillance of Felicia at a distance approximately 3-degrees latitude from the circulation center (Figs. 9 and 10).

2.2 GPS Dropwindsonde Instrumentation and Deployment

NCAR spearheaded the development and implementation of the GPS sonde. As highlighted by Hock and Franklin (1999), GPS sonde improvements over the ODW include global operation at altitudes up to 24 km, simultaneous operation of up to four sondes per aircraft, a narrow RF transmission bandwidth of < 20 kHz, telemetry range of 325 km, sonde descent time of ~12 min when released from 12 km, sensor measurement rate of 2 Hz, and a shelf life of at least 3 years (Fig. 11).

The GPS sondes incorporate a Barocap, H-Humicap, and Thermocap for the pressure, humidity, and temperature sensors, respectively. The Thermocap, developed by Vaisala, produces a consistent, noticeable response lag in the sondes temperature measurements that are corrected in the data processing stage. For wind estimates the sonde has a GPS receiver that records the relative Doppler frequencies from the GPS

satellite. These Doppler frequencies describe the motion of the sonde relative to the satellite. After being digitized, the Doppler frequencies are then sent back to the aircraft to be converted into winds via the aircraft data system.

GPS sondes are characterized by a 2 Hz sampling rate which translates to a vertical resolution of 12-14 m at 200-300 hPa and ~5-7 m resolution in the lower troposphere. In field accuracy is not as accurate as the manufacturer specifications, with typical errors of pressure, temperature, humidity evaluated at 1.0 hPa, 0.2°C, <5%, and 0.5 m s⁻¹, respectively. Due to GPS technology, the vertical resolution of wind measurements are ~6 m, an exceptional advancement from the ODWs ~ 150 m vertical resolution. Moreover, GPS allows the sonde to measure winds to the surface, whereas ODW measurements were often missing below 400 m. The accuracy error of the humidity sensor is an important consideration when analyzing skew-T log-P profiles near saturation. Sensor wetting, as presented in the following chapter, is also an issue that can be remediated sometimes by techniques outlined by Bogner et al. (2000) and Barnes (2008).

Over the course of the 3-day G-IV synoptic surveillance 73 GPS sondes were deployed with a success rate of 90% (Table 1). This success rate refers to whether or not vertical atmospheric soundings were achieved at the deployment locations. One aspect of Table 1 that is particularly noteworthy is that the sondes deployed along the circumnavigated portion of the flight exhibited a 100% success rate on the 8th, and 78% for the 9th. At first glance this may appear to be a significant disadvantage from an analysis point-of-view, however the trends around the 9th circumnavigation are consistent and an absent sounding can be interpolated from the data obtained by adjacent sondes.

2.3 Estimating Sea Surface Temperatures

The Optimum Interpolation (OIV2) SST fields generated by NOAA are used for the analysis of Felicia. The SST fields are produced weekly on a one-degree grid and merge buoy, ship, satellite SST data, and SSTs simulated by sea-ice coverage. The root mean square (RMS) monthly error associated with these SST fields is $\sim 0.8^{\circ}\text{C}$. Before the SST field is completed, the satellite SST fields are adjusted for biases as suggested by Reynolds (1988) and Reynolds and Marsico (1993). Since the weekly OIV2 SST analysis is centered on each Wednesday, the week of 5-12 August 2009 is chosen for the SST analysis of Hurricane Felicia.

2.4 NCEP CFSR Fields

In order to describe the large-scale environment surrounding Felicia when the G-IV was not in flight, NCEP Climate Forecast System Reanalysis (CFSR) fields are utilized. This global, high resolution reanalysis product was established in order to generate the best estimate of the coupled ocean-atmosphere system. CFSR incorporates all applicable traditional and satellite observations, but with a significantly finer atmospheric resolution of ~ 38 km. The G-IV's GPS sonde TEMPDROPS are included in CFSR, therefore greater confidence can be placed on the reanalysis fields during the G-IV sampling periods. CFSR produces a wide variety of variables that are available four times daily. Specifically, the upper-level wind fields and atmospheric column precipitable water are employed.

2.5 Satellite Imagery and Satellite Derived Products

Various satellite imagery products are employed before, during, and after the G-IV sampling periods. Evolution of the Geostationary Operational Environmental

Satellites- (GOES) West infrared (IR), visible, and water vapor channels are used to assess the intensity of Felicia as determined by cloud organization, intensity of convection, and synoptic flow regimes in the vicinity of Felicia. Observations from various polar orbiting satellite sensors, particularly the 85 GHz Horizontal channel, are also utilized to gauge the intensity of Felicia. The 85 GHz frequency band is sensitive to scattering of radiation by large ice typically found in deep convection. Cooperative Institute for Meteorological Satellite Studies (CIMSS) satellite imagery overlays and model analyses are also incorporated. In August 2009, CIMSS employed the Naval Operational Global Atmospheric Prediction System (NOGAPS) analyses as the background fields for their local TC analyses. Atmospheric Motion Vector (AMV) fields, generated by sequences of geostationary satellite imagery, are also incorporated in the analyses and provide data for observation deficient regions such as the Pacific basin.

CHAPTER 3

METHODOLOGY

3.1 Processing of GPS Sonde Data: ASPEN and Beyond

Data from the GPS sondes are first received and processed by the research aircraft through the onboard Airborne Vertical Atmospheric Profiling System (AVAPS).

Afterwards the data are processed through the Atmospheric Sounding Processing Environment (ASPEN) program (Martin 2007) which runs the raw AVAPS files through a series of quality control (QC) algorithms in order to revise or omit unrepresentative data. ASPEN processes pressure, temperature, humidity, and winds individually. The winds are decomposed into u and v components. In particular, the ability to compute the component winds depends on the number of acquired satellites during both the initial deployment and subsequent descent of each sonde. Overall, inadequate acquisition of satellites was not an issue during the surveillance of Felicia. The temperature sensor developed by Vaisala has a lag in the temperature measurements due to the rapid fall speeds of the GPS sondes at high altitude. ASPEN auto-corrects this temperature lag by inclusion of the following formula:

$$T = T_m + \left(\frac{\partial T}{\partial z} \right) \left(\frac{\partial z}{\partial t} \right) \times \tau \quad (1)$$

where T_m is the GPS sonde measured temperature, $\partial T/\partial z$ is the sonde measured lapse rate, $\partial z/\partial t$ is the sonde measured fall velocity, and τ is the time constant of the temperature sensor. Additional corrections to temperature and wind sonde measurements are discussed in Hock and Franklin (1999). ASPEN outputs the AVAPS files in both QC

data files and QC skew-T log-P diagrams. A comprehensive overview of the ASPEN program and its QC procedures are provided by NCAR and Martin (2007) at the following URL: (<https://www.eol.ucar.edu/system/files/Aspen%2520Manual.pdf>).

After running the AVAPS datasets through ASPEN, the soundings are subjectively scrutinized for errors. Although ASPEN is able to resolve most errors associated with the sondes, issues with sensor wetting, relative humidity (RH) accuracy, and telemetry require inspection. It is prudent to mention that as the sondes are jettisoned from the aircraft, there is a time lag in which the pressure, temperature, and humidity (PTH) sensors equilibrate from the aircraft environment to the atmospheric conditions. The P and T sensors are able to resolve this equilibration slightly faster than the H-Humicap. On average, the sondes provide useful data starting at 190 hPa.

Sensor wetting may occur when a sonde passes through a cloud and liquid collects on the humidity sensor. As a sensor enters into a layer of unsaturated air, the humidity sensor may continue to read 100% humidity. On a skew-T log-P diagram, a sensor wetting signature is characterized by a saturated profile along a moist adiabat that then transitions to a dry adiabatic lapse rate while remaining saturated. Bogner et al. (2000) offer a simple method to fix sensor wetting; locate where the lapse rate becomes dry adiabatic while maintaining saturation, and carry a constant mixing ratio from this level to the surface (Fig. 12). This procedure yields more realistic humidity values for the subcloud layer which are then used in further analysis.

In the GPS sondes jettisoned around Felicia, some layers of the sonde profiles hover at >98% RH while following a saturated adiabat. It is reasonable to suspect that these slight departures from 100% RH are associated with the <5% accuracy error range

of the RH sensor. Wang (2005) concluded there is no systematic dry bias of the GPS sondes RH sensor near saturation. The sondes released around Felicia do not conflict with this assertion, but it seems reasonable that a dry bias exists *within* the <5% error range of the RH sensor with regard to near saturated conditions (Fig. 13). Specifically, if the error range associated with the RH sensor is <5%, and several sondes depict layers of 98% RH, how can one refute the possibility that the 2% departure from saturation is not associated with the inherent accuracy error of the sensor?

Each GPS sonde incorporates a 400 MHz telemetry transmitter in order to send data from the sonde to the aircraft AVAPS. On a few occasions the telemetry failed, resulting in layers absent of data. Layers that were thin, and layers that had a very predictable consistent behavior at start and end points, were interpolated, as described in the following section.

3.2 Analysis with the Sonde Data

After the sondes undergo case specific error corrections, the successfully deployed sondes are processed through a program created by Dolling (2012). Felicia weakened substantially over the three days of sampling, but during each synoptic surveillance mission of ~6 hours, the TC filled by only a few hPa, so it is reasonable to assume a steady-state storm for each data gathering period. The duration of the circumnavigation for the 8th and 9th was ~ 2 h. Additionally, the sonde deployments during the circumnavigation occurred at a radial distance of 3-degrees latitude from the center of the TC where evolution (e.g., spin down) is likely slower than the core. The Dolling program outputs a list of variables including but not limited to θ_e , tangential

winds, and radial winds. The following subsections briefly outline the approach of the program.

The position of each deployed sonde with respect to the movement of Felicia is essential in order to compute accurate storm relative variables such as radial and tangential winds. The first step is to formulate the storm track of Felicia. This is done by decomposing the movement of Felicia into latitude and longitude based on the NHC's best track (BT) data. Regression lines were imposed on the center fixes for latitude versus time and longitude versus time for the 3-day G-IV mission. The circulation center positions from BT were well approximated by a linear regression with $R^2 > 0.96$ for the G-IV missions.

Once all the GPS sondes are post-processed for erroneous data, a median launch time for each mission is determined by which all the data during that mission will be composited. The launch time for each sonde is added to the Dolling program in order to find the sondes relative time with reference to the composite time of the storm track during mission. Thus, as the sonde descends its latitude and longitude positions are deduced with respect to the movement of the storm with time. Every half second time step in which the GPS sonde takes a reading the pressure, temperature, RH, earth relative speed of the sonde, direction of the sonde, and altitude is computed with reference to the relative position of the moving storm. This is conducted for each mission.

Data gaps are caused by an assortment of factors but primarily the data gaps result from transmission problems and incorrect or failed measurements by the sonde's instrumentation. The program that calculates the field variables mentioned above

automatically implements linear interpolation of data gaps less than or equal to 300 m. Gaps larger than 300 m are left as missing data.

3.2.1 *Calculating Storm Relative Winds and Thermodynamic Variables*

The GPS sonde measures the earth relative speed of the sonde and the direction of the sonde at half second intervals. To derive storm relative winds, the u and v components of the storm are subtracted from the u and v components of the GPS sonde at each time step. The following equations are used to compute the radial and tangential winds:

$$V_{rad} = U_{rel} \cos \Theta + V_{rel} \sin \Theta \quad (2)$$

$$V_{tan} = -U_{rel} \sin \Theta + V_{rel} \cos \Theta \quad (3)$$

where U_{rel} is the u component of the storm velocity subtracted from the u component of the GPS sonde and V_{rel} is the v component of the storm velocity subtracted from the v component of the GPS sonde. The angle Θ is defined as the angle between the GPS sonde and a Cartesian coordinate system aligned along a unit circle. Dolling's program also computes the vapor pressure, saturation vapor pressure, mixing ratio, specific humidity, potential temperature (θ), lifting condensation level (LCL) temperature, and θ_e based on the procedure outlined by Bolton (1980).

3.2.2 *Calculating VWS, Divergence, and Vorticity*

Complete vertical soundings in the eastern Pacific basin in proximity to a powerful TC like Felicia provides the unique opportunity to compute values for VWS. Both the synoptic environment and the 3-degree circumnavigation around Felicia are targeted.

The VWS is calculated using the following formula:

$$VWS = \sqrt{[U_{225}-U_{850}]^2 + (V_{225}-V_{850})^2} \quad (4)$$

where $U_{225}, V_{225}, U_{850},$ and V_{850} are the averaged U and V components of the wind speed from 200 to 250 hPa (for U_{225}/V_{225}) and 825 to 875 hPa (for U_{850}/V_{850}) as measured by the GPS sonde. U_{850} and V_{850} refer to the U and V components of the wind at 850 hPa.

This 50 hPa average was used in order to get a more representative estimate of the flow pattern at each level. U_{225} and V_{225} were used instead of the traditional level at 200 hPa because consistent data did not always register near or above 200 hPa. Horizontal divergence and relative vorticity were calculated using Eqs. (5 and 6) for the area inscribed by the circumnavigations on the 8th and 9th of August. The levels were averaged ± 25 hPa.

$$DIV = \frac{du}{dx} + \frac{dv}{dy} \quad (5)$$

$$\zeta = \frac{dv}{dx} - \frac{du}{dy} \quad (6)$$

3.2.3 *Circumnavigated Analysis Levels*

Throughout this study three layers were analyzed to better understand the collapse of Felicia, centered at 975, 700, and 250 hPa. These values were chosen to summarize the influence of adverse factors to Felicia in the subcloud layer, midlevels, and the upper-levels. The subcloud layer was centered on 975 hPa based upon the circumnavigated skew-T log-P diagrams representing LCLs of ~ 950 hPa. For all of the analyses, a 50 hPa average is computed in order to suppress any outliers and obtain a representative

depiction of each layer. Measurements above and below this 50 hPa average were also investigated for consistency in order to ensure these three levels (975/700/250) are representative of a deeper layer. For these analyses, we assume Felicia maintains a steady state as the aircraft conducts the circumnavigations. The time of circumnavigation on 8 August was from 08:40:55-10:59:05 UTC while the sampling period on 9 August occurred from 09:19:40-11:37:05 UTC.

CHAPTER 4

RESULTS

4.1 Formation and Intensification- Attendant Conditions

According to the NHC, Felicia originated in the Atlantic basin on 23 July 2009 as an easterly wave. This easterly wave moved into the eastern North Pacific and started to organize deep convection on 1 August around 110°W. The cluster of deep convection achieved tropical depression (TD) status at 1800 UTC 3 August and tropical storm (TS) classification 0000 UTC 4 August at approximately 12°N, 122°W based on both archived satellite imagery and the NHC's Tropical Cyclone Report for Hurricane Felicia. With satellite derived SSTs between 28 and 29°C and a synoptic regime characterized by low VWS, Felicia rapidly intensified from 0000 UTC 4 August through 0000 UTC 6 August while being steered to the WNW by a well-defined deep-layer ridge. Felicia achieved a minimum central pressure of 935 hPa at 0000 UTC 6 August 2009.

Based on NOAA OIV2 SSTs for the week of 6 August 2009 in the eastern North Pacific basin were .5 to 1.5°C above normal. Consequently, Felicia's initial growth and intensification occurred over SSTs greater than 28.5°C near 9°N 115°W. As Felicia tracked toward the WNW and intensified to a category 4 hurricane, SSTs were maintained at 28-28.5°C. At approximately 1200 UTC 5 August, Felicia started to track over cooler water. Despite a slight reduction in SSTs, Felicia continued to intensify until 0000 UTC 6 August based on both BT and the Advanced Dvorak Technique (ADT) intensity estimates.

Felicia developed and intensified along the southern boundary of an expansive, deep-layered ridge that stretched from the eastern to the central North Pacific. During this

period the TC maintained a WNW track at 6-8 m s⁻¹. On 5 August, Felicia approached the western boundary of the ridge and entered a weak flow regime characterized by high pressure far to the NE (Fig. 14). As a result, Felicia's movement slowed to ~5 m s⁻¹ and her track shifted due NW from 0000 UTC 5 August through 1200 UTC 7 August. On 7 August, Felicia approached the southeastern quadrant of a rejuvenated high cell and the dominant flow shifted Felicia's direction to a more westerly heading again.

The VWS in the immediate vicinity of Felicia during formation and intensification was fairly weak, on the order of 5-10 m s⁻¹ according to CIMSS model analysis which incorporates gridded AMV output (Fig. 15). CIMSS VWS analyses alongside CFSR reanalysis data indicate Felicia remained in a region of low environmental shear through at least 7 August, however, a strong gradient in VWS resided more than 5° latitude to the NW of Felicia from as early as 0000 UTC 5 August onward.

The dry, subsident synoptic regime associated with the Pacific High is clearly depicted by the average total precipitable water (TPW) during the month of August 2009 as highlighted by the NOAA Special Sensor Microwave Imager Sounder (SSMIS). A strong zonal gradient in TPW existed from the southern tip of the Baja peninsula to longitudes near Hawaii; above 20°N, values of monthly averaged TPW were less than 30 mm while the near equatorial convergence zone (NECZ) featured more than 55 mm of TPW. At 0000 UTC August 7, CFSR depicted TPW values greater than 50 mm covered an expansive region north of 20°N from 122°W to 135°W (Fig. 16). The stark contrast between monthly averaged TPW and TPW represented at 0000 UTC 7 August 2009 is attributed to enhanced convection associated with an active NECZ, TS Enrique, and

Hurricane Felicia. The dry air signature of the subtropical high is present in Figure 16; however, the aforementioned convective fields have moistened the atmosphere farther north than usual. Overall, as Felicia tracked WNW, she entered an increasingly dry environment with regard to midlevel moisture. This is exemplified by satellite imagery and overlaid surface pressure analysis as shown in Fig. 17. The influence of this stable surrounding environment on Felicia's intensity is evaluated in later sections.

4.2 Actual Intensity versus Maximum Potential Intensity

The actual intensity of Felicia based on BT and ADT is shown in Fig. 18 alongside the estimated central pressure evaluated by MPI theory. During Felicia's RI stage, BT and ADT follow closely to each other while the MPI estimation exhibits a low bias due to its sole evaluation based on surface inflow and tropopause outflow temperature. At maximum intensity, both the BT and ADT approach the MPI value. It is important to mention that the deviation between the MPI and BT/ADT at maximum intensity in Fig. 18 is likely even less since SST was utilized as the inflow temperature rather than a more representative, slightly cooler near surface inflow temperature. Felicia began to lose intensity at 0600 UTC 6 August. During this time all three curves (BT/ADT/MPI) exhibit an equivalent weakening trend through 0600 UTC 7 August. This initial decay reflects the decrease in inflow temperature as Felicia tracked over cooler SSTs. At 0600 UTC 7 August the three curves diverge, with BT maintaining a gradual weakening trend, ADT suggesting enhanced weakening, and MPI leveling off. At 1800 UTC 7 August, ADT indicates a re-intensification through 0600 UTC 8 August with BT suggesting continued weakening. At 1200 UTC 8 August, ADT begins to suggest a weakening trend and catches up to BT at 0000 UTC 9 August.

4.3 SSTs and the Initial Decay

From 0000 UTC 6 August through 0000 UTC 8 August Felicia tracked toward the NW, across strong SST gradients; SSTs decreased from 28.5°C to below 25.5°C underneath the circulation center (Fig. 19). Correspondingly, minimum sea level pressure fell from 935 to 970 hPa according to BT. This SST decline is supported by the fact that the BT and ADT intensity estimates follow the same trend as MPI from 0600 UTC 6 August through 0600 UTC 7 August. On 8 August, SSTs stabilized at 25-25.5°C beneath the storm center as Felicia moved due W.

4.4 Outflow Channel Enhancement

After Felicia tracked over cooler waters from 0600 UTC 6 August through 1800 UTC 7 August (Fig. 19), Felicia re-intensified as highlighted by CIMSS ADT, the Tropical Analysis Forecast Branch (TAFB), and the NHC's Hurricane Felicia Discussion at 0300 UTC 8 August. According to CIMSS ADT, the estimated central pressure dropped from 980 hPa to less than 960 hPa between 1800 UTC 7 August and 0000 UTC 8 August (Fig. 18). Interestingly, the NHC BT maintained a steady weakening trend during this period. At 0000 UTC 8 August, NHC BT evaluated Felicia's central pressure at 970 hPa while TAFB estimated a central pressure of 960 hPa. Figure 20 shows four satellite IR views every 3 h during the re-intensification from 1500 UTC 7 August through 0000 UTC 8 August. Note that the spatial extent of the cold cloud tops less than -50°C increased, these cold tops became more axisymmetric, and the eye also became better defined. Tropical Rainfall Measuring Mission (TRMM) 85 GHz Horizontal imagery also portrayed a period of re-intensification, with better organization of deep convection around the eyewall between overpasses at 1354 UTC and 2205 UTC 7

August. According to CIMSS, Felicia began filling at 0600 UTC 8 August. At this time, the estimated pressure difference between BT and ADT was more than 15 hPa.

Unfortunately, C-130 aircraft reconnaissance was not helpful in pinpointing a central pressure during this re-intensification since the earliest mission occurred at 1400 UTC 8 August. The preponderance of evidence supports the contention that Felicia did re-intensify though 20 hPa may be viewed as somewhat extreme deepening.

4.4.1 Is the STJ Responsible for Felicia's Re-Intensification?

Black and Anthes (1971) used satellite derived winds to determine that the major outflow channel winds of mature TCs extended to an average radius of 800 km. Since Felicia was not a major hurricane prior to re-intensification as evidenced in Fig. 20a, an anticyclonic outflow of 8 degrees latitude is not likely. In fact, during Felicia's re-intensification water vapor and visible satellite imagery indicated Felicia's anticyclonic circulation extended outward to about 4.5 degrees latitude (or ~500 km) within the NW quadrant (Fig. 21). In another applicable study, Sadler (1976) examined the interaction between TUTTs and nascent typhoons Gilda and Harriet. Sadler noted that an interaction appeared to occur when the TUTT was approximately 500 km from the nascent TC's surface vortex. Felicia was an established TC prior to interaction with the TUTT; therefore a distance of 500 km between the TUTT and the vortex center of Felicia is likely associated with heightened VWS rather than beneficial outflow enhancement.

In order to evaluate if Felicia's re-intensification was attributed to an enhanced outflow channel, as shown for other TCs by Sadler (1976, 1978), the upper-level flow field and its relationship to Felicia's anticyclonic outflow channel are examined. A stronger outflow channel removes low momentum from the core and thus acts as a

momentum source (Holland and Merrill 1984). GOES West water vapor imagery and overlain Global Forecast System (GFS) model 250 hPa heights and winds shed some light on the potential interaction between the TUTT's attendant STJ and the outflow channel of Felicia (Fig. 22). Initially, the STJ and its associated wind field are positioned more than 800 km to the NW of Felicia's anticyclonic outflow (~4.5 degrees latitude from the core of Felicia). As the separation distance between the STJ and the outflow channel decreases, at some point the anticyclonic outflow of Felicia is given a boost via the complementary wind flow associated with the STJ. In order to quantify the degree of interaction, a separation distance is determined, defined as the distance between Felicia's anticyclonic outflow at 4.5 degrees and the gradient of 15-18 m s⁻¹ winds at 250 hPa based on CFSR. It is important to reiterate that the 7 August G-IV GPS sonde data is incorporated into the CFSR fields, therefore greater confidence can be placed on the position and strength of the STJ during the period of G-IV surveillance. The G-IV data was not used exclusively in determining the separation distance because the 7 August G-IV flight was not a comprehensive synoptic surveillance mission like 8 and 9 August. An example of the methodology in determining the separation distance is demonstrated in Fig. 23.

The results indicate that separation distance (defined in prior paragraph) steadily decreases from ~700 km at 0000 UTC 7 August to zero km at 1200 UTC 9 August (Fig. 24). During Felicia's re-intensification from 1800 UTC 7 August through 0600 UTC 8 August, separation distance drops from roughly 400 to ~230 km. After this point the separation distance continues to steadily drop to zero. The evolution of this separation distance analysis indicates that there is a period in which the STJ may have provided an

enhanced outflow channel for Felicia to re-intensify. Specifically, this distance is 400 to 230 km from the TUTT's STJ to the anticyclonic outflow of Felicia, or roughly 900 to 730 km from the STJ to the vortex center of Felicia. Since SSTs are on the decline and Felicia entered an environment of lower midlevel moisture, it is reasonable to posit that the re-intensification of Felicia is possibly due to enhancement of the northern anticyclonic outflow channel. This conclusion is supported by satellite imagery, CIMSS ADT, and NHC Hurricane Felicia advisory discussions.

4.5 Basic G-IV Analyses

At the time of Felicia's re-intensification, the G-IV was en route to Honolulu and sampling the environment to the N and NW of Felicia. GPS sondes were jettisoned along the flight route from 5:30-13:30 UTC 7 August. All deployed sondes described an environment associated with the Pacific High: deep-layered easterly flow with strong inversions in the east transitioning to higher, slightly weaker inversions at longitudes near the Hawaiian Islands. The deep layer of low relative humidity and the near dry adiabatic lapse rates above a strong inversion are indicative of subsidence. Specifically, deployment location #1 had an inversion base of ~950 hPa while sonde deployments 10-17 had inversions around 800 hPa. On 7 August, the axis of the TUTT at 200 hPa extended from NE to SW at longitudes of 150-155°W. Elsewhere, west-southwesterly flow dominated above 300 hPa associated with the STJ. Below 300 hPa, easterly flow prevailed.

Before and after the G-IV completed a circumnavigated route around Felicia on 8 and 9 August, the aircraft conducted synoptic surveillance of the environment to the NW of Felicia. Similar to the 7th, the skew-T log-P diagrams in the environment to the NW of

Felicia on the 8th and 9th suggest subsidence, and inversions reside at ~825 hPa. As one might expect, deployment location #8 on 8 August described an environment in transition between the synoptic environment and that of Felicia; a weaker inversion and higher boundary layer moisture content. At the 3-degree circumnavigation, higher moisture resided throughout the depth of the troposphere (Fig. 25). The green vertical profile of θ_e portrays the layer averaged environment based on sonde deployments 1-7 and 24-27 (Fig. 9) and 1-11 and 26-27 (Fig. 10). Therefore, this green curve represents a typical θ_e profile one might expect in the Tradewind environment; modest θ_e values in the low-levels dropping to a low mid-tropospheric minimum at 775 hPa followed by a gradual increase to the top of the troposphere. Although both the 8th and 9th circumnavigation profiles are similar in overall structure, on average, the 300-800 hPa θ_e layer on the 8th is ~3 K greater than the 9th highlighting a decreasing trend in θ_e around the 3-degree circumnavigation between the sampling periods on 8 and 9 of August.

Divergence and vorticity are calculated for the circumnavigation at 8:40-11:00 UTC 8 August and 9:20-11:40 UTC 9 August. The layered analysis of divergence exhibits convergence below 800 hPa, with 8 August demonstrating slightly greater convergence throughout this layer with a peak value at $-2.4 \times 10^{-5} \text{ s}^{-1}$ (Fig. 26). Above 800 hPa and continuing to ~200 hPa on 8 August there is weak divergence. Contrarily, from 200–400 hPa, 9 August analysis portrays strong convergence with a maximum near 200 hPa at $-2.15 \times 10^{-5} \text{ s}^{-1}$. This convergence aloft is attributed to the nearby STJ and its SW flow impinging on the 3-degree ring. The low resolution of this layered analysis of divergence suggests there may be convergence from the STJ at levels as low as 600 hPa;

however, storm relative wind flow indicates the STJ's wind field does not penetrate below 400 hPa.

Vorticity for the circumnavigations paints a predictable picture of positive relative vorticity throughout the depth of the analysis, and a trend towards zero at 200 hPa (Fig. 27). With relative vorticity essentially zero at ~ 200 hPa, it can be deduced that this 3-degree circumnavigational ring occurs proximate to the inflection point in which the cyclonic nature of Felicia transitions to anticyclonic outflow. The largest values of relative vorticity for the 8th and 9th are $7.0 \times 10^{-5} \text{ s}^{-1}$ and $6.6 \times 10^{-5} \text{ s}^{-1}$ respectively, and occur at near 800 hPa. This trend from 8 to 9 August corresponds to a reduction of relative vorticity by $\sim 6\%$.

4.6 Subcloud Layer Fields

In order to investigate the detrimental effects, if any, residing in the boundary layer, composites of both storm relative flow fields and θ_e are examined along the 3-degree circumnavigations within the subcloud layer. On average, skew-T profiles from the GPS sondes revealed a cloud base of roughly 950 hPa therefore this subcloud layer analysis was centered at 975 hPa. Based on the tangential flow at 975 hPa, both 8 and 9 August indicate a highly asymmetric wind field at 3-degrees (Fig. 28a). The strongest tangential winds on both days are $\sim 15 \text{ m s}^{-1}$, with a peak in the W quadrant on 8 August, transitioning to the N on 9 August. The weakest tangential winds lie clockwise from N to S on 8 August at $\sim 9 \text{ m s}^{-1}$ while 9 August is characterized by minimum winds in the E/SE quadrant at $\sim 5 \text{ m s}^{-1}$. From the 8th to the 9th, the average tangential flow around the circumnavigation drops from over 11 m s^{-1} to less than 9 m s^{-1} suggesting a drop of intensity between the 8 and 9 August sampling periods. The storm relative radial flow

presents a similar picture of asymmetry; radial inflow peaks along the N to NE sector for the 8th and from the N to E quadrant on the 9th (Fig. 28b). Interestingly, there is greater inflow on the 9th, at more than -10 m s^{-1} as compared to $\sim -8 \text{ m s}^{-1}$ on the 8th. From 8 to 9 August, weak inflow in the S/SW sector transitions to outflow.

The θ_e values at 975 hPa range from 340 to 350 K along both of the 3-degree circumnavigations (Fig 29). Both 8 and 9 August profiles are similar except for a marked decrease in θ_e along the NNW-NNE quadrant on the 8th. This minimum in θ_e along the N quadrant is collocated with storm relative radial inflow of -6 to -8 m s^{-1} . These θ_e values of 340 K in the N/NW sector of the circumnavigation on the 8th are quite similar to the θ_e values of the synoptic environment on 8 and 9 August suggesting the N/NW section of the circumnavigation on 8 August is representative of trade wind air.

IR satellite imagery at 0900 UTC 8 August demonstrates that most of the deployment locations, including the N/NW sector, were located outside of the primary convection associated with Felicia (Fig. 30). In this figure, the red circle denotes a radial distance of 3-degrees latitude from Felicia's center of circulation and the approximate location of the deployed sondes. What is evident is that in the northern sector this red line resides along the boundary between Felicia's cirrus outflow and the stratocumulus field associated with the Subtropical High. Therefore, the minimum in θ_e during the circumnavigation on the 8th is most likely due to a gentle intrusion of environmental air. In order to determine if this drop in θ_e at 3-degrees along the N/NW sector is responsible for the weakening of Felicia, a theoretical air parcel is timed from this radial distance to the inner core. A few assumptions need mention; firstly, this estimation assumes that the analysis at the 975 hPa level applies to the majority of the subcloud layer. Secondly,

moisture and heat fluxes in the boundary layer are not considered, partially because AXBTs were not jettisoned during reconnaissance of Felicia. Finally, the radial flow is assumed to increase linearly to -12 m s^{-1} as the parcel travels radially inward to the core. With these assumptions in mind, storm relative radial flow increasing from -7 to -12 m s^{-1} with decreasing radius would take roughly 8-9 h to reach the core of Felicia given the observation at a radial distance of 3-degrees. If the near core radial inflow was -15 m s^{-1} , the flow along the 3-degree ring would reach the core in ~ 7.5 h. The timing of these potential intrusions into Felicia's core are in alignment with the decrease in Felicia's intensity observed from 8-9 August, however, it is important to note that this minimum in θ_e is not present in the θ_e profile for the 9th, suggesting that the decrease in the θ_e on the 8th is not a prolonged feature during the sampling periods. Moreover, the three sondes that measured substantially lower values of θ_e on 8 August account for only 21% of the 3-degree ring. Although the aforementioned assumptions are constraining, especially the diabatic effects associated with ~ 7.5 h of residence time in Felicia's inner region, this estimation demonstrates the influence of dry air in the subcloud layer was not significant.

C-130 aircraft reconnaissance flights into the core of Felicia on 8 and 9 August were able to determine if the lower θ_e values observed along the N/NW sector of the G-IV's 3-degree circumnavigation on 8 August influenced Felicia's intensity. The C-130 flight on the 8th began at 14:45 UTC 8 August and ended at 00:39 UTC 9 August while the flight on the 9th took place from 02:28 UTC to 12:08 UTC 9 August. Four center fixes were obtained on each mission. Between the last center fix on the 8th and the first center fix on the 9th, a 6 h period, the central pressure of Felicia rose approximately 2 hPa. From the 8th to the 9th, averaged θ_e profiles in the subcloud layer for sondes jettisoned in the

near eyewall region exhibited a drop of 1.5 K. A drop of 1.5 K translates to an estimated increase in a TC's central pressure of 4.5 hPa (Malkus and Riehl 1960; Emanuel 1986). Since only 2 hPa of filling was observed from the C-130 center fixes, the decay was even slower than observational studies suggest (i.e., the eyewall column did not degrade as much as the assumption that -1.5 K extends throughout the column). Therefore, these C-130 missions demonstrate that the lower θ_e air measured along the G-IV's 3-degree circumnavigation on the 8th did not substantially impact the central pressure of Felicia.

4.7 Evidence of Dry Air Entrainment in the Midlevels

The storm relative radial flow in unison with θ_e at 700 hPa is analyzed with the primary objective to determine the presence and possible impact of drier, midlevel air at the 3-degree circumnavigations (Fig. 31). The storm relative radial flow (Fig. 31a) demonstrates a similar profile for both 8 and 9 August; peak radial outflow of $\sim 5 \text{ m s}^{-1}$ in the W-NW sector is followed by a gradual decline to very weak radial inflow of -1 to -2 m s^{-1} in the NE through SW portions of the circumnavigation. Figure 31b highlights θ_e values in the midlevels. Clockwise from SW to NE, both 8 and 9 August indicated that θ_e fluctuates between 335 K and 342 K. In particular, the SE quadrant exhibited a drastic decrease in θ_e during both sampling periods, with the 8th dropping to 330 K and 325 K on the 9th. This sector of lower θ_e was collocated with very weak storm relative radial inflow of -1 to -2 m s^{-1} on both circumnavigations. This very weak 700 hPa radial inflow at a radial distance of 3-degrees is supportive of vertical profiles of radial flow composed by Frank (1977). With the assumptions outlined in the previous section in mind, this sector of lower θ_e on the 8th would have reached Felicia's core in 1.7 days, a value far too long to be a noticeable factor in Felicia's decay since Felicia's central pressure began to

steadily fill at approximately 1800 UTC 8 August. With this time estimation, I have assumed that there is no increase in the radial flow through the midlevels, unlike the subcloud layer. This signature of lower θ_e in the midlevels at 3-degrees is more representative of environmental air, as previously highlighted in Figure 30. Comparison to visible and IR satellite imagery during the sampling period supports the contention that the GPS deployments occurred along the fringes of the cloud mass associated with Felicia.

4.8 Evidence of the STJ's Intrusion into the Inner Core

The strength and position of the STJ with respect to Felicia was critical in determining the degree of influence on Felicia's intensity. At 0900-1240 UTC 7 August, the TUTT axis resided at approximately 25°N 152.5°W with 25 m s⁻¹ winds draped from 147.5°W to 140°W at 26°N (Fig. 32a). During this time frame, the approximate position of Felicia's center of circulation was 18°N 135°W. On 8 August the TUTT, which alters the strength and location of the STJ, retrograded, and the strongest winds were located just NE of the Hawaiian Islands at 22.5°N 152.5°W (Fig 32b). Figure 32c demonstrates that the STJ followed the motion of the TUTT and established itself over the Hawaiian Islands. Furthermore, the STJ increased its coverage and strength from 8-9 August, becoming more zonal and expanding its area of high winds along longitudes near Hawaii, and just east of 150°W.

Latitude-longitude plots presenting only the GPS recorded storm relative winds allow one to explicitly determine the degree of influence of the STJ on the 3-degree circumnavigated ring. The 3-degree circumnavigation on 8 August (Fig. 33a) was characterized by much weaker winds in comparison to the 9th (Fig. 33b). Along the NW

and SW quadrants on the 8th winds were $\sim 5 \text{ m s}^{-1}$, with anticyclonic flow along the NW sector and cyclonic flow to the SW. Contrarily, the storm relative winds on 9 August had a westerly component throughout the circumnavigation, with over 15 m s^{-1} westerly winds where the STJ impinged on Felicia. Overall, the storm relative flow at 200 hPa illustrates the intrusion of westerly flow associated with the STJ; the west side of the circumnavigation had strong W winds while more variable winds, in both magnitude and direction, characterized the eastern half. Since the E side of the circumnavigation was further away from the STJ and blocked by Felicia's vortex structure the winds were, unsurprisingly, weaker. However, the winds still exhibited a westerly component on the E side of the circumnavigation, suggesting that the STJ's adverse winds had reached the core of Felicia by the time of the sampling on 9 August.

From 8 to 9 August, both the storm relative tangential and radial flows at 250 hPa demonstrated increasing interaction with the TUTT's STJ (Fig. 34). On 8 August, tangential flow was weak throughout the majority of the circumnavigation. Tangential flow on the 9th was substantially different; strong cyclonic flow was limited to the SW portion of the circumnavigation, rapidly shifting to anticyclonic flow along the NW sector due to the proximity of the STJ. This pattern suggests a zone of strong divergence in the west due to the influence of the STJ. The storm relative radial flow at 250 hPa portrays a clear picture; intrusion of the TUTT's attendant STJ is evident at the 3-degree circumnavigation (Fig. 34b). Specifically, the 8th was characterized by radial inflow in the W-NW sector of -3 to -4 m s^{-1} while 9 August was over -20 m s^{-1} .

Since the amount of moisture at 250 hPa is minimal, analysis of θ_e is comparable to θ . The θ_e values along the circumnavigation at 250 hPa indicate the intrusion of the

STJ was not accompanied by a substantial change in θ_e , or θ for that matter (Fig. 35). As shown, θ_e on both 8 and 9 August only ranges from 345.5 to 348 K. In fact, data suggests that the intrusion of the jet along the NW sector is associated with a modest increase in θ_e of roughly 2 K.

4.8.1 *Quantifying the STJ's Intrusion into the Inner Core*

The VWS from 850-225 hPa further substantiates the adverse impacts of the STJ (Fig. 36). Along the 3-degree circumnavigation, 8 August exhibited wind shear of 8-15 m s^{-1} throughout the circumnavigation while 9 August demonstrated a doubling of the VWS in the NW quadrant to more than 30 m s^{-1} . Therefore, it is clear that the STJ intruded into the 3-degree ring along the W-N quadrant while the easternmost extent was somewhat sheltered and remained at less than 15 m s^{-1} VWS. There is less than 5 m s^{-1} VWS in the SW quadrant on the 9th, a location just S of the influence of the STJ.

The radial flow at 250 hPa rose substantially between the sampling period on 8 August to the sampling period on 9 August; gentle inflow of -3 to -4 m s^{-1} was replaced by -20 m s^{-1} of radial inflow in the W/NW quadrant. Based upon satellite imagery at 1200 UTC 9 August, the upper and lower level circulations of Felicia were already separated by the end of the G-IV sampling period at 11:40 UTC 9 August (Fig. 37). This separation is represented by colder cloud tops of the upper-level circulation being displaced to the east and the lower level circulation exposed to the west with warmer cloud tops.

Since both satellite imagery and GPS sonde analyses suggest that the STJ had already intruded into Felicia's core before the end of the G-IV surveillance on the 9th, the 250 hPa radial inflow along the NW quadrant was linearly interpolated between the

observation periods on 8 and 9 August, resulting in a value of -10 to -12 m s⁻¹ radial inflow at 0000 UTC 9 August. With the eyewall radius evaluated at 50 km, -11 m s⁻¹ radial inflow in the NW quadrant would have reached Felicia's core in approximately 7 h. This eyewall radius of 50 km is based upon the NOAA HRD 9 August H*wind analysis following the scheme developed by Powell et al. (1998), which incorporates the C-130 aircraft data and all other available observations platforms. The radial inflow was estimated from the 3-degree circumnavigation to the eyewall. The timing of this radial inflow estimated intrusion (0700 UTC 9 August) corresponding with IR satellite imagery is shown in Fig. 38. In this figure, deep convection associated with Felicia is graphically represented by the spatial extent of IR estimated cloud tops with temperatures less than -50° C. As shown, coverage of deep convection is 3-4 degrees² until 0600-0700 UTC 9 August, at which point deep convection (T < -50° C) steadily drops to zero. Satellite imagery evidence, demonstrating the initial stages of the STJ's flow impinging on the eyewall of Felicia with the upper-level circulation and deepest convection being displaced downshear to the east and northeast is shown in Fig. 39a. Figure 39b is a visible image of Felicia at 1600 UTC 9 August, with the low-level circulation clearly discernable along the western portion of the satellite image and downshear displaced convection straddling the east side of the vortex.

4.9 SHIPS Shear Evaluation of Felicia

The SHIPS operational forecasted shear is a blended calculation from the SHIPS shear predictors, SHDC and SHGC. Both SHDC and SHGC are computed from GFS model data and are evaluated from 850-200 hPa with an annulus of 0-500 km relative to the 850 hPa vortex center, after which the GFS model vortex is removed. SHGC is the

generalized shear, and differs from SHDC in that its shear value is computed by a pressure integral from 850 to 200 hPa rather than the two level of 850 and 200 hPa. The G-IV datasets on 8 and 9 August were absorbed into the SHIPS 1200 UTC GFS model runs, therefore these model runs have the added benefit of in-situ measurements in the vicinity of Felicia in order to better represent the true environmental flow, and subsequently, VWS.

Figure 40 presents the SHIPS operational forecasted shear after maximum intensity at 0600 UTC 6 August. Also plotted are the averaged 850-225 hPa storm relative VWS values around the G-IV 3-degree circumnavigations on 8 and 9 August. While the SHIPS shear predictors determine a shear value for an area 0-500 km relative to the 850 hPa vortex center, the storm relative G-IV computations of shear are solely determined by taking an average of the shear values along the 3-degree circumnavigations. Since the values of shear are not computed in the same fashion, there are large differences between the SHIPS shear forecast trends and the shear calculated from the circumnavigated GPS sondes. With consideration to this difference in shear methodology, the timing of the shear increase is more comparable than the variation in shear magnitude. Somewhat surprising, the SHIPS forecast on 6 August demonstrated the closest trend with regard to the timing of increasing shear; SHIPS shear forecasts on 7 and 8 August suggested a reduction in shear around Felicia from 1200 UTC 8 August to 0000 UTC 9 August while both the SHIPS 6 August forecast and the trend in G-IV circumnavigations from 8 to 9 August portrayed an increasing trend.

CHAPTER 5

CONCLUSIONS AND FUTURE WORK

5.1 Summary and Discussion

Hurricane Felicia was a major hurricane in the eastern and central North Pacific basin that threatened the Hawaiian Islands. Felicia reached a peak intensity of 935 hPa at 0000-0600 UTC 6 August. Beginning 7 August, the NOAA G-IV aircraft conducted synoptic surveillance of Felicia with the primary interest to improve forecasts of its track. During 8 and 9 August, the synoptic environment in which the TC was intended to track towards was sampled, and then a circumnavigation around the TC was conducted at a radial distance of 3-degrees latitude. The timing of each surveillance mission provided the opportunity to analyze an often overlooked stage of a TC's life cycle, decay. The value of this 3-degree circumnavigation from an intensity perspective was also examined. The primary caveat of this study is that the original intention of the G-IV deployment distributions was to improve track forecasts not intensity, therefore overt data gaps exist. Additionally, the circumnavigations are unable to recognize any processes in the core of Felicia such as eyewall replacement cycles, eyewall contraction, eye to eyewall mixing, convective flare-ups in the eyewall, and rainband competition within the eyewall.

Felicia's best track overlaid on the weekly satellite derived SST field indicated that Felicia moved over strong SST gradients just after maximum intensity. Specifically, SSTs dropped from 28.5°C to below 25.5°C underneath the circulation center from 0000 UTC 6 August through 0000 UTC 8 August coincident with the initial filling of Felicia's central pressure. During this time frame the synoptic environment to the N and NW of Felicia, as evidenced by satellite imagery and the GPS sondes, revealed deep layered

easterly flow emanating from the semi-permanent Pacific High. These easterlies were characterized by low relative humidity and near dry adiabatic lapse rates above strong inversions, suggestive of stable, subsident flow. Since the evolution of Felicia's MPI curve followed the same slope as the intensity estimations of BT and CIMSS ADT, it is reasonable to conclude that reduction of SSTs was the first blow to Felicia's intensity.

After a drop in intensity attributed to SSTs, the most critical component with regard to Felicia's intensity was the evolution of the STJ lying to the NW of Felicia and the westward movement of the TC. Above ~300 hPa, west-southwesterly flow prevailed, associated with the STJ. The upper-level trough, synonymous with the TUTT, and the STJ slowly retrograded from its position on 7 August at ~25°N, 150-155°W. As Felicia tracked due W, the separation distance between Felicia's outflow channel and the gradient of strong winds associated with the STJ decreased from ~700 to 400 km. During Felicia's re-intensification of ~20 hPa as evidenced by CIMSS ADT, this separation distance declined from 400 to 230 km. Therefore, as Felicia tracked westward towards the upper-level jet there was a transition from little to no interaction with Felicia, to a short-lived period of anticyclonic outflow enhancement at large radii, and then an overwhelming impingement of the STJ on the core of Felicia on 9 August. Since Felicia entered an increasingly hostile environment with regard to SSTs and a stable synoptic regime, it is reasonable to conclude that the re-intensification was attributed to a brief but optimal separation distance and orientation between the STJ and Felicia's northern anticyclonic outflow. These results are supportive of the pioneering work of Sadler (1967, 1976).

The G-IV circumnavigations during Felicia's decay on the 8 and 9 August revealed that, in both the subcloud layer and midlevels, there was no convincing evidence of lower θ_e air being entrained into the inner core of Felicia. The observed drop in θ_e on 8 August in the N/NW sector of the subcloud layer was characterized by substantial radial inflow, however, due to the duration and distance of the inflow trajectory from this confined portion of the circumnavigation to the core of Felicia it is reasonable to conclude that this measured drop in θ_e on the 8th was not a pivotal factor in Felicia's decay. Moreover, the subcloud layer on the 9th revealed that the observed drop in θ_e along the N/NW sector of the circumnavigation on 8 August had recovered. The midlevel drop in θ_e observed on both 8 and 9 August in the SE sector were not associated with inflow rates larger than -2 m s^{-1} , therefore this midlevel flow is also not a factor in Felicia's collapse.

In contrast, the upper-levels painted a clear picture with progressive intrusion of the STJ from 8 to 9 August. Specifically, the radial inflow along the NW sector of the circumnavigation quintupled from less than -4 m s^{-1} on 8 August to more than -20 m s^{-1} on 9 August. One may have expected that such a strong advection of environmental air into the inner core to be accompanied by a change in θ_e (a proxy for θ or temperature at such high altitudes). However, results indicated a flat θ_e profile characterized the NW sector from 8-9 August. With corresponding satellite imagery exemplifying the effects of VWS, the demise of Felicia was ultimately attributed to the debilitating effects of deep layer wind shear in excess of over 30 m s^{-1} impinging on the W/NW sector of Felicia.

Although satellite imagery and GPS sonde computed VWS clearly highlight the impact of VWS on Felicia, the physical mechanisms by which VWS acts to weaken a

mature TC are more ambiguous. While the theory of ventilation (Simpson and Riehl 1958; Gray 1968), in which a sheared environment displaces upper tropospheric warm anomalies from the low-level convergence of heat and moisture is widely accepted as a debilitating factor for developing TCs, the exact physical mechanism of how this occurs is still uncertain. DeMaria (1996) points out that ventilation of a mature TC, where warm air is drawn away from the upper-levels, would tend to de-stabilize the inner core of a TC and promote intensification. Additionally, ventilation may transport away low momentum air residing in the upper troposphere leading to enhanced flow over the inner core. This transport acts as a momentum source, and potentially contributes to spin-up of the vortex (Holland and Merrill 1984). From a thermodynamic perspective, ventilation of the warm core itself would lead to a temperature-pressure-wind adjustment; the addition of cooler, drier air would act to reduce the pressure gradient, weaken the surface winds, and consequently lower the energy fluxes drawn from the sea surface.

While the ventilation of a mature TC may act to increase or decrease the central pressure, conceptual models of the tilting of a TC core are widely recognized to adversely affect intensity. The vertical integration of the warm air in the eye and eyewall column of a tilted core highlights the weakening effects of TC tilt; reduced limits of integration for a tilted core results in a thinner layer of integrated warm air, which leads to a rise in sea level pressure, a weakening of the pressure gradient, reduced surface wind speeds, and less energy fluxes drawn from the sea surface.

DeMaria (1996) used a simple two-layer model to show that the potential vorticity (PV) of the vortex becomes tilted in the vertical when the upper-level vortex is displaced from the lower layer. In order to maintain a mass balance, the model vortex responds to

this PV tilt by inducing a midlevel warm perturbation above the low-level circulation center. In an actual TC, vertical stability associated with midlevel warming would act to inhibit core convection and lead to a filling of the central pressure. Additionally, this two-layer model of PV tilt also produced a cold anomaly downshear of the low-level vortex center that would promote convection in this downshear region. Firstly, this downshear convection would tend to rob the eyewall convection of inflow energy. Secondly, the downshear convection may generate downdrafts and outflow boundaries that would replace the inflow layer with lower θ_e air, leading to a reduction of moist enthalpy available to the eyewall. Therefore, this sequence of events combines the shear arguments discussed by Riemer (2010) and the adverse impacts of downdrafts pioneered by Barnes et al. (1983) and Powell (1990).

The numerical simulations produced by Frank and Ritchie (2001) suggest that weakening evolves from the top down. Essentially, they concluded that shear generates asymmetric upper-level PV and θ_e fields along with the deterioration of the upper-level warm core structure, which induces a rise in surface pressure. Frank and Ritchie (2001) hypothesize that the low inertial stability in the upper-levels allows the shear to prescribe these asymmetric patterns to the upper-levels first, before shifting downward with time and producing an increasingly shallower, vertically aligned.

How did shear lead to the demise of Hurricane Felicia? First, the satellite presentation of Felicia demonstrates a distinct downshear displacement of deep convection and this observation is supported by most conceptual models and observational studies (Black et al. 2002). While this supports the conclusions of both DeMaria (1996) and Frank and Ritchie (2001), the mechanisms of the two studies are

vastly different. Although both DeMaria (1996) and Frank and Ritchie (2001) stress the importance of asymmetries, the mechanisms and sequence of events by which a warm core dissipates in a sheared flow are not well understood. The low inertial stability in the upper-levels as presented by Holland and Merrill (1984) leads me to believe the initial weakening mechanism begins in the upper-levels. With regard to Felicia, I hypothesize that the heightened VWS acted to tilt the upper-level core downshear as well as disrupt the concentrated PV and θ_e fields of this layer. While the agitation of these PV and θ_e fields reorganize the vertically aligned vortex from the top down, the tilted core and asymmetries promote a downshear displacement of deep convection. The outflows from the downshear convection advect upshear and stabilize that region, further enhancing asymmetries. The shift in deep convection from the eyewall region to the downshear region at greater radii disrupts the original circulation in the lower levels by rerouting a portion of the inflow layer to the new downshear convection. More robust observation-based missions may be able to map the evolution of these conceptual models in order to pinpoint the most important mechanisms involved in how a warm core dissipates in a sheared environment.

The timing of the STJ's NW impingement on Felicia's eyewall was quantified using a linear interpolation of the storm relative radial flow along the 3-degree circumnavigation. Although several assumptions were implemented, -10 to -12 m s^{-1} of radial inflow translated to an intrusion 7-8.5 hrs later. This estimated intrusion was well supported by IR satellite imagery demonstrating the initial stages of the upper and low-level circulations undergoing separation and collapse of vigorous convection around the western half of the eyewall.

With regard to the TUTT and upper-level flow features, the G-IV GPS sonde results verified the findings of Sadler (1967, 1976), Holland and Merrill (1984), Chen and Chou (1994), Patla et al. (2009) and Shieh et al. (2013). The debilitating effects of high VWS on Felicia's inner vortex supported the work of McBride and Zehr (1981), Zehr (1992), DeMaria (1996), Gallina and Velden (2002), and Tang and Emanuel (2012).

5.2 Future Work

Tailoring the current G-IV flights for intensity research and forecasting is the primary future goal. For instance, if a STJ lies to the NW of a TC, as was the case with Felicia, deployment of a succession of sondes along the STJ wind gradient may be important in determination of potential TC intensity changes. And afterwards, following the traditional circumnavigation, the G-IV could safely approach the TC center by implementation of a zig-zag pattern in order to better map a given TC. In 2013, a tail Doppler radar was placed on the NOAA G-IV and this onboard radar could aid in better characterization of TC outflow channels, and the potential interaction with flows such as the STJ.

Alternatively, the Global Hawk Dropsonde System is an unmanned, high altitude observation platform intended to improve our understanding of TC intensity at both inner and outer core radii. Developed by NASA, the Global Hawk (GH) was first deployed into Hurricane Earl in 2010 and is capable of 30+ h flight times at altitudes up to ~ 19 km (Sippel et al. 2013). Due to its exceptional flight level and unmanned nature, the GH can fly over stratospheric penetrating eyewall convection and therefore sample the tropospheric extent of the eye and eyewall of TCs.

Coyote, essentially a GPS sonde flying a programmed pattern that is deployed from a Lockheed WP-3D Orion, is capable of horizontal and vertical movement with a flight time of ~ 1.5 h. After deployment Coyote is guided to investigate specific regions of a TC with the primary objective to improve thermodynamic measurements, particularly moisture, in the boundary layer of TCs. The addition of both the GH and Coyote platforms to traditional TC reconnaissance has the potential to help answer questions with regard to TC intensity, structure, and environmental interaction from an unmanned platform.

Comparison between the SHIPS operational shear forecasts and the VWS around the 3-degree circumnavigations highlighted the impact of differing shear methodologies. This idea of questioning traditional shear methodology has been addressed in a recent paper by Velden and Sears (2014) in which layer-means are computed instead of analyzing winds at two levels. Moreover, while SHIPS VWS is computed from a radial average of 500 km from storm center Velden and Sears evaluate the final VWS value at the storm center.

While current shear methodology calculates shear from all radial sectors equally, a case specific alternative approach or extension would consider computing VWS with more weight to a certain sector of the TC's annulus. Specifically, if there is a region of high VWS confined to a sector some radial distance from a TC and the TC is tracking towards this region of high VWS, perhaps this sector characterized by heightened VWS should carry more weight in the resultant shear computation. In this manner the lower shear associated with the rest of the annulus would not "dilute" the high VWS of the sector in which the TC is tracking towards. Naturally, this case specific approach would

not apply to all TCs; however, as evidenced by Felicia, VWS does not need to impinge on all sectors of a TC equally in order to drastically influence TC intensity.

TABLES

G-IV GPS Sonde Deployment				
Date	# of Failed Sonde Deployments	Total # of Deployment Positions	Success Rate of Deployment Positions (%)	Success Rate of Circumnavigated Deployment Positions (%)
8/7	3 (15 and 18 lost at launch, no winds for sonde 12)	18	83	<i>N/A</i>
8/8	1 (sonde 23 lost at launch)	27	96	100
8/9	3 (sonde 18 lost at launch, weak telemetry for sonde 16, no winds for sonde 21)	27	89	78
Total Success Rate of G-IV deployment positions (%)				90

Table 1. GPS dropwindsondes launched during the G-IV synoptic surveillance flights of Hurricane Felicia on 7-9 August 2009.

FIGURES



Figure 1. The NOAA Gulfstream IV-SP (G-IV) aircraft.

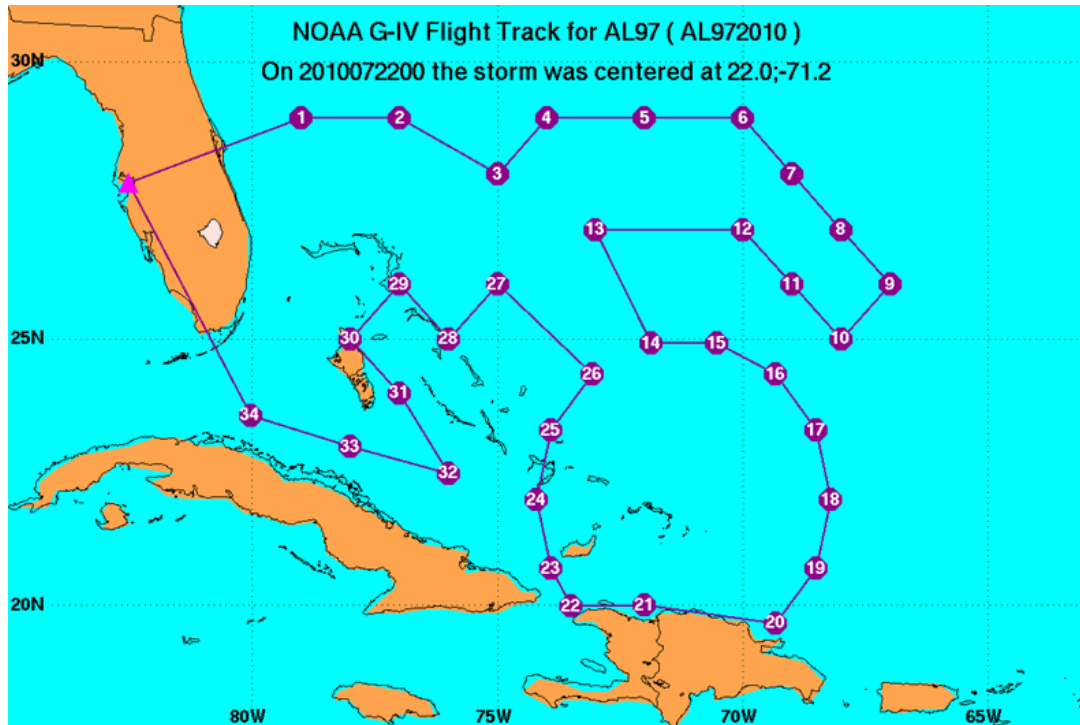


Figure 2. NOAA G-IV flight route in the Atlantic basin during TS Bonnie in July 2010. Sonde deployments 14-26 represent a 3^o circumnavigation around the center of the circulation (Courtesy of NOAA HRD).

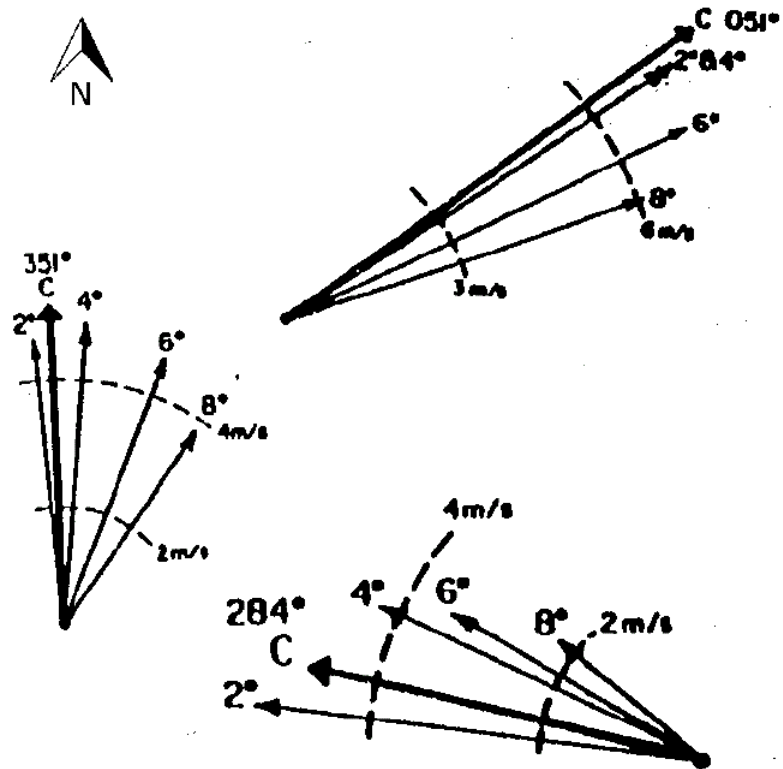


Figure 3. Schematic diagram demonstrating mean TC motion in the western North Pacific basin based upon composites of rawinsondes. Figure represents the 850-350 hPa layer and radial-band average wind vectors for northeast moving storms (top) at higher speeds, north moving storms at moderate speed (middle left), and westward moving TCs (bottom). Radial arcs delineating speed are shown in m s^{-1} . The “C” vector represents the mean cyclone motion of a given TC (Adopted from Gray 1989).

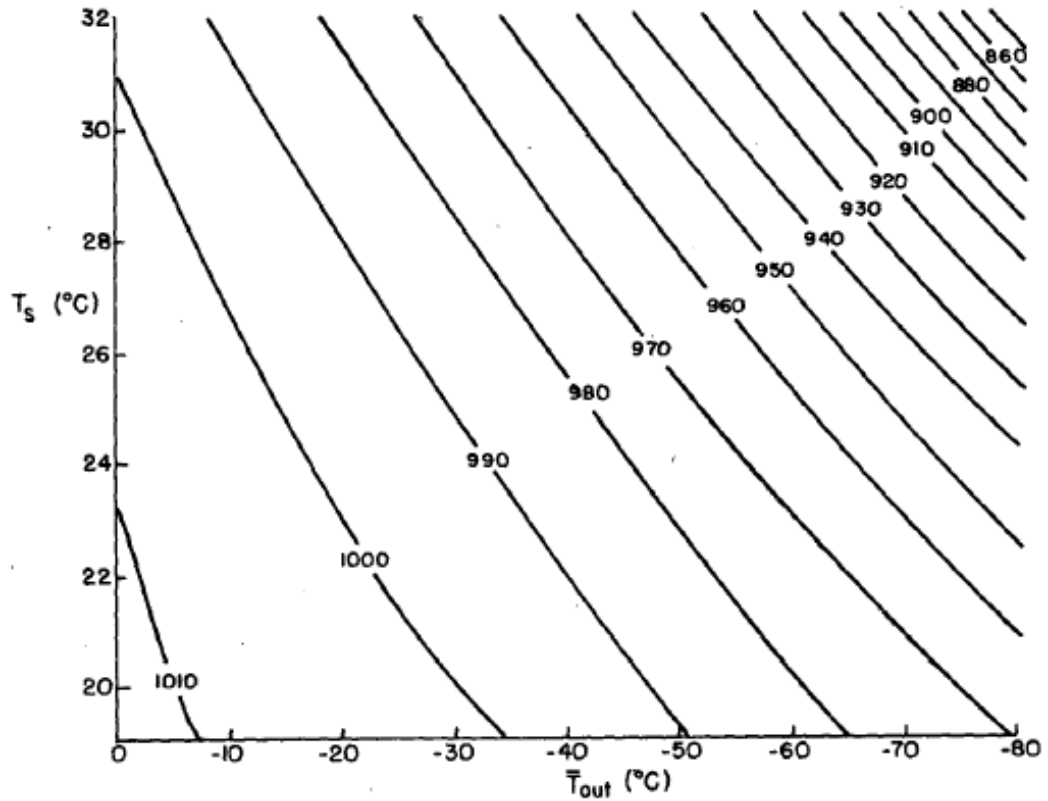


Figure 4. Evaluation of the minimum attainable central pressure (hPa) of a TC as a function of the surface air temperature (T_s) and the weighted mean outflow temperature near the tropopause (T_{out}). The ambient surface pressure, ambient surface relative humidity, coriolis parameter f , and r_o are 1015 hPa, 80%, 20 degrees latitude, and 500 km, respectively (Adopted from Emanuel 1986).

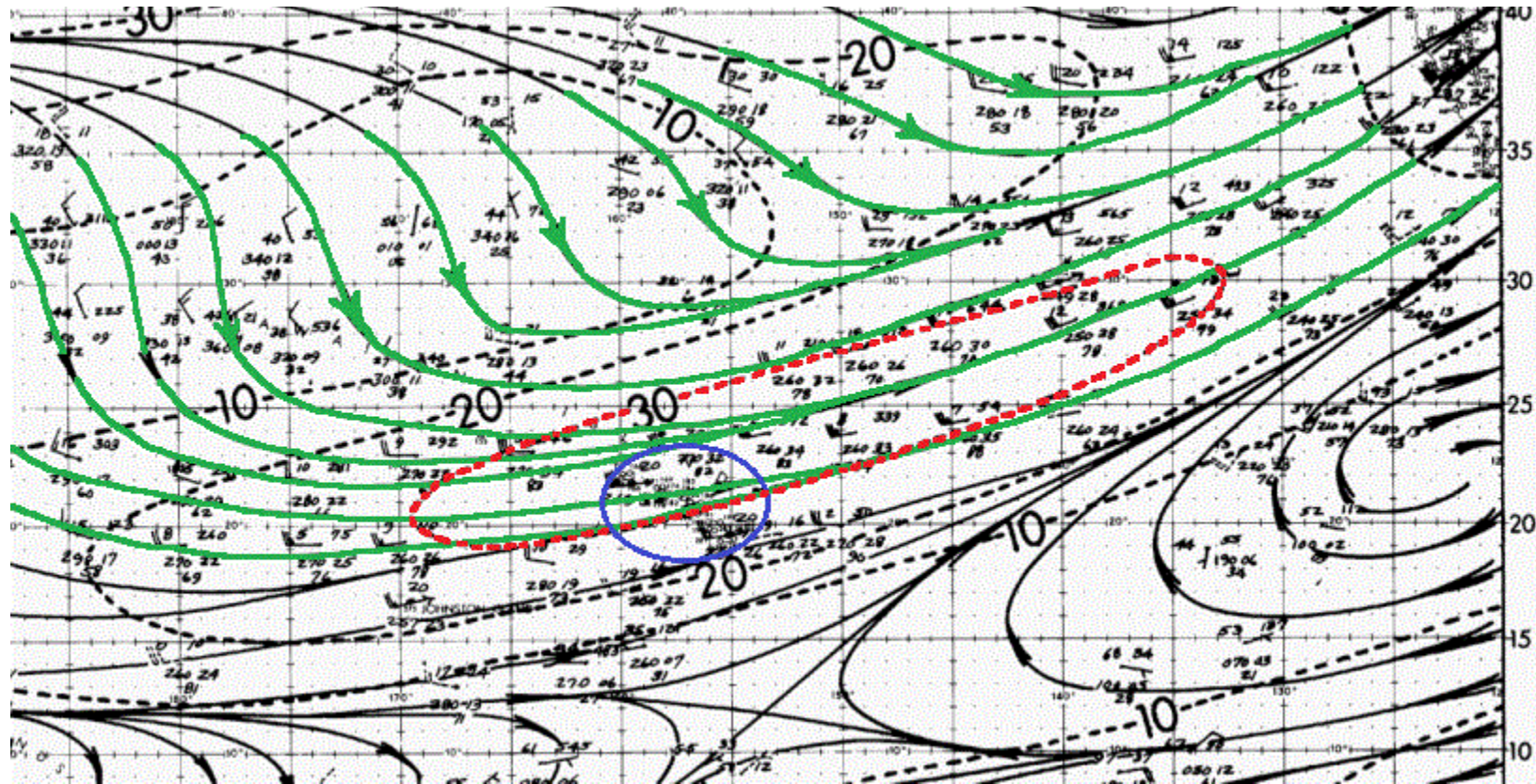


Figure 5. Streamline analysis of mean flow (kts) at 200 hPa near the Hawaiian Islands during the month of August based on cloud-drift winds and upper air observations. The North Pacific Tropical Upper Tropospheric Trough (TUTT) is evident, extending from NE to SW in green. The location of the Hawaiian Islands are circled in blue and the TUTT's wind zone greater than 30 knots is outlined in red. Adopted from Sadler (1975).

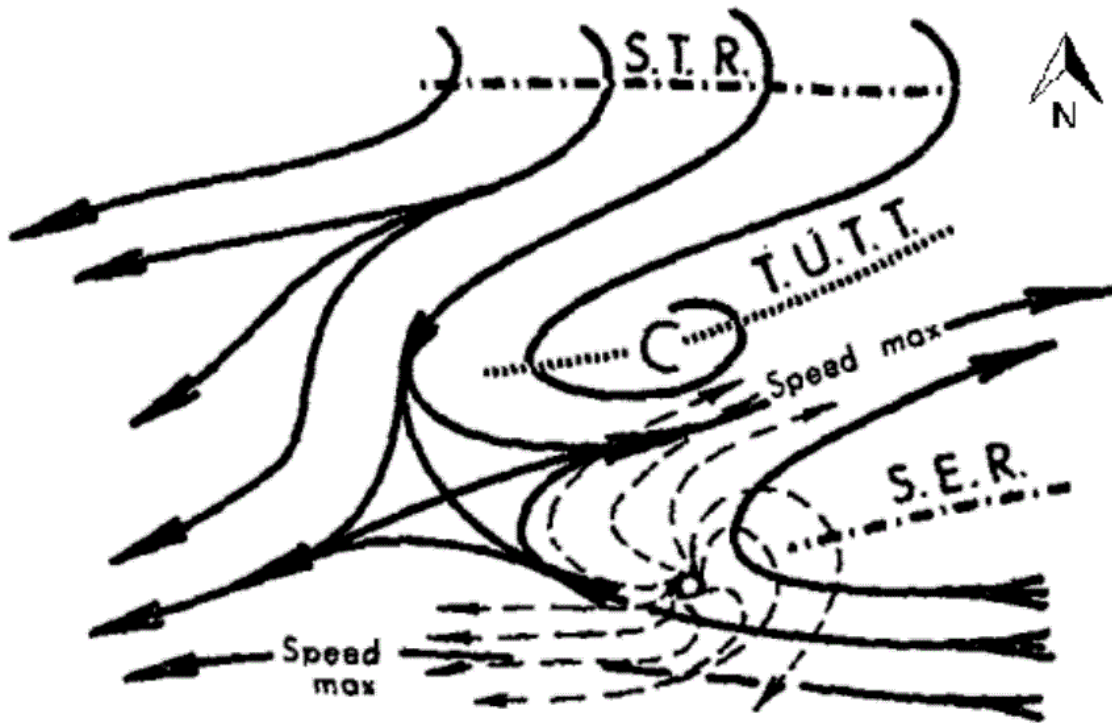


Figure 6. TUTT interaction with the anticyclonic outflow of a TC. Through proper orientation and position of a TUTT cell, enhancement of a TC's anticyclonic northern outflow channel can be achieved by means of the TUTTs associated jet. Adopted from Sadler (1976).

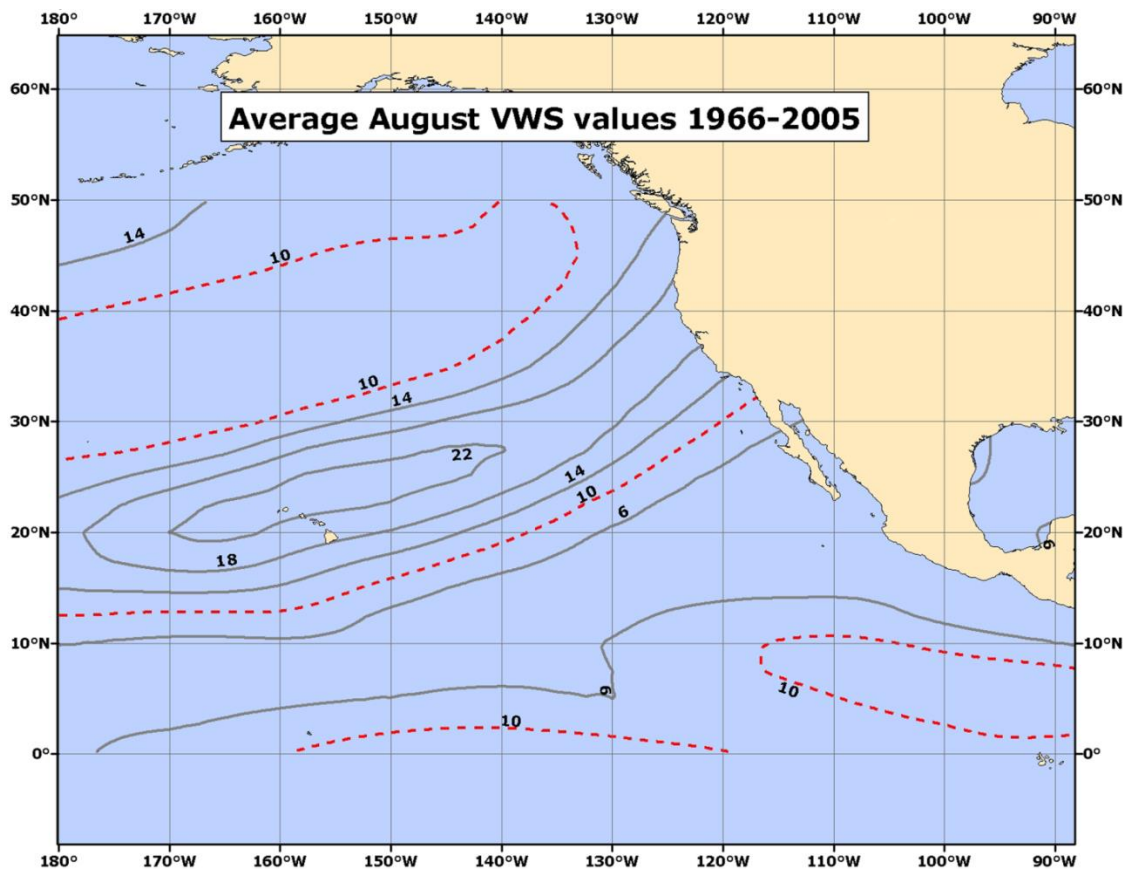


Figure 7. Average August 850-200 hPa VWS values in m s^{-1} from 1966-2005. Adopted from Dettmer (2011).

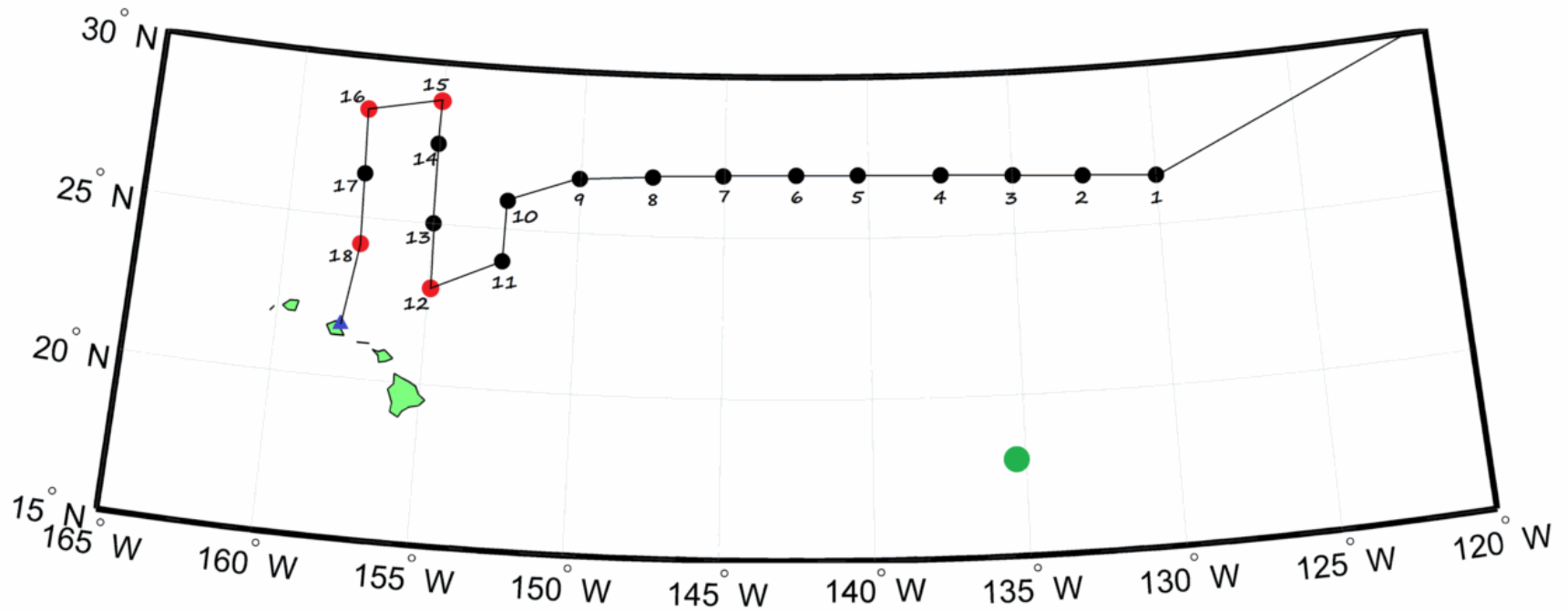


Figure 8. NOAA G-IV surveillance mission of Felicia on 7 August 2009 and chronological deployment distribution of GPS sondes. The red markers denote unsuccessful sonde deployment locations. The green circle is Felicia's low-level circulation center.

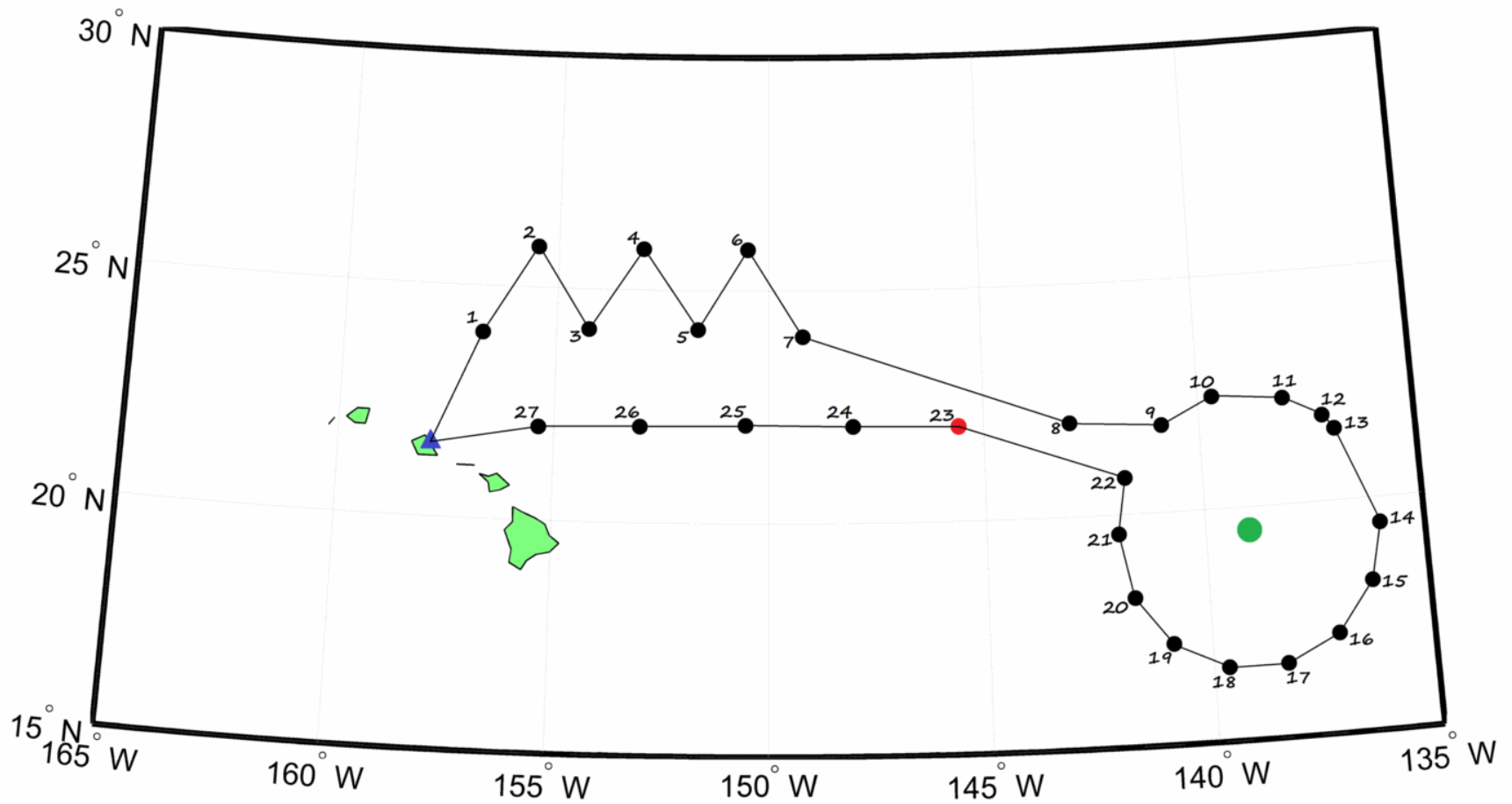


Figure 9. NOAA G-IV surveillance mission on 8 August 2009 and chronological deployment distribution of GPS sondes. The red marker denotes an unsuccessful sonde deployment location. The green circle is Felicia's low-level circulation center.

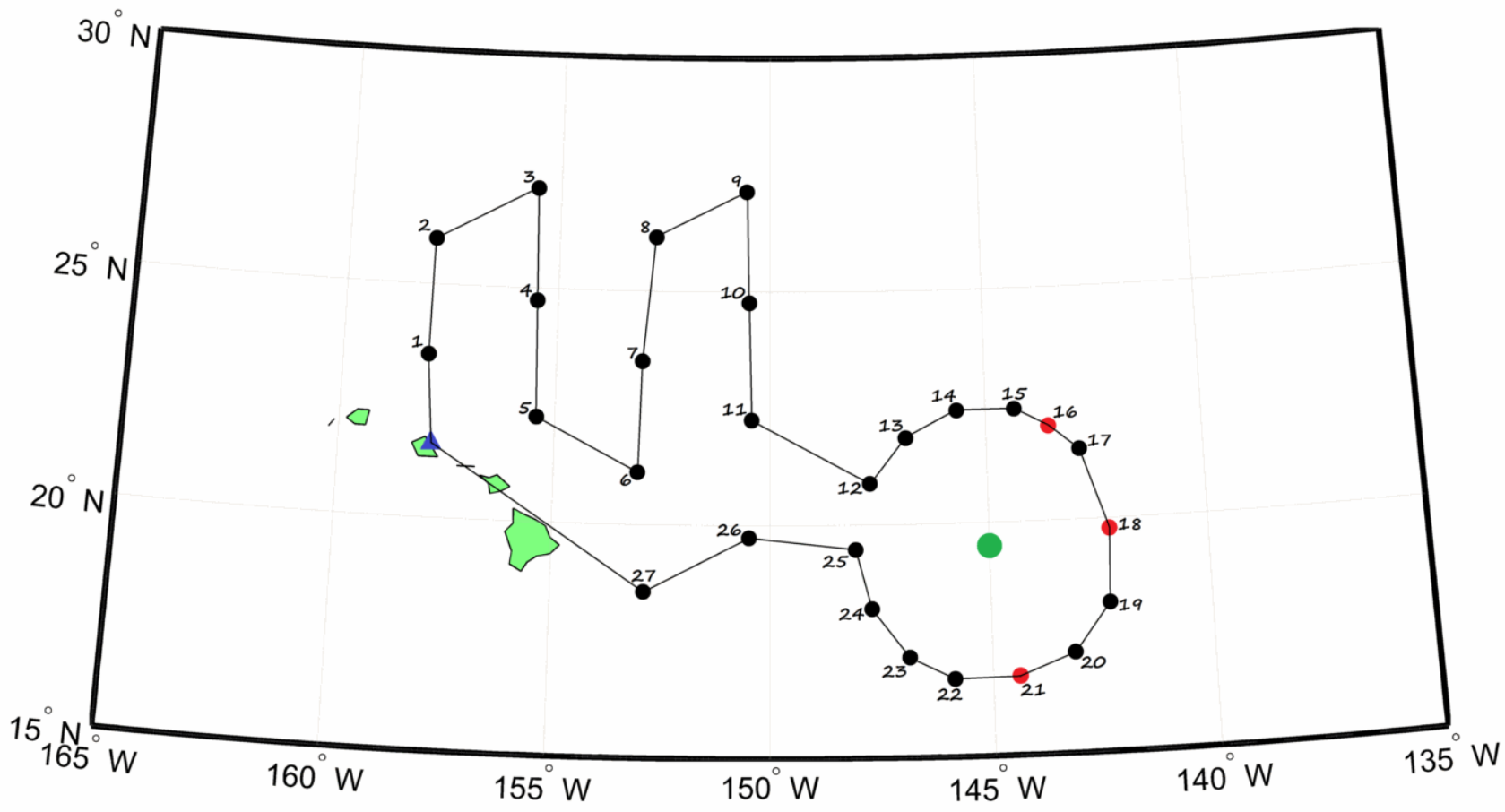


Figure 10. NOAA G-IV surveillance mission on 9 August 2009 and chronological deployment distribution of GPS sondes. The red markers denote unsuccessful sonde deployment locations. The green circle is Felicia's low-level circulation center.

NCAR GPS Dropsonde

the definitive atmospheric profiling tool

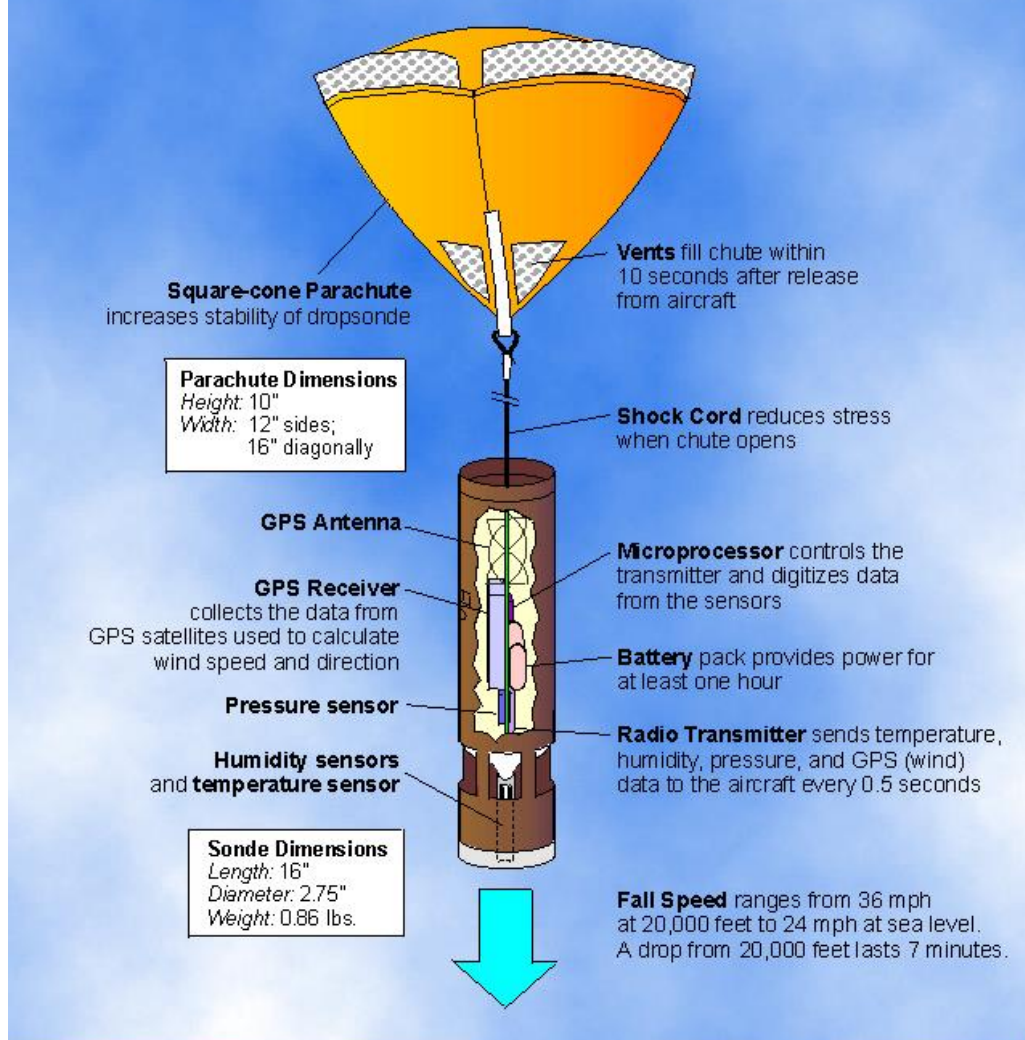


Figure 11. Schematic diagram of the NCAR GPS dropwindsonde used during the G-IV surveillance missions of Hurricane Felicia. (Adopted from NCAR/UCAR Earth Observing Laboratory).

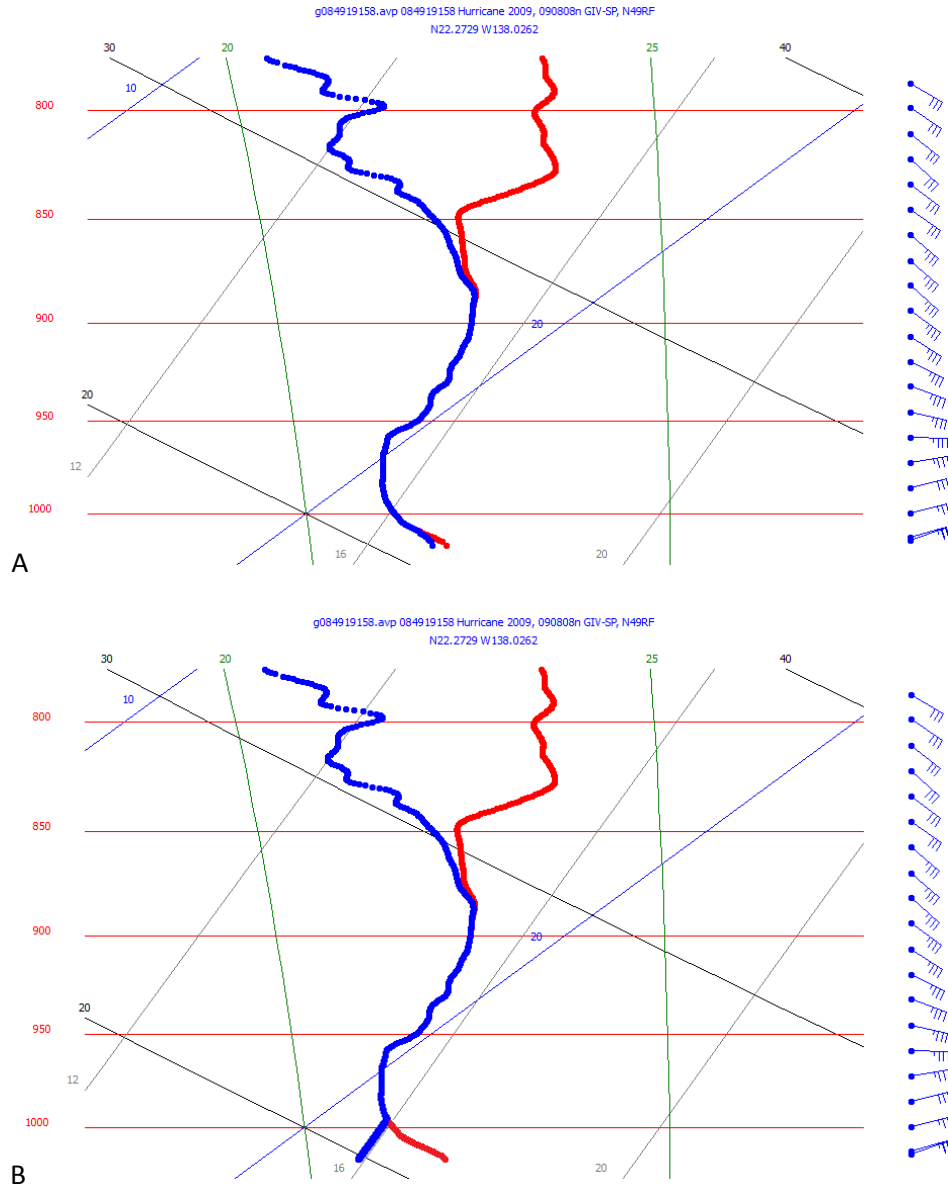


Figure 12. Example of a sensor wetting correction on a skew-T log-P diagram processed with ASPEN from 8 August deployment #11. Pressure is labeled on the left y-axis with thin red horizontal lines from 800 to 1000 hPa. Temperature (thin gray lines) and mixing ratio lines (thin blue lines) run from lower left to upper right, respectively. Dry adiabats are black from lower right to upper left. Moist adiabat lines run nearly vertical in green. GPS sonde measured wind speed and direction are shown on the right y-axis. The vertical profiles of temperature and dewpoint temperature are highlighted by thick red and blue curves. Fig. 5(A) is the original QC skew-T log-P diagram produced by ASPEN while Fig. 5(B) shows the same skew-T with a corrected humidity profile from roughly 990 hPa to the surface.

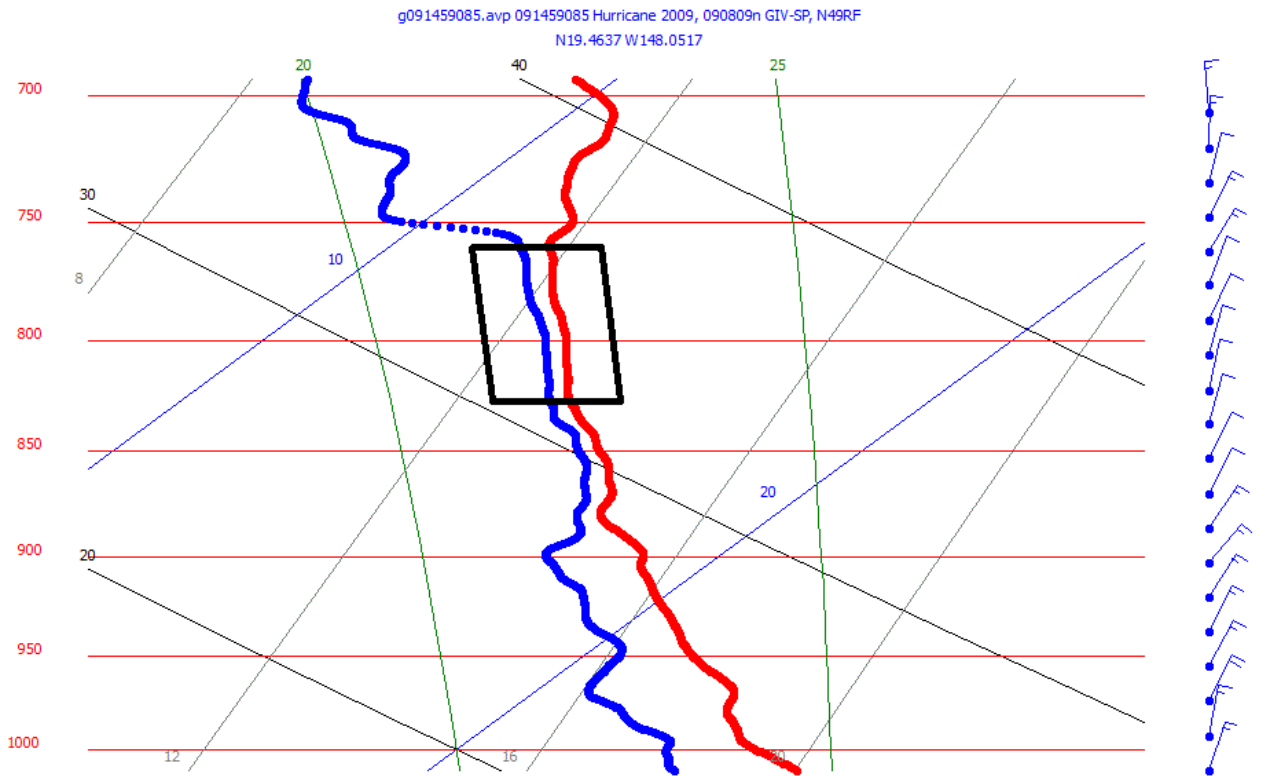


Figure 13. Example of a layer of a skew-T log-P diagram demonstrating a slight departure from a saturated profile. The lines and curves are the same as in Fig. 5. The black box indicates a layer in which the GPS sonde measured a RH >98% while paralleling a moist adiabetic line.

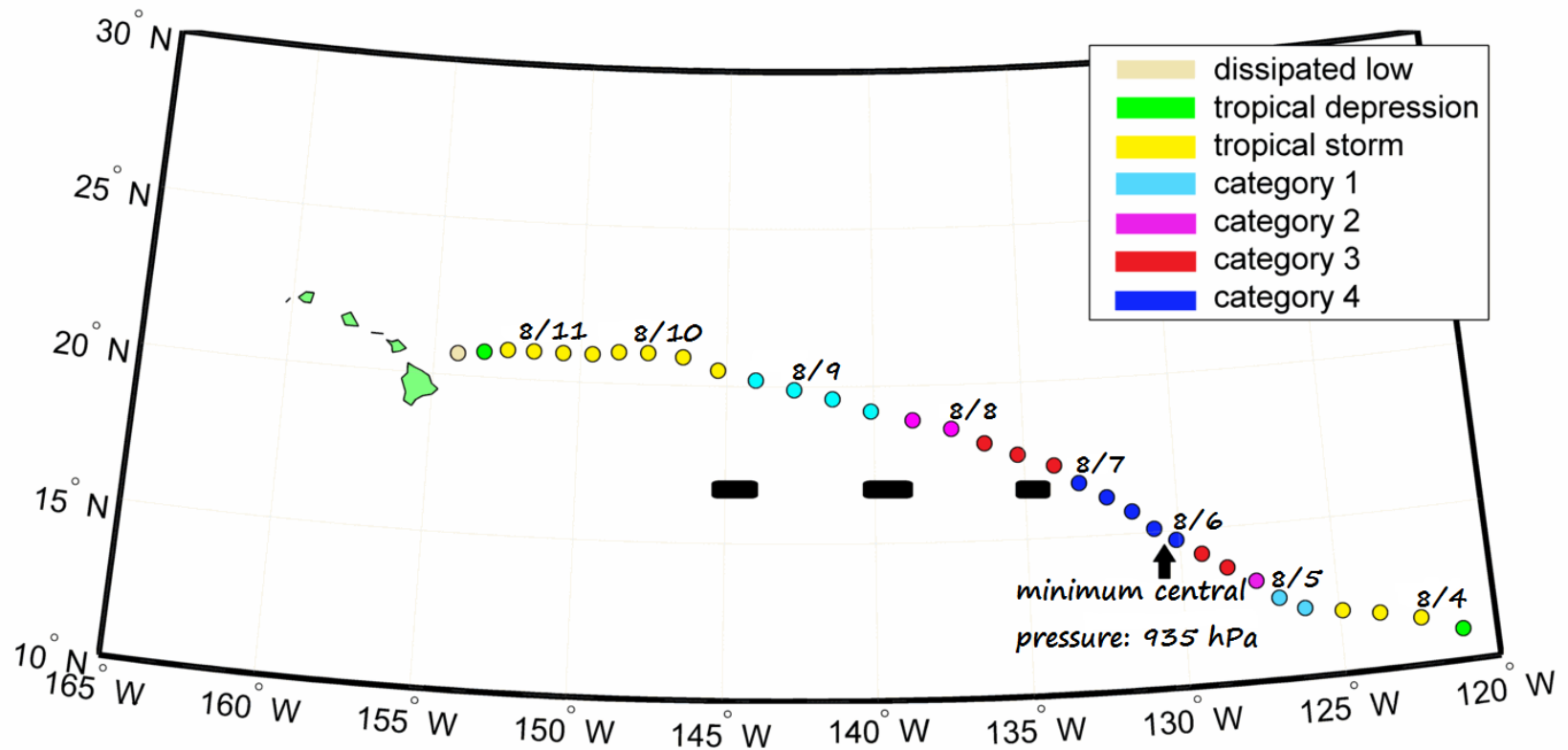


Figure 14. NHC's best track of Hurricane Felicia with center positions every 6 hours. The labeled dates correspond to 0000 UTC on that day. The black horizontal lines denote the sampling periods of the NOAA G-IV aircraft on 8/7, 8/8 and 8/9.

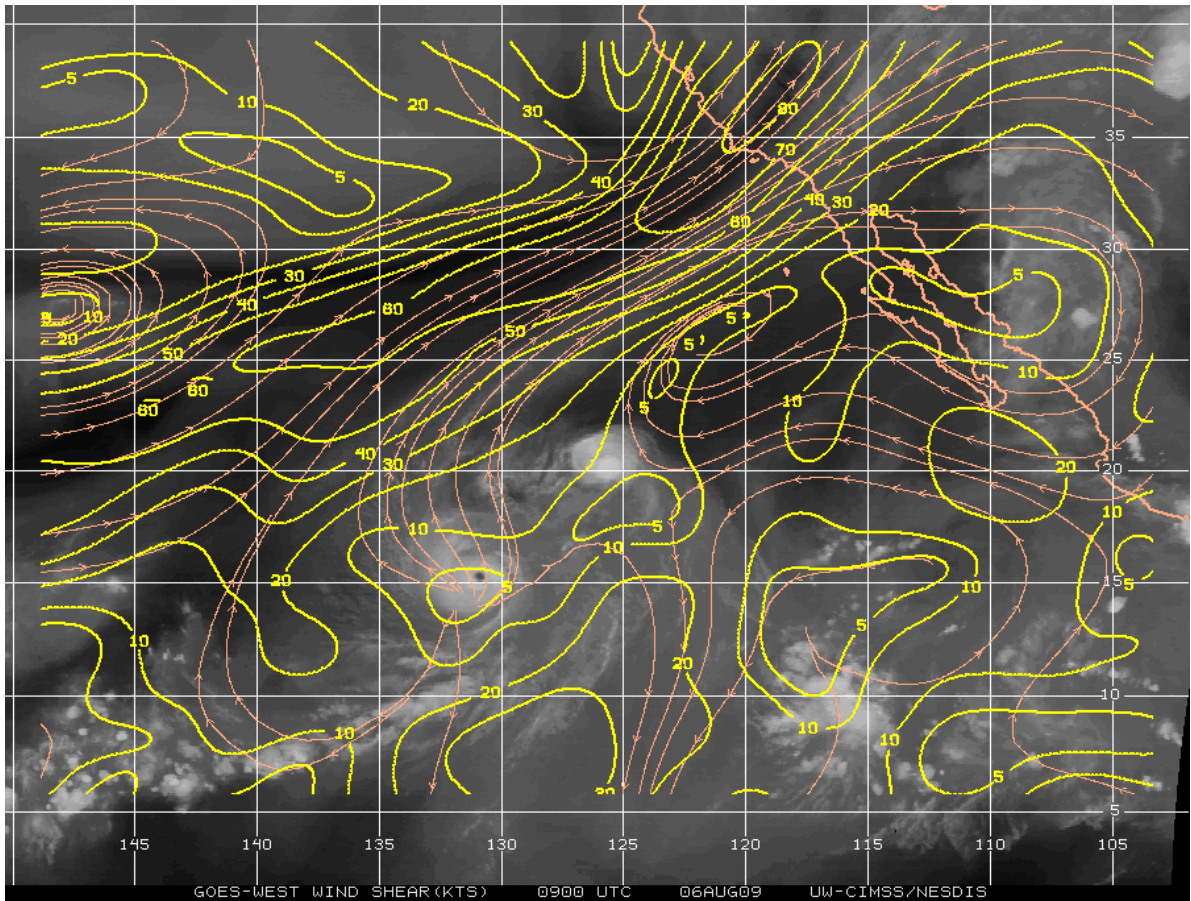


Figure 15. VWS (kts) overlaid on GOES-WEST IR satellite imagery for 0900 UTC 6 August. The yellow contours illustrate the wind shear and are drawn every 10 knots, with inclusion of the 5 knot contour. Streamlines are shown in tan. Felicia is located at 15.5°N , 131.5°W . (Adopted from University of Wisconsin – CIMSS).

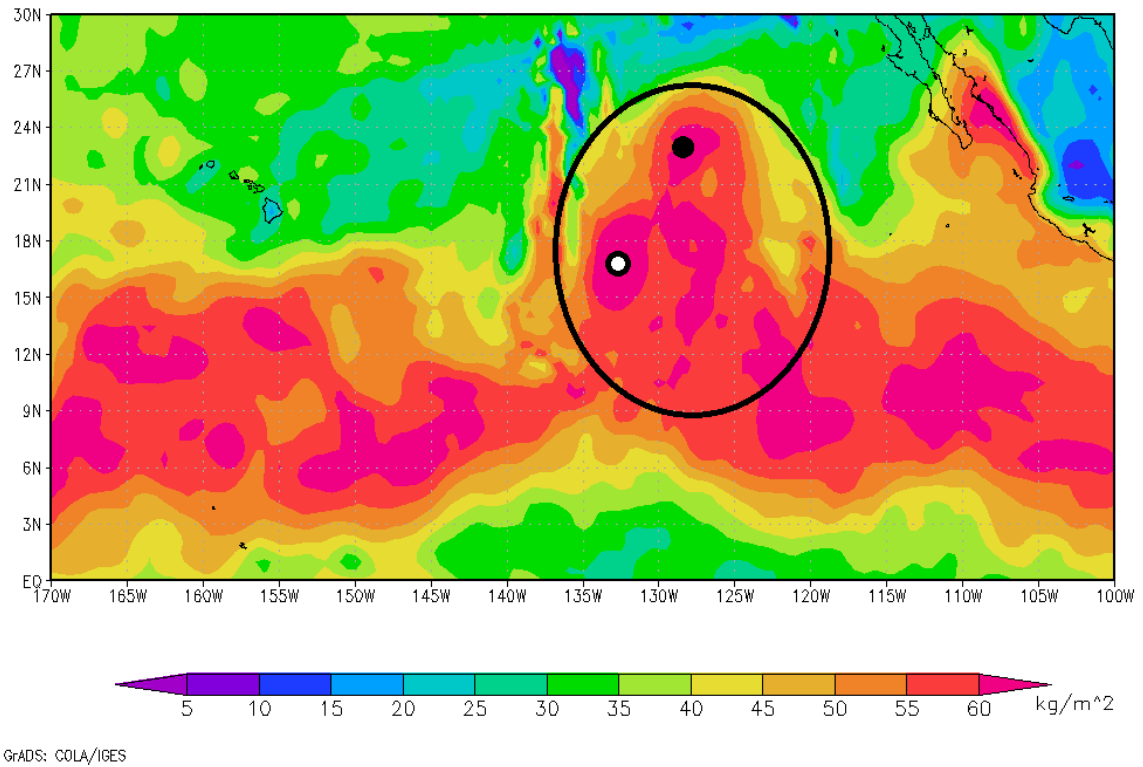


Figure 16. NCEP CFSR total atmospheric precipitable water (kg/m^2) at 0000 UTC 7 August 2009. The large black oval denotes a region of high TPW associated with Hurricane Felicia, TS Enrique, and the NECZ. The black circle with white center is Felicia's low-level circulation center and the full black circle is the low-level circulation center of TS Enrique. Both positions are based upon NHC best track.

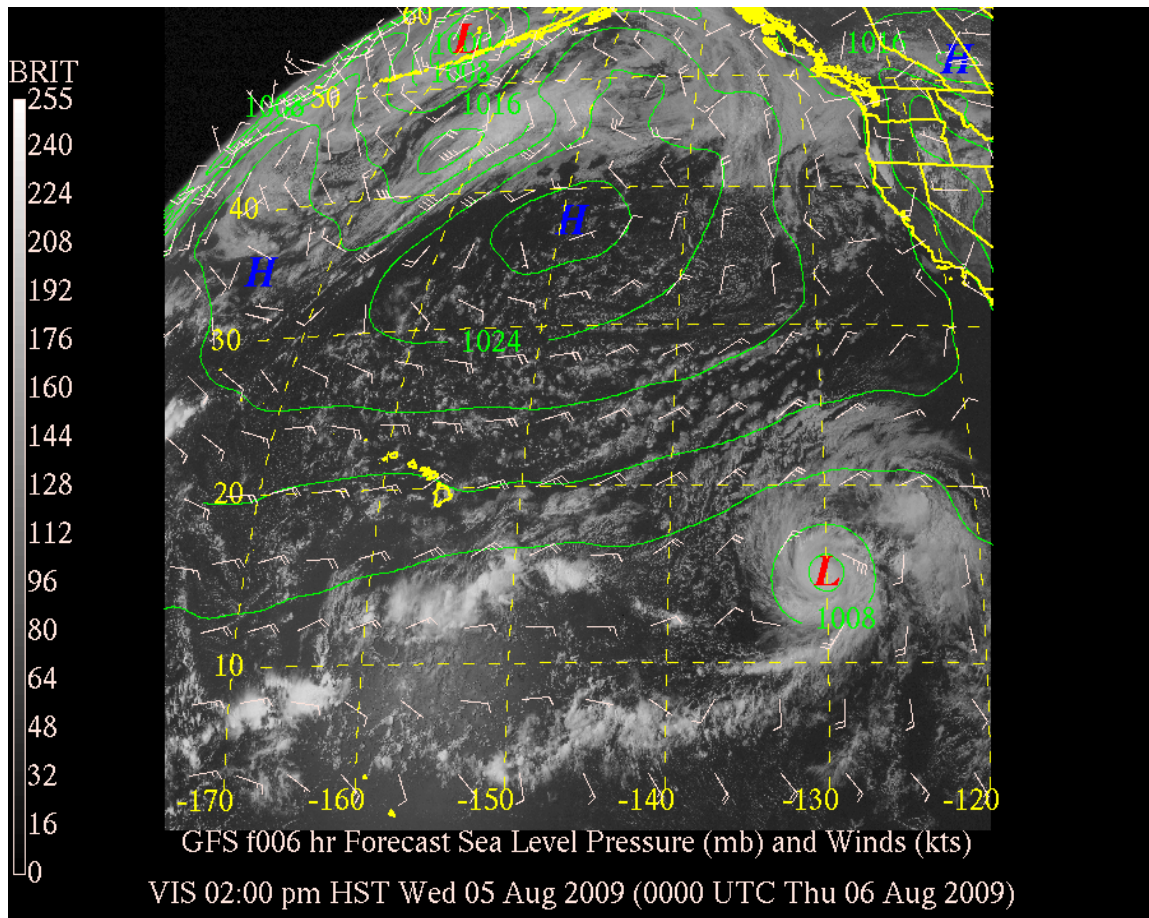


Figure 17. GOES-WEST 0000 UTC 6 August 2009 visible satellite imagery and 0600 h GFS forecasted model overlay of sea level pressure (mb) and winds (kts). (Adopted from Mauna Kea Weather Center Archive).

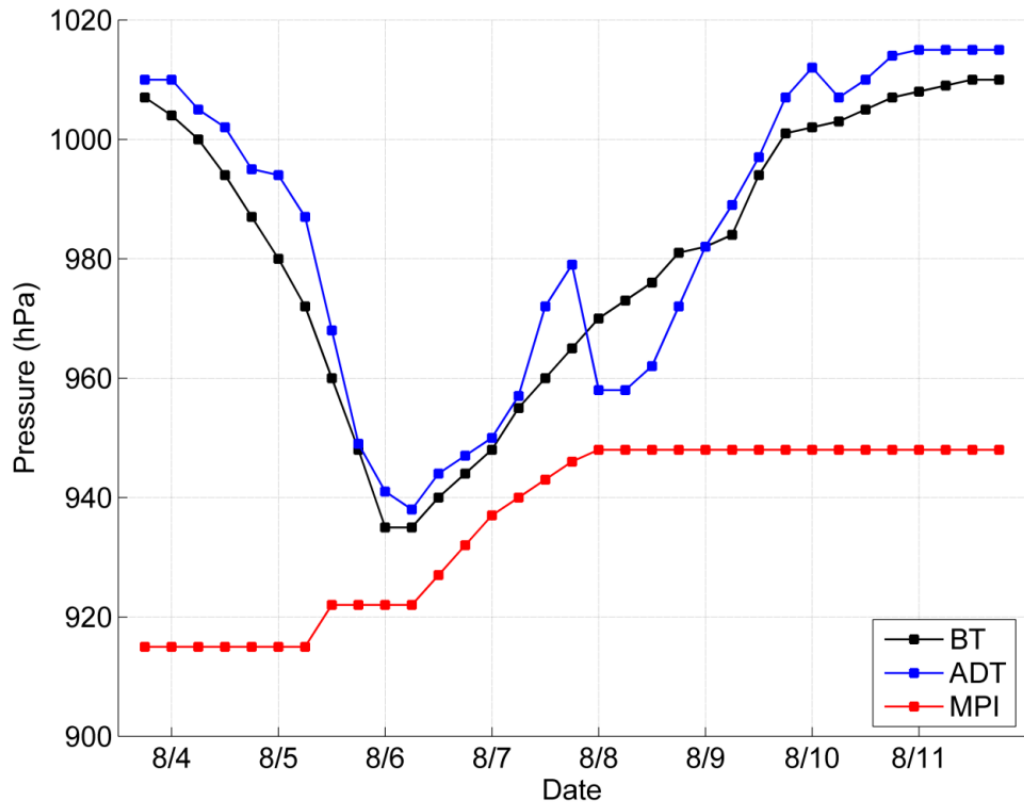


Figure 18. The evolution of Hurricane Felicia's central pressure based on three approaches; NHC's best track, CIMSS Advanced Dvorak Technique, and MPI theory.

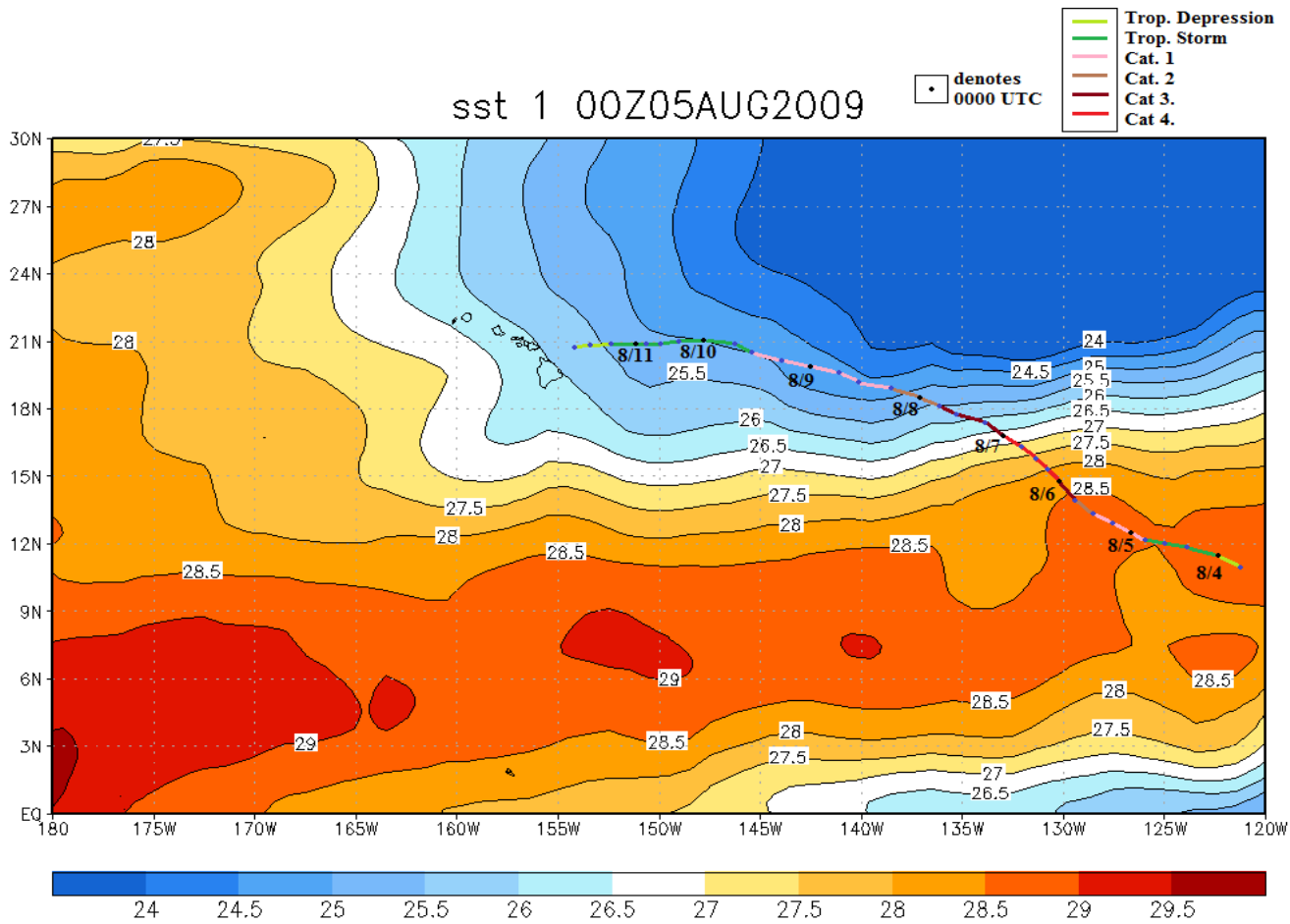
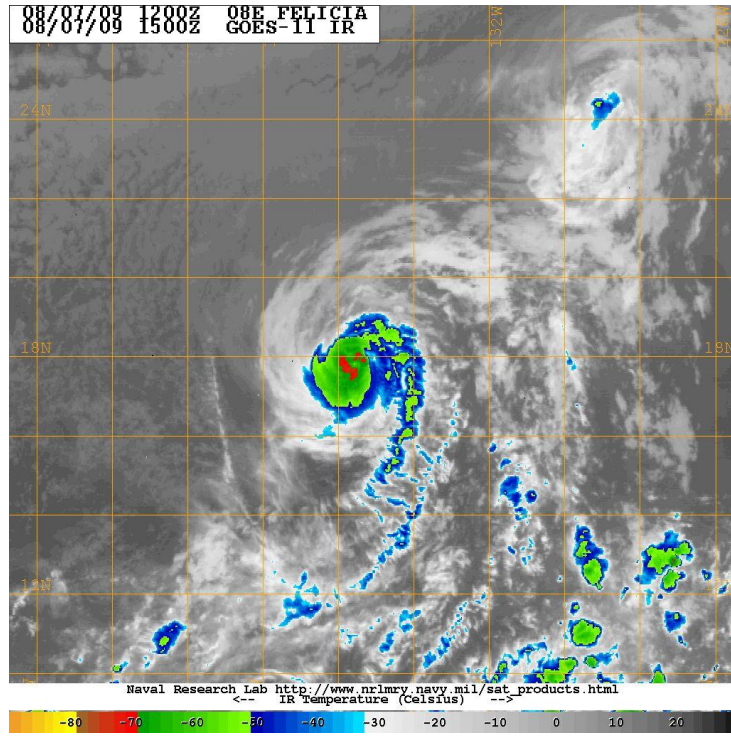
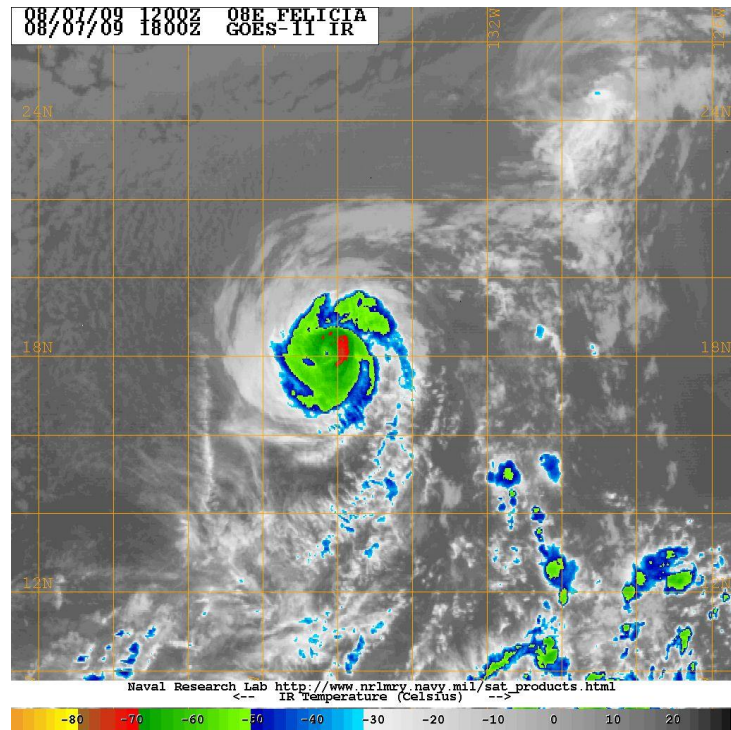


Figure 19. NOAA OIV2 weekly averaged satellite derived SSTs ($^{\circ}\text{C}$) beginning 0000 UTC 5 August 2009 for the domain 180°W to 120°W , 0°N to 30°N . Overlaid on this SST field is the complete track of Hurricane Felicia based upon best track. Black dots denote 0000 UTC of the labeled day. (Adapted from NOAA).



(a)



(b)

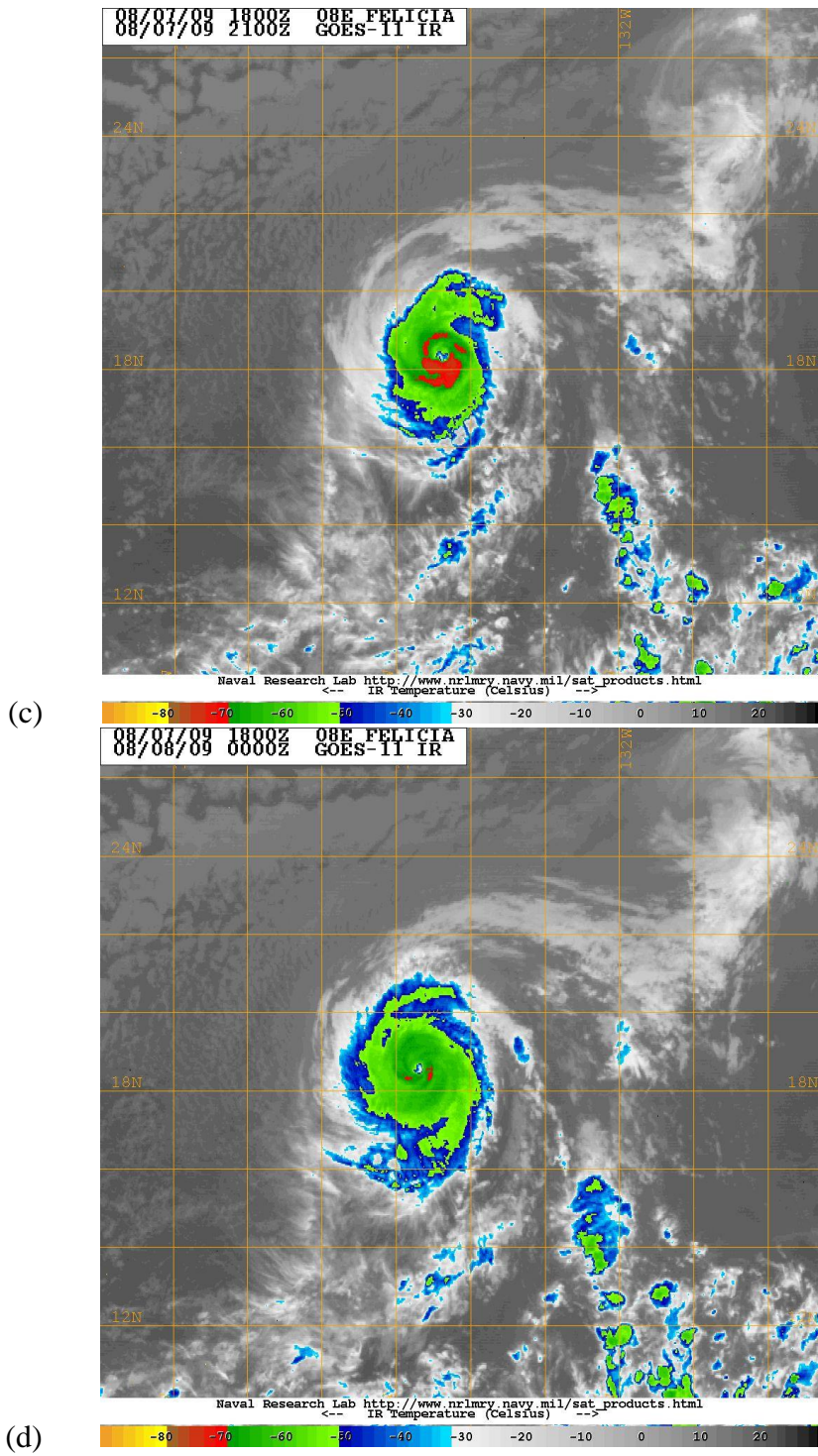


Figure 20. Color enhanced IR satellite imagery on (a) 1500 UTC 7 August (b) 1800 UTC 7 August (c) 2100 UTC 7 August and (d) 0000 UTC 8 August. Green color is $<-50^{\circ}\text{C}$, red is $<-70^{\circ}\text{C}$.

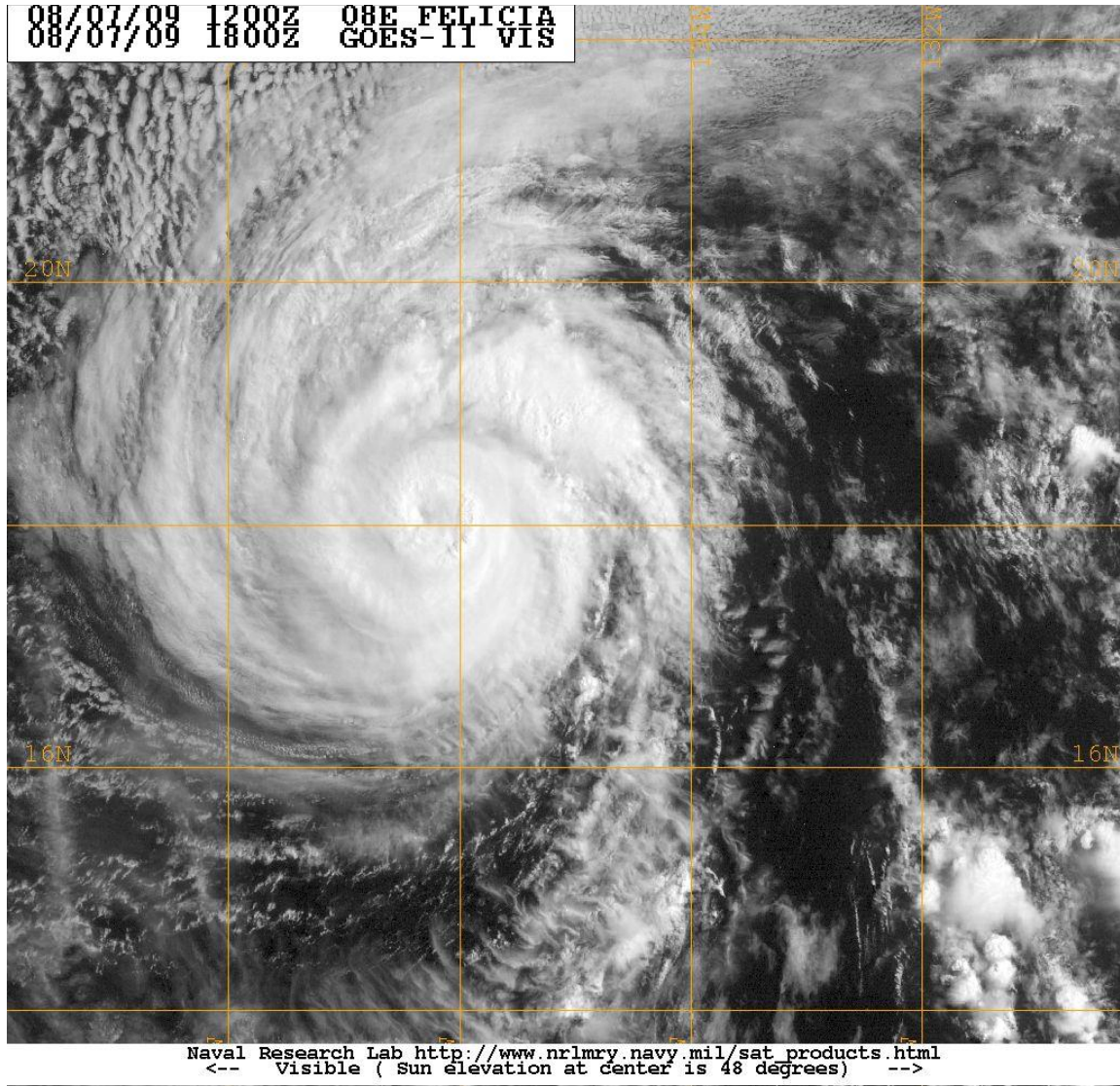


Figure 21. Visible satellite imagery of Hurricane Felicia at 1800 UTC 7 August. Grid is every 2 degrees latitude or longitude.

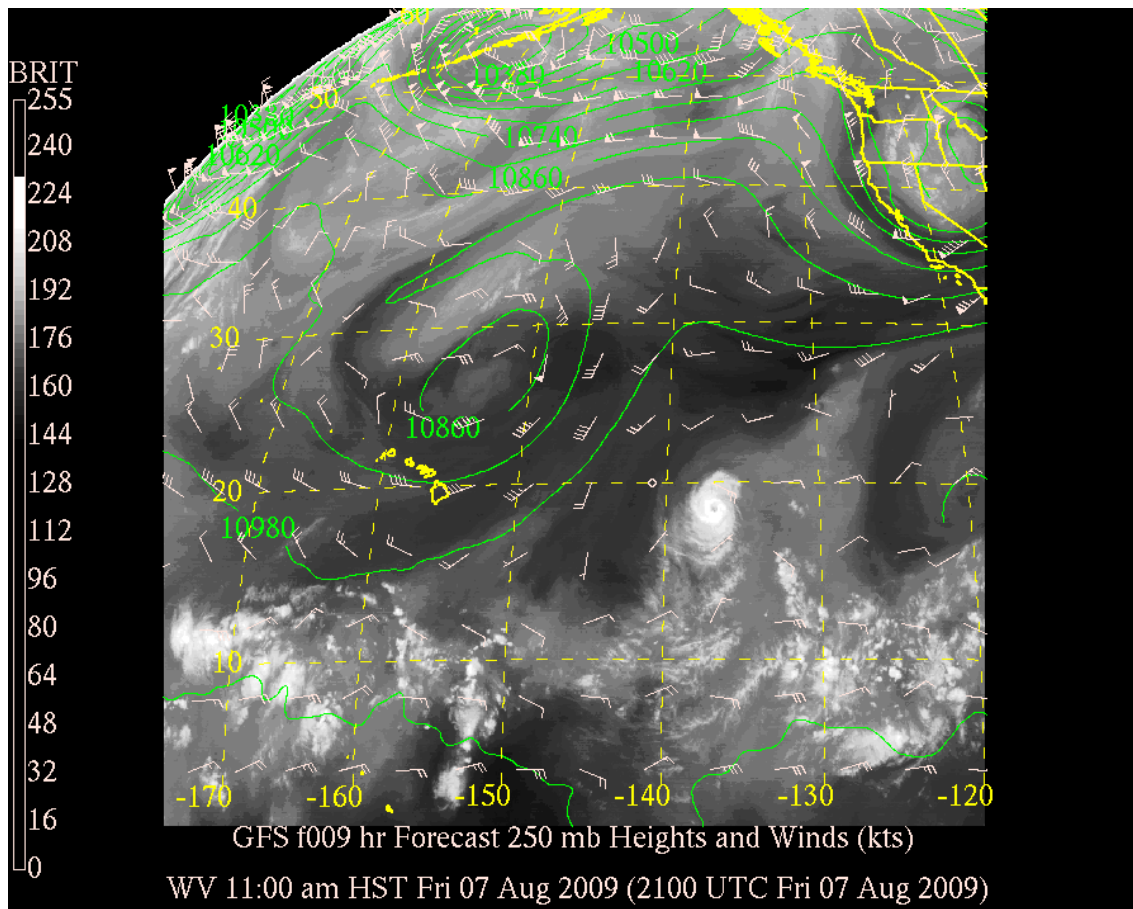


Figure 22. GOES-WEST water vapor imagery at 2100 UTC 7 August and 0900 h forecasted GFS model overlay of 250 heights (mb) and winds (kts). (Adopted from Mauna Kea Weather Center Archive).

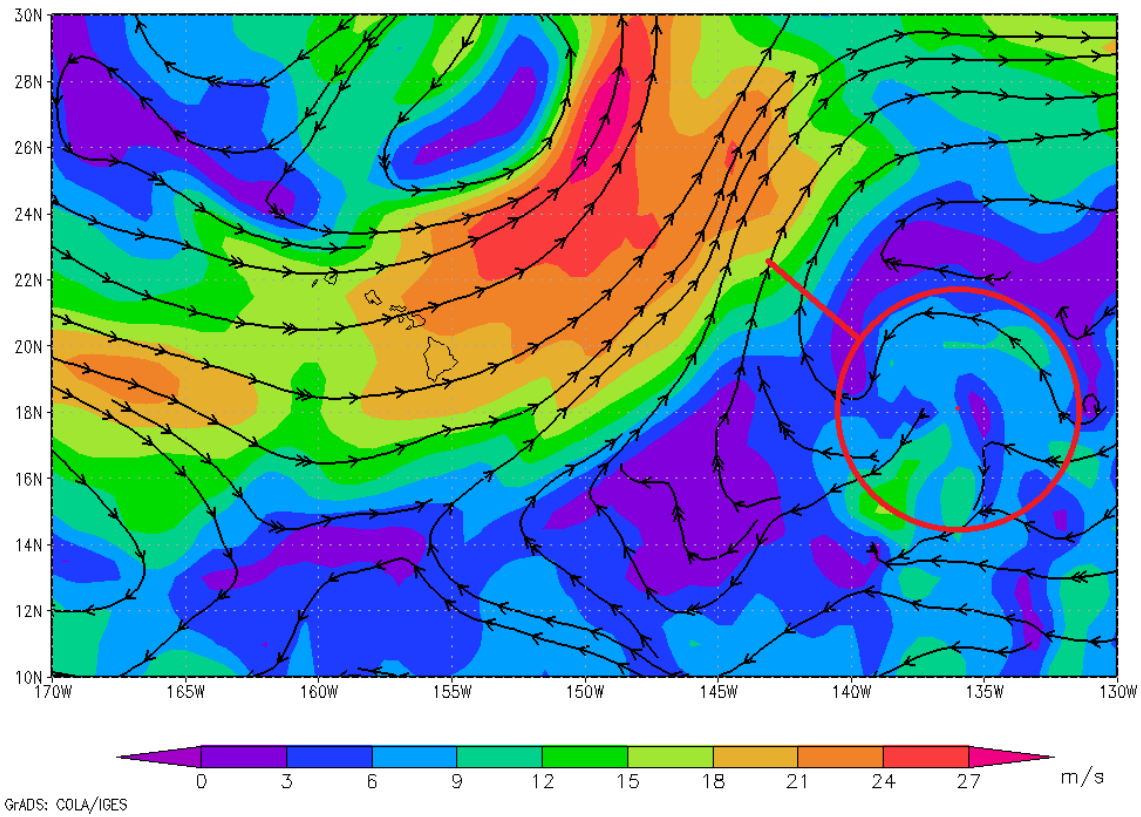


Figure 23. NCEP CFSR 250 hPa winds (m s^{-1}) at 1800 UTC 7 August 2009 with overlay of “separation distance” methodology. The red circle delineates the extent of anticyclonic outflow associated with Hurricane Felicia based on GOES-WEST visible satellite imagery. The red line is the separation distance between the STJ’s $15\text{-}18 \text{ m s}^{-1}$ winds and the anticyclonic outflow.

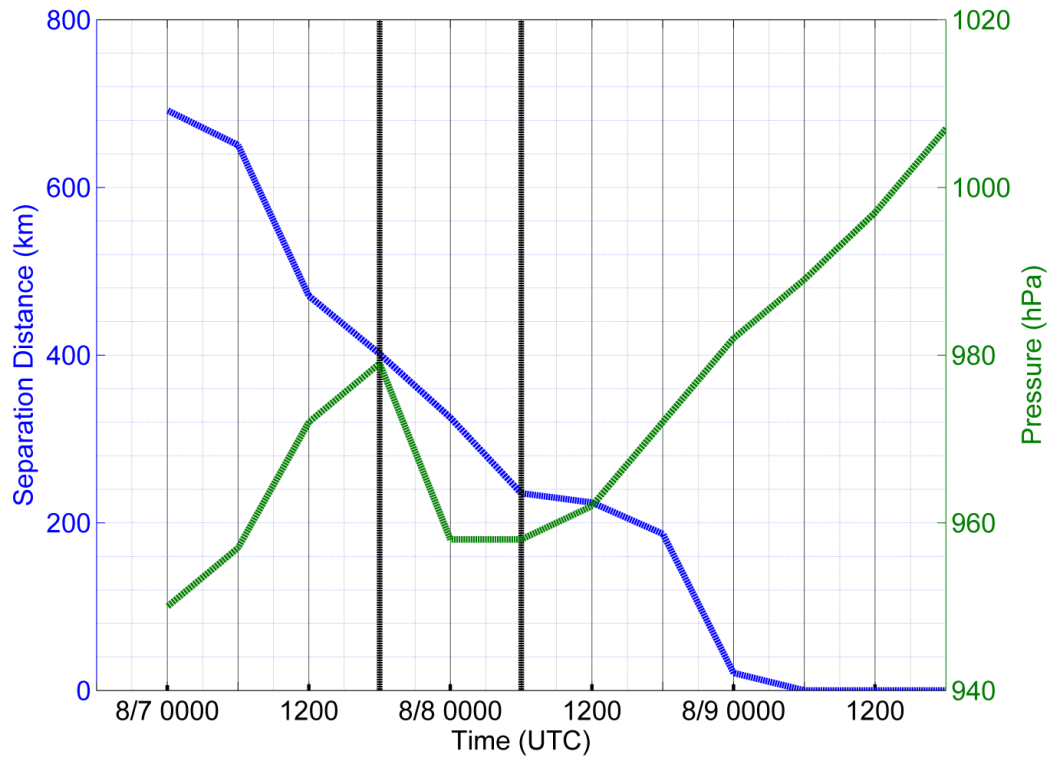


Figure 24. Separation distance (blue) and Felicia's central pressure measured by CIMSS ADT (green) as a function of time. The section of the graph partitioned by vertical black lines highlights the re-intensification as estimated by CIMSS using the ADT.

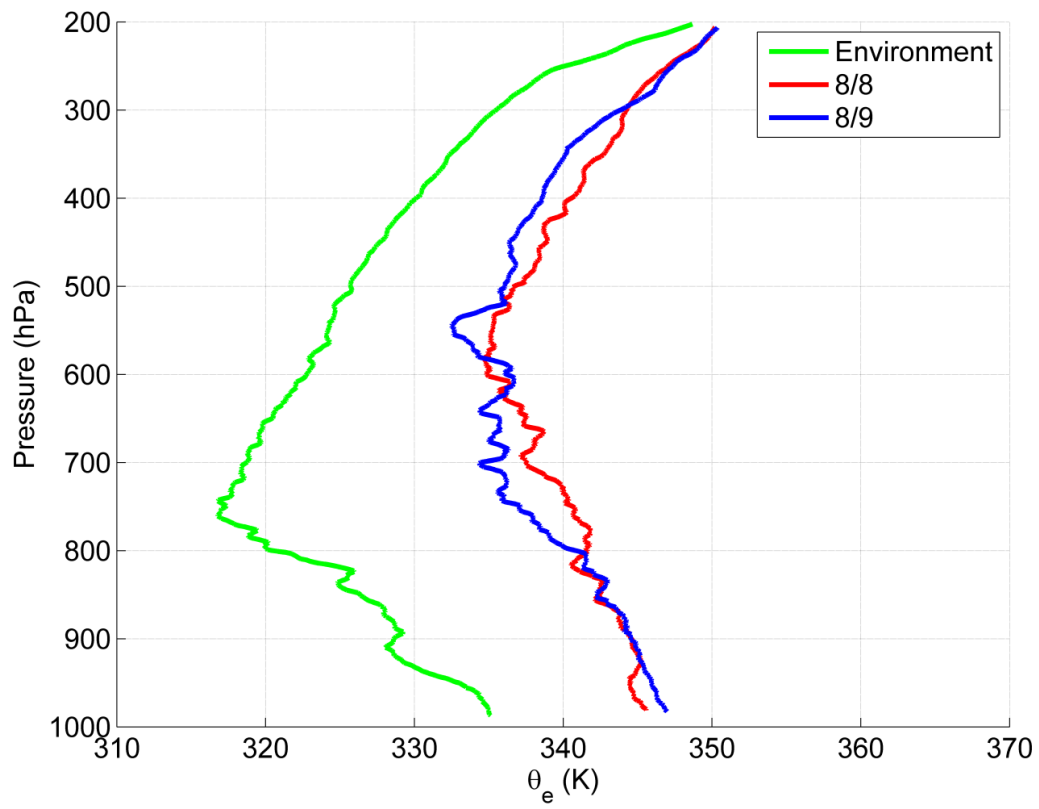


Figure 25. Layer averaged vertical profiles of θ_e for the environment to the NW of Felicia on 8-9 August (green), and the circumnavigations on 8 August and 9 August are represented by red and blue, respectively.

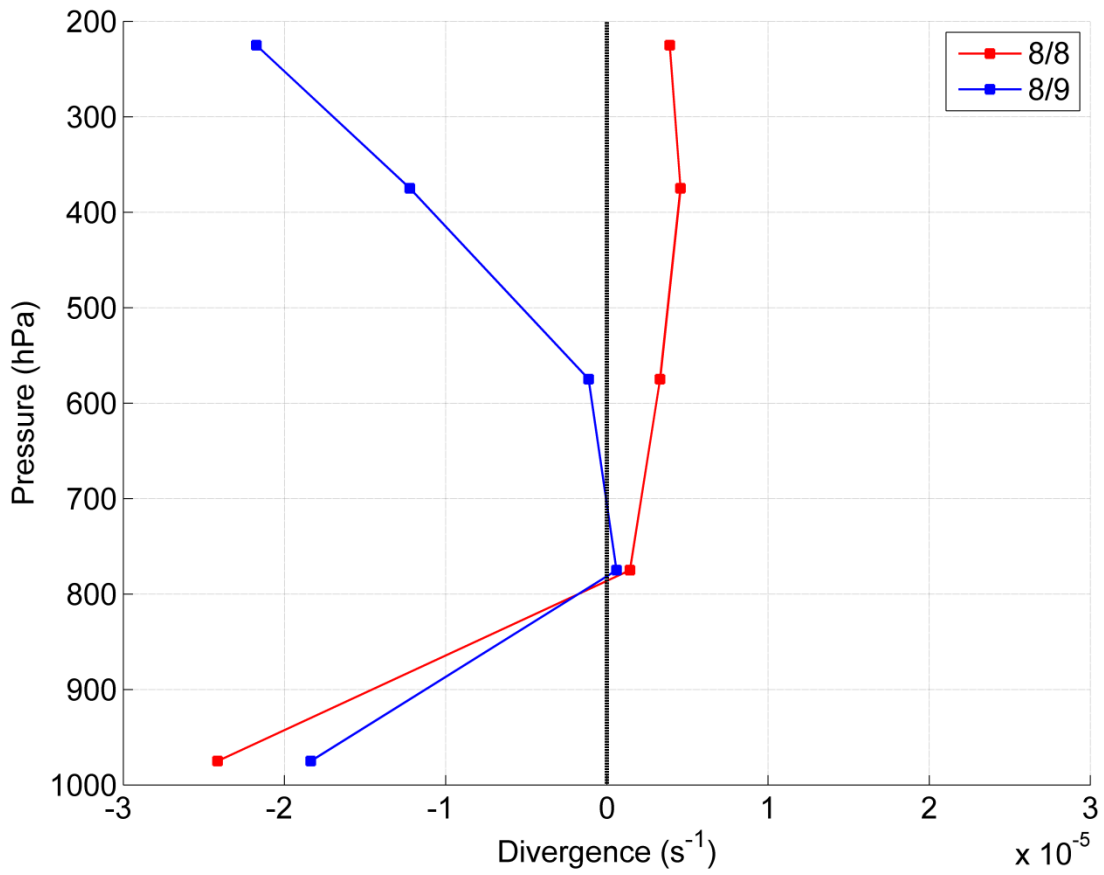


Figure 26. Divergence associated with the 3-degree circumnavigation of Felicia. Divergence values are multiplied by 10^{-5} .

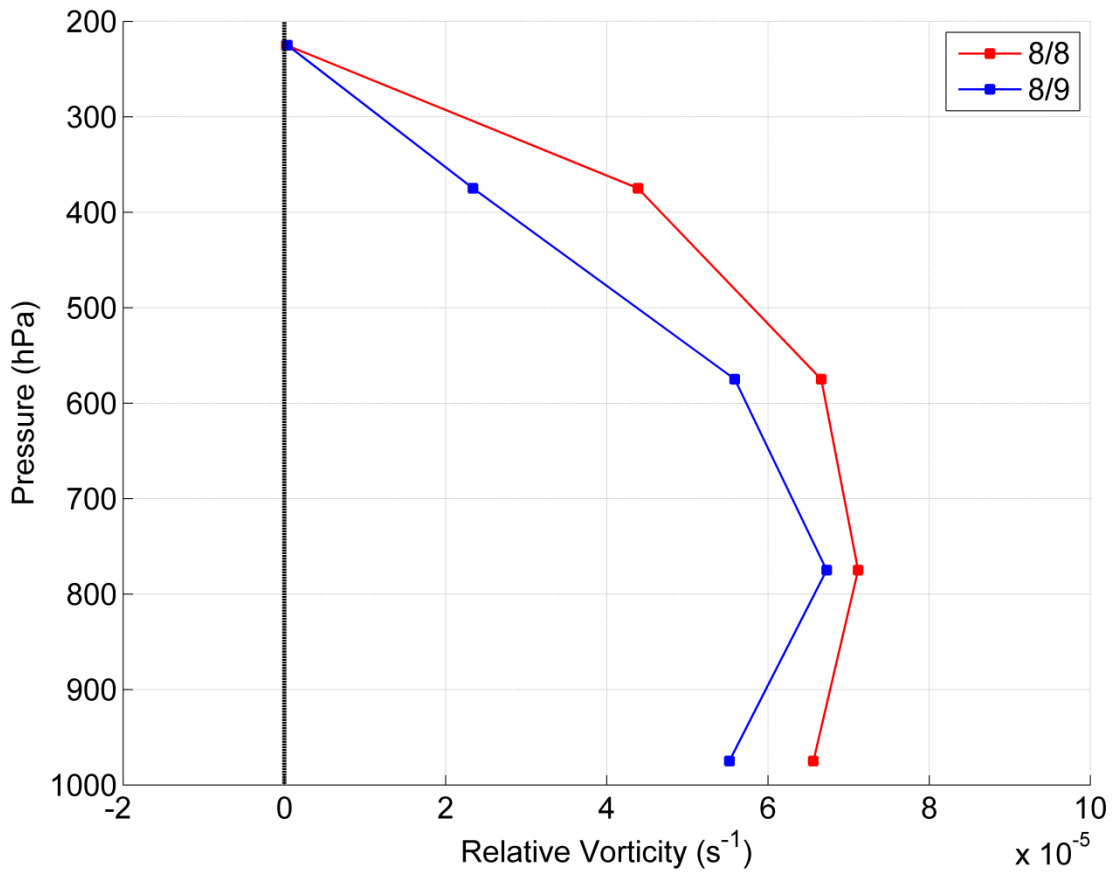
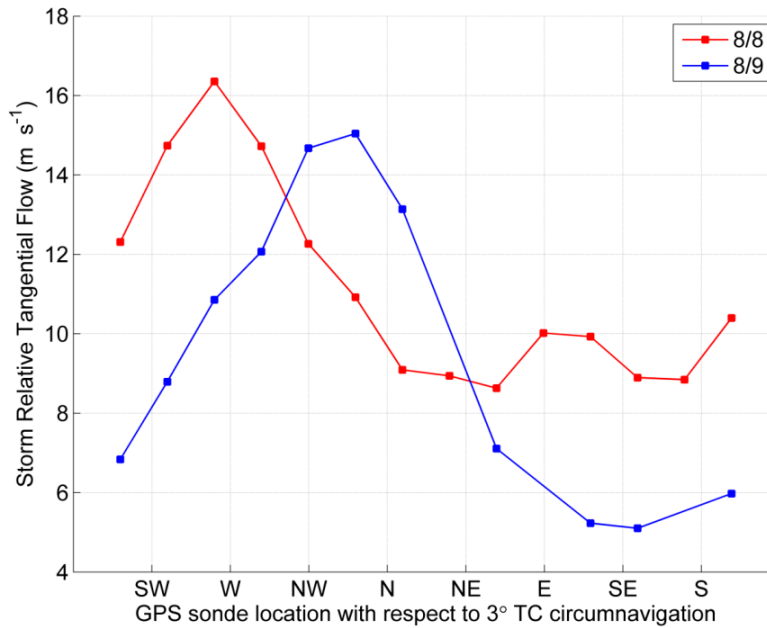
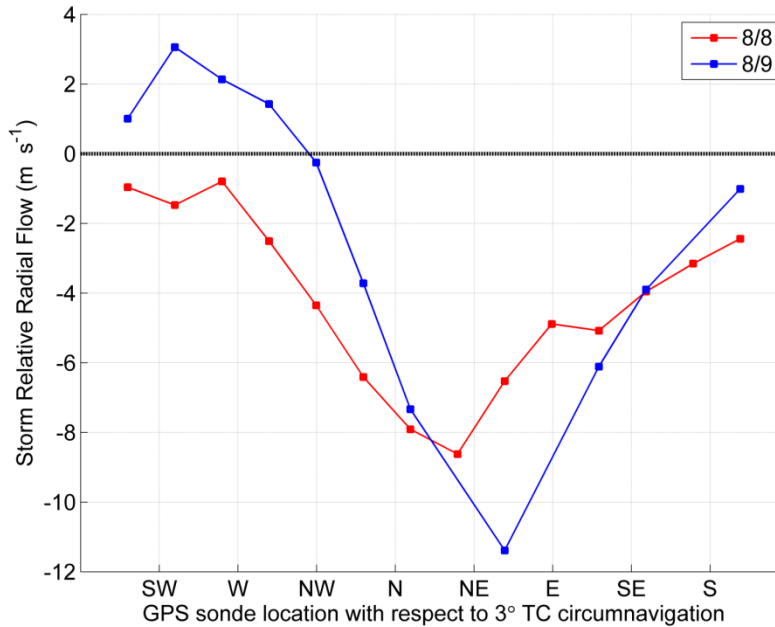


Figure 27. Relative vorticity associated with the 3-degree circumnavigation of Felicia. Relative vorticity values are multiplied by 10^{-5} .



(a)



(b)

Figure 28. Storm relative tangential flow (a) and storm relative radial flow (b) along circumnavigation at 975 hPa. Each datum describes the deployment position on the circumnavigated ring starting at the SW quadrant and rotating clockwise. In (a) positive tangential flow values are cyclonic and negative values are anticyclonic. In (b) positive values are outflow and negative values are radial inflow. The data on the 8th and 9th is shown in red and blue, respectively.

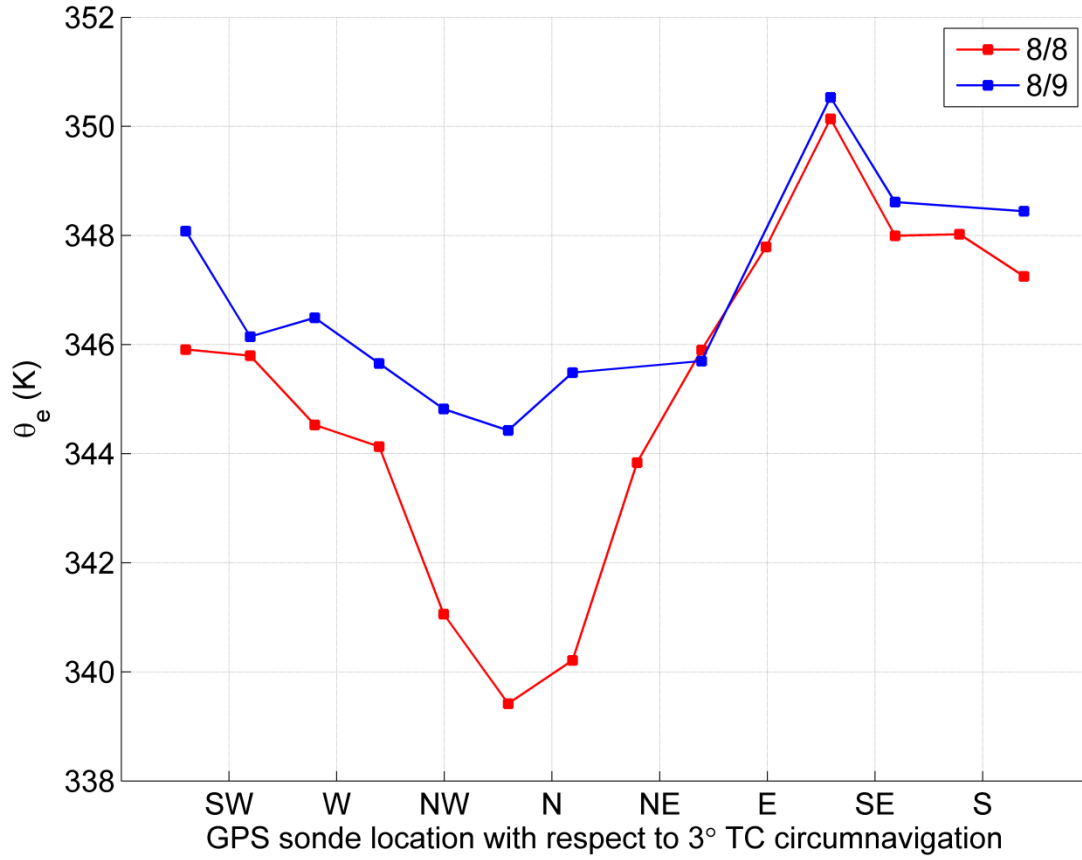


Figure 29. θ_e values along circumnavigation at 975 hPa. Each datum describes the deployment position on the circumnavigated ring starting at the SW quadrant and rotating clockwise. The data on the 8th and 9th is shown in red and blue, respectively.

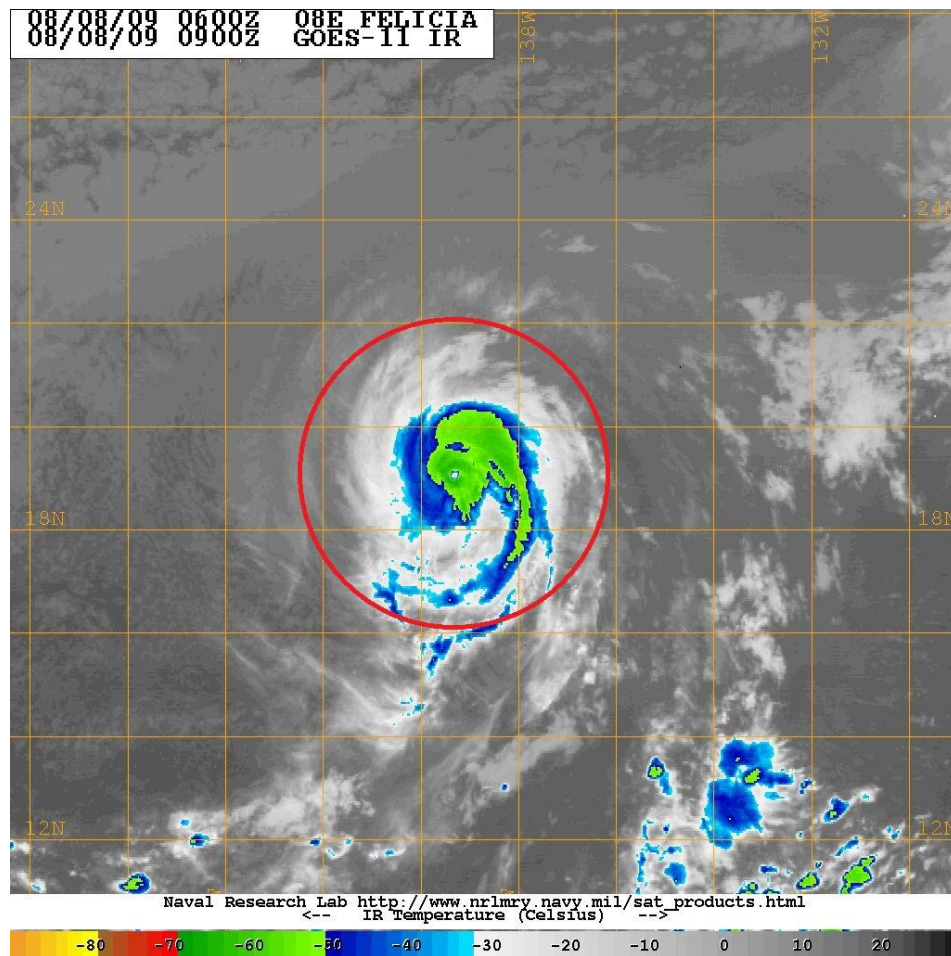
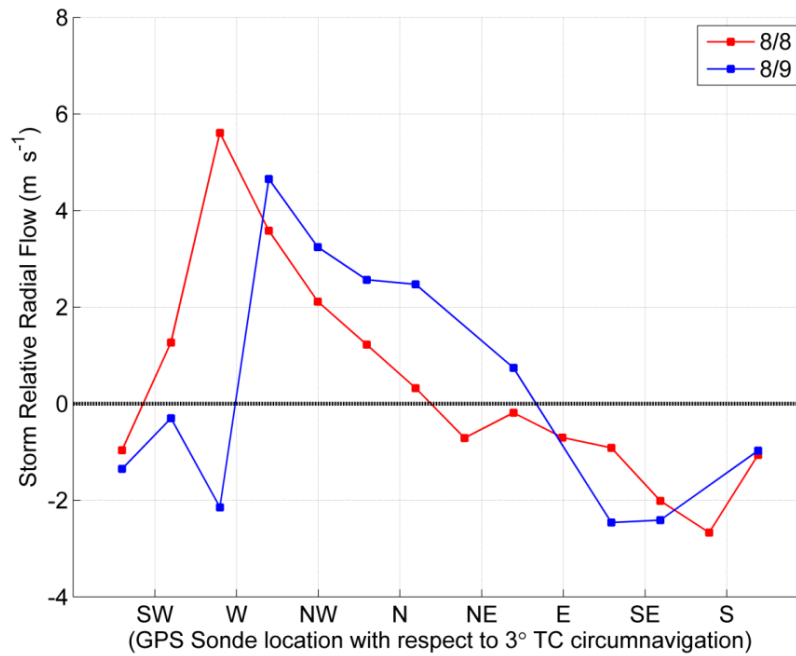
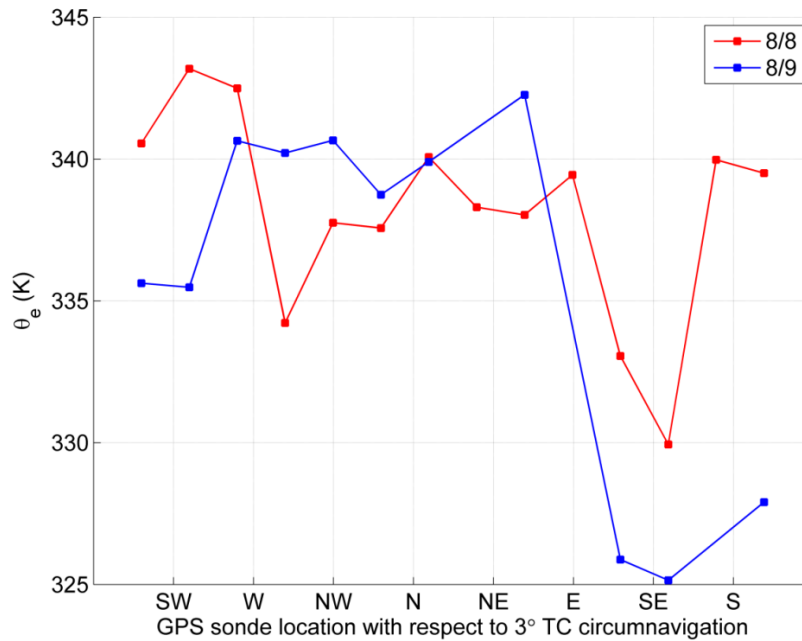


Figure 30. IR satellite image of Hurricane Felicia at 0900 UTC 8 August. A circumnavigation of 3-degrees latitude is represented by the red circle.

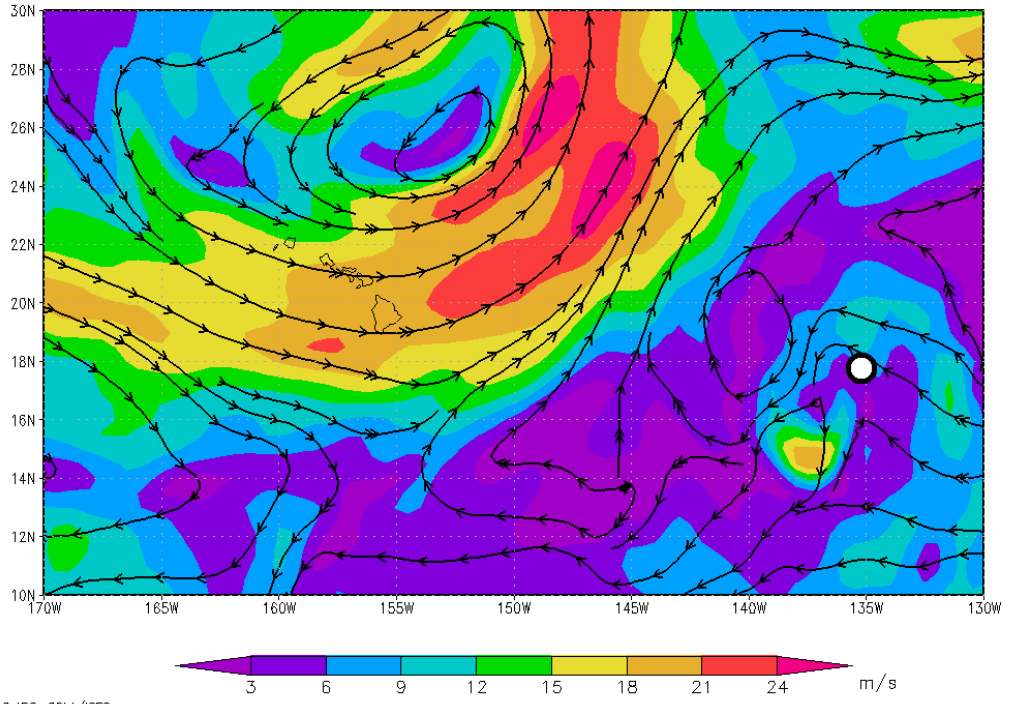


(a)

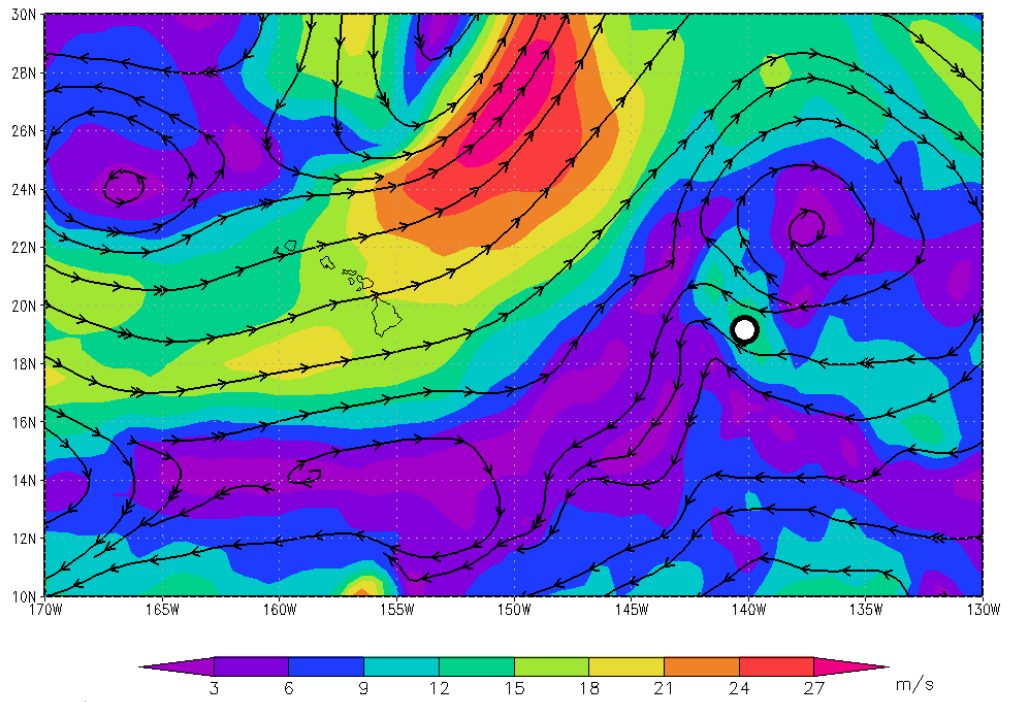


(b)

Figure 31. Storm relative radial flow (a) and θ_e (b) at 700 hPa. In (a), positive values are outflow and negative values are radial inflow. Each datum describes the deployment position on the circumnavigated ring starting at the SW quadrant and rotating clockwise. Red depicts the observations on the 8th and blue shows the observations during the sampling period on the 9th.



(a) GRADS: COLA/IGES



(b) GRADS: COLA/IGES

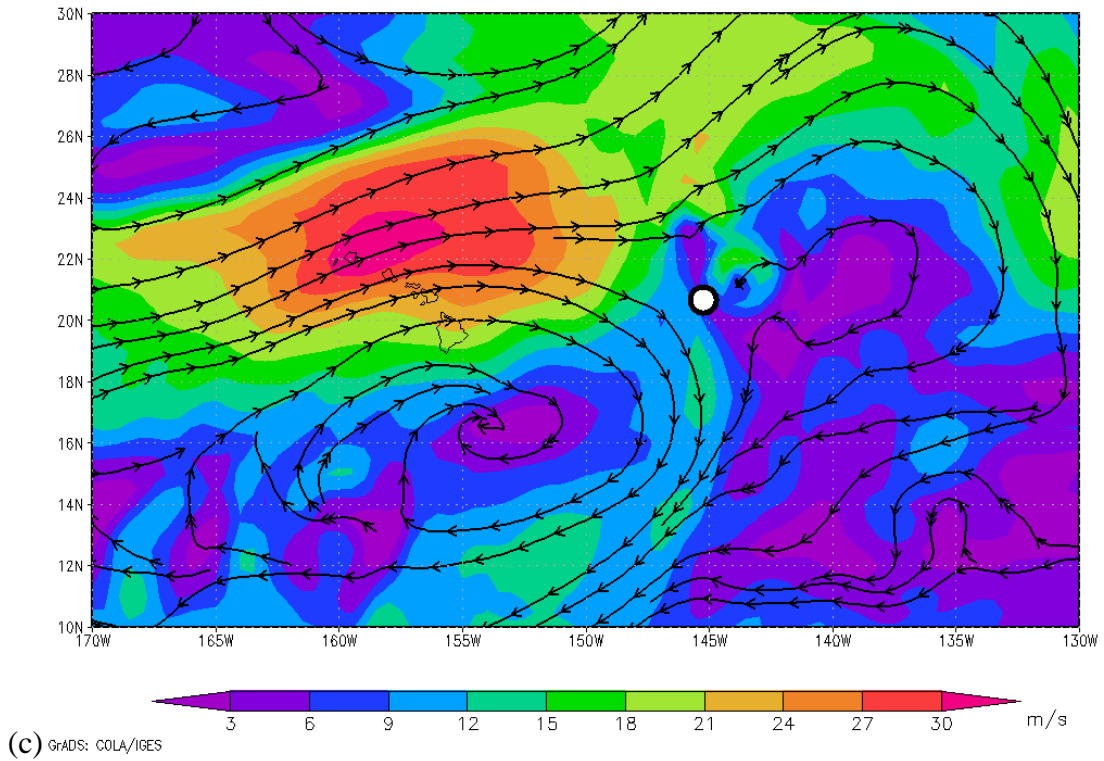
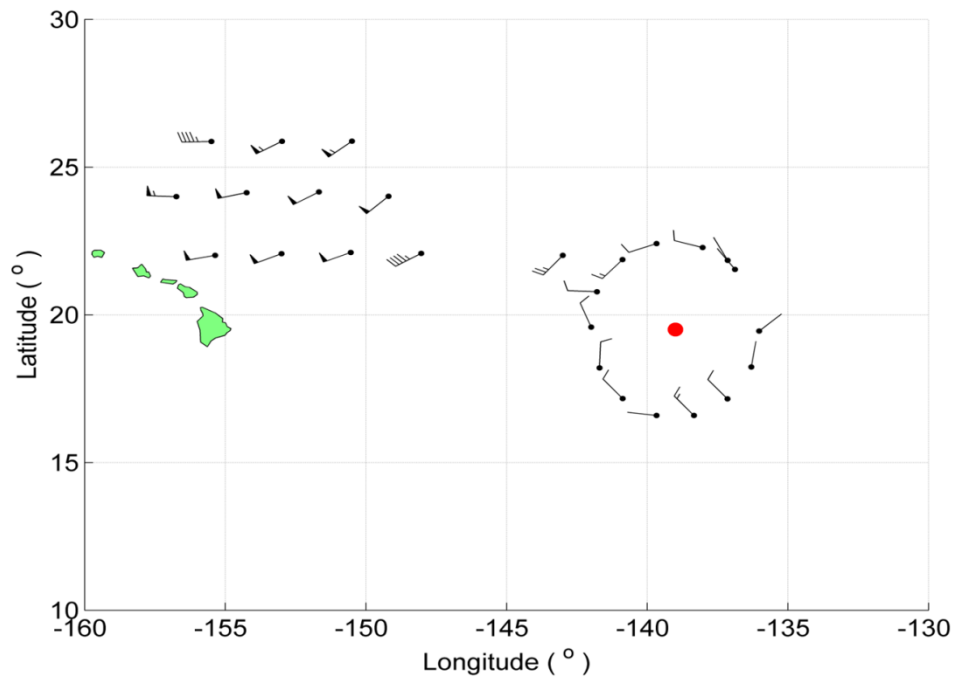
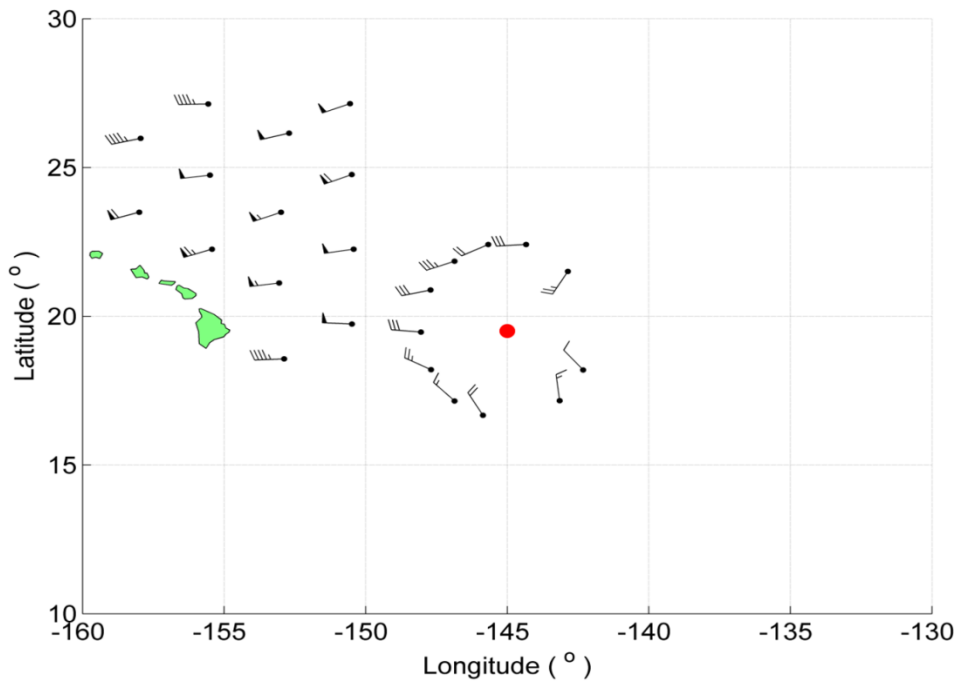


Figure 32. NCEP CFSR 250 hPa winds (m/s) for (a) 1200 UTC 7 August, (b) 1200 UTC 8 August, and (c) 1200 UTC 9 August. The low-level circulation center of Felicia in each panel is represented by the white and black circle.

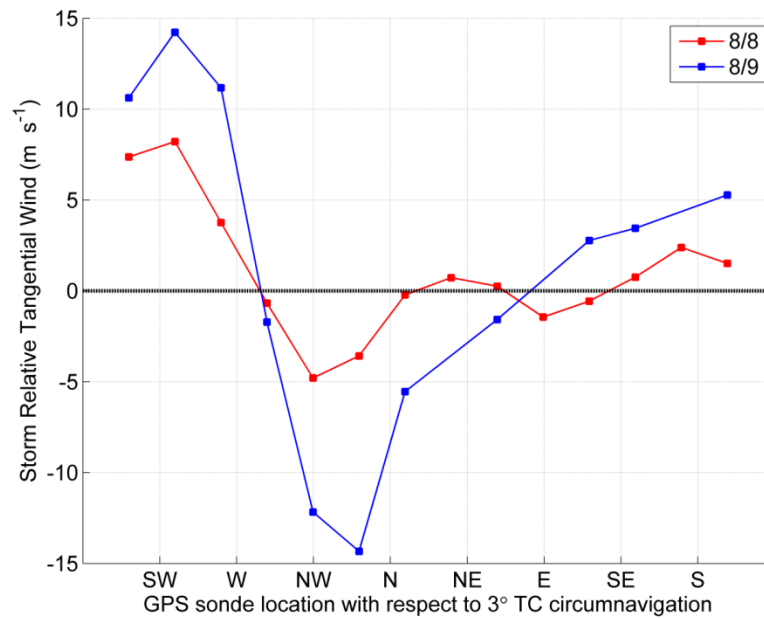


(a)

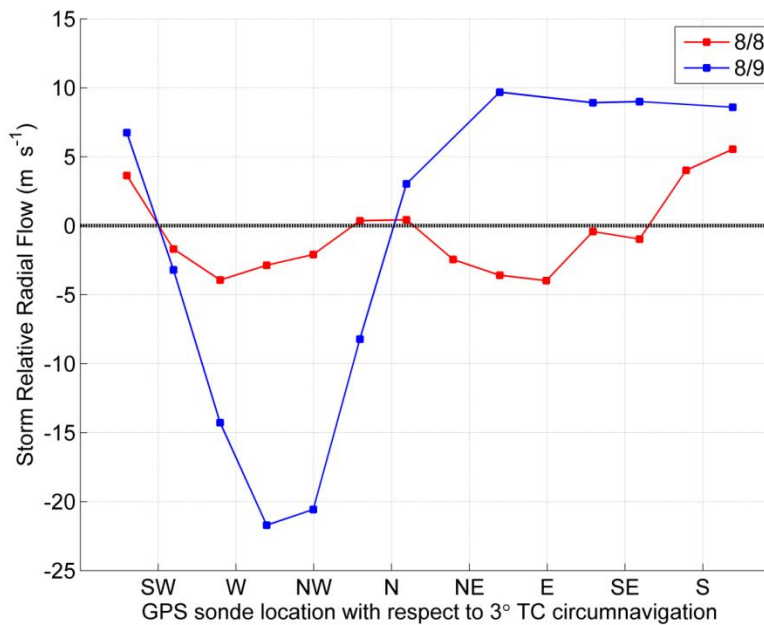


(b)

Figure 33. GPS sonde measured storm relative wind flow at 200 hPa during the G-IV missions on (a) 8 August and (b) 9 August. Wind speeds are in knots. The red circles denote Felicia's center of circulation.



(a)



(b)

Figure 34. Storm relative tangential (a) and radial flow (b) at 250 hPa. In (a), positive tangential flow values are cyclonic and negative values are anticyclonic. In (b), positive values are outflow and negative values are radial inflow. Each data point describes the deployment position on the circumnavigated ring starting at the SW quadrant and rotating clockwise. Red depicts the observations on the 8th while blue shows the observations during the 9th.

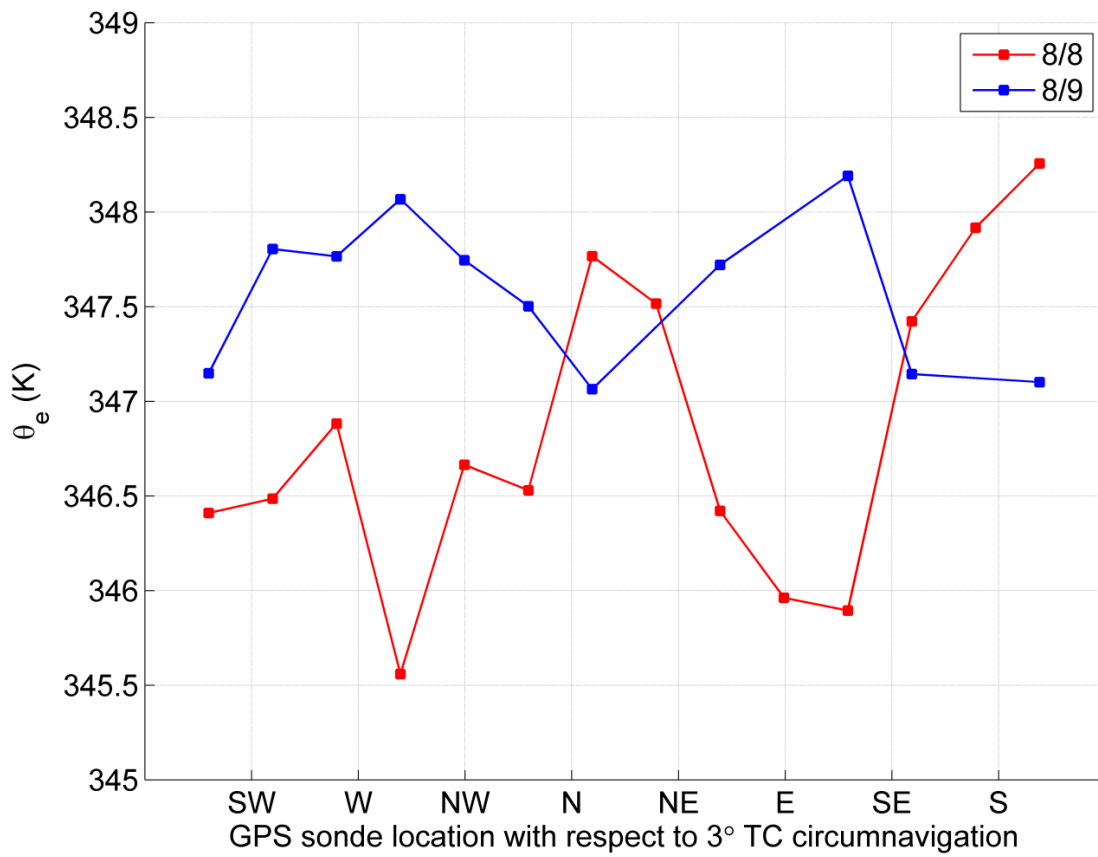


Figure 35. θ_e at 250 hPa. As in previous figures, each data point describes the deployment position on the circumnavigated ring starting at the SW quadrant and rotating clockwise.

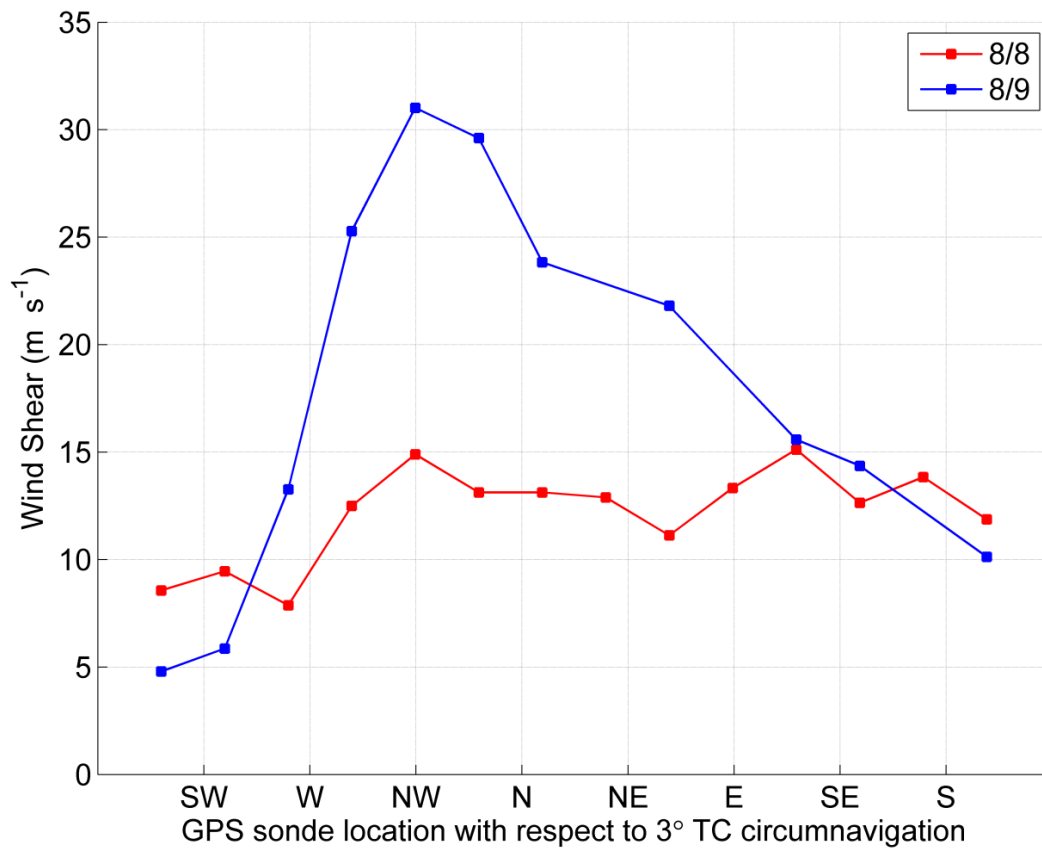


Figure 36. VWS from 850 – 225 hPa in m s^{-1} . As in previous figures, each data point describes the deployment position on the circumnavigated ring, starting at the SW quadrant and rotating clockwise.

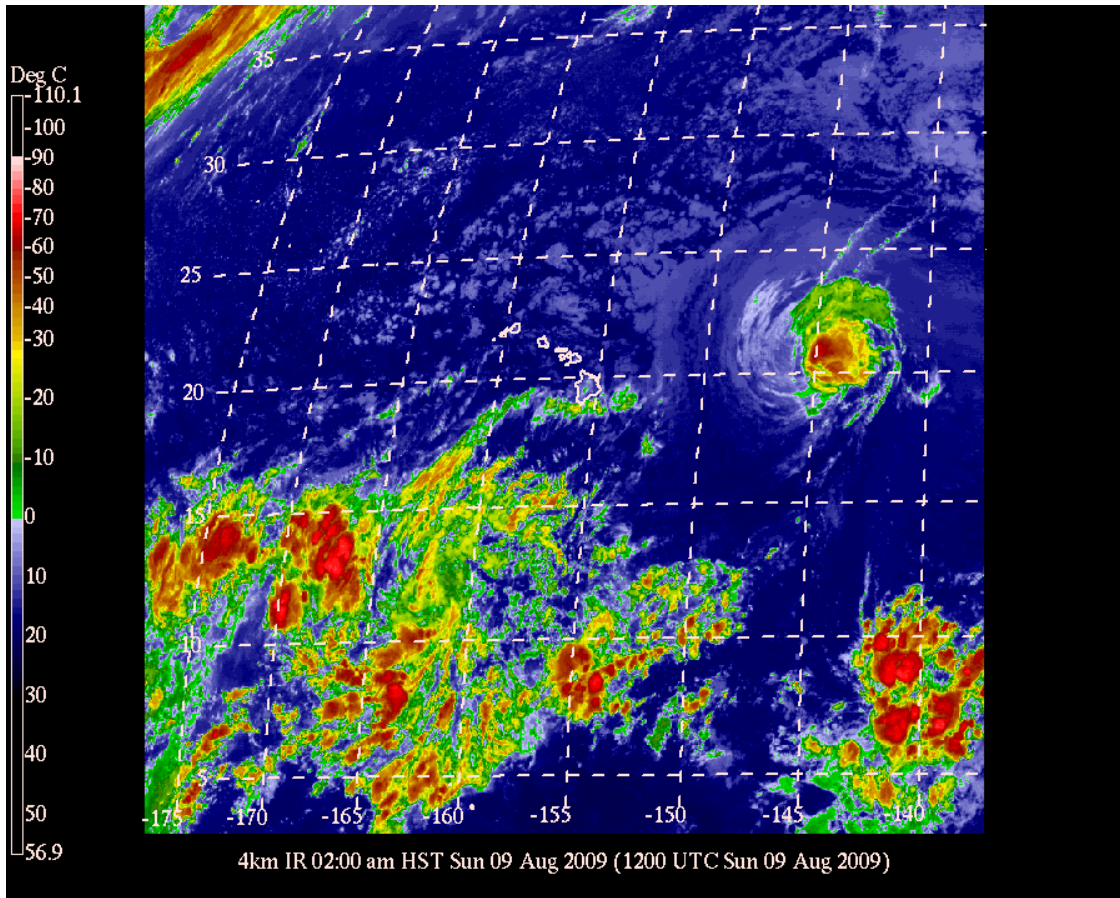


Figure 37. IR satellite image of Hurricane Felicia at 1200 UTC 9 August.

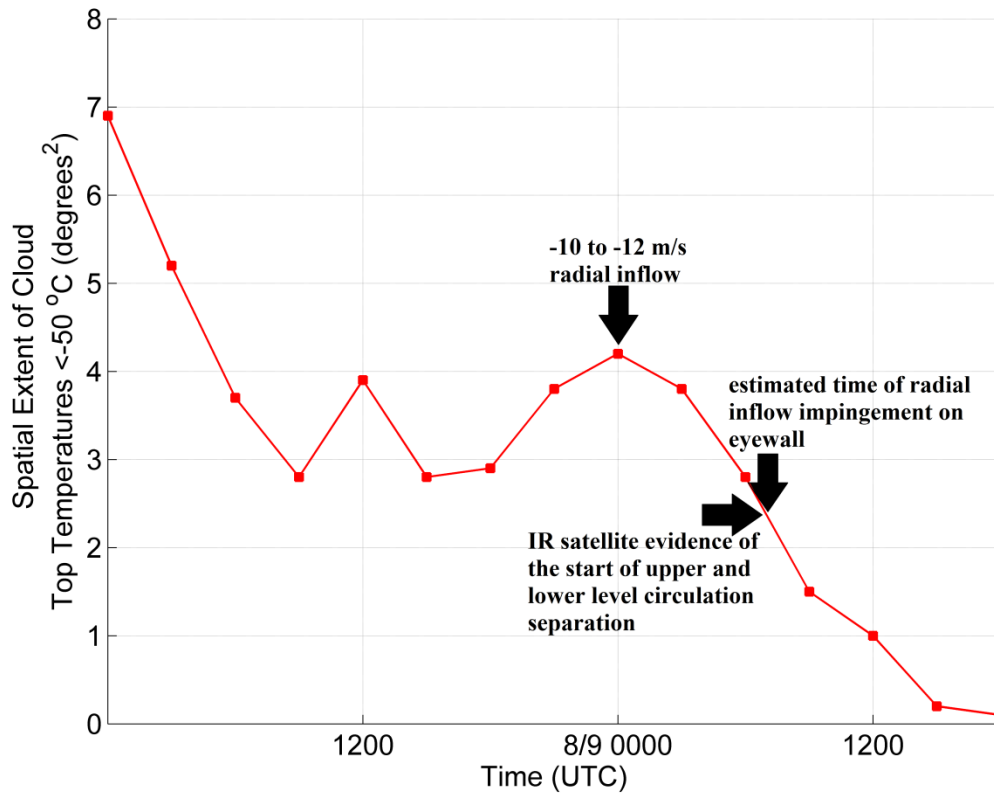
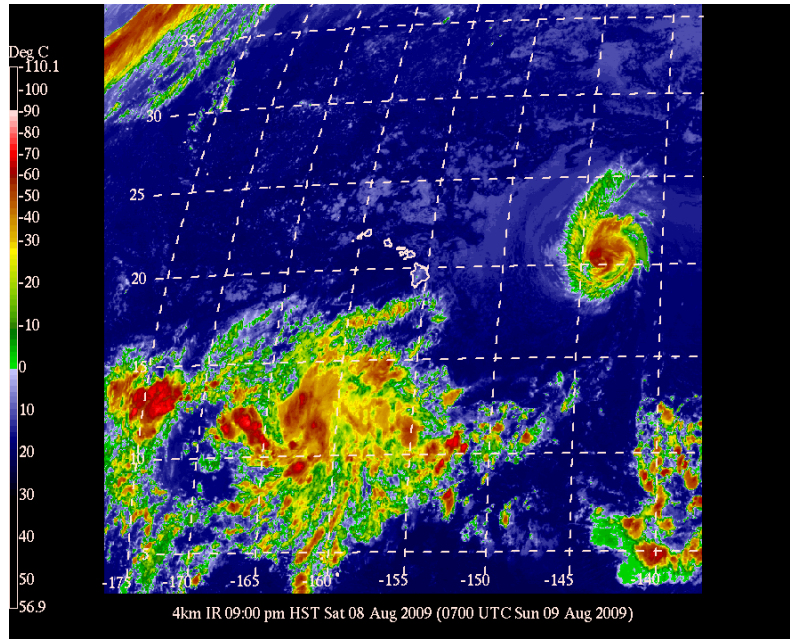
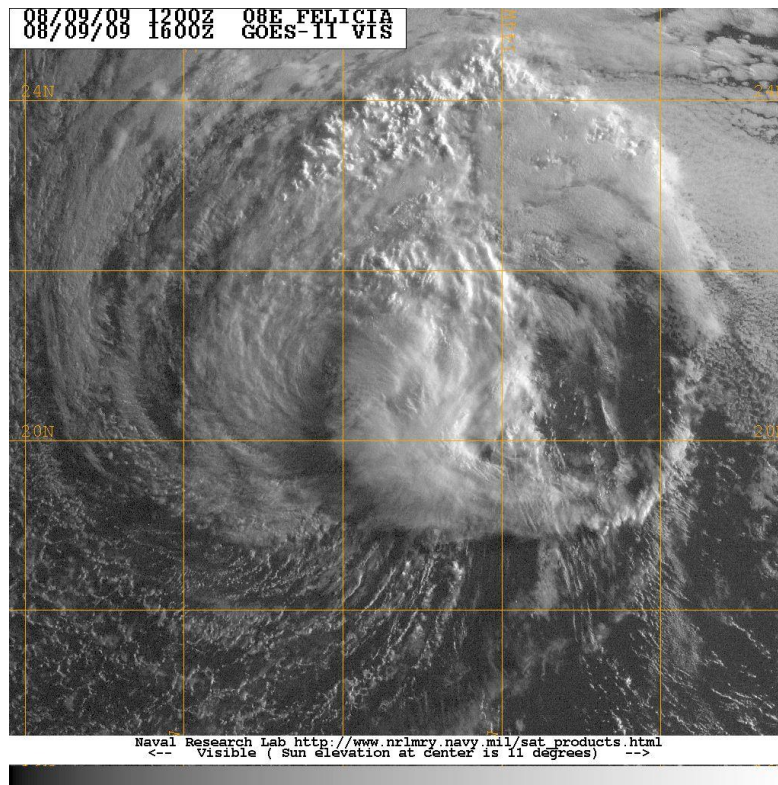


Figure 38. Evolution of spatial extent of cloud top temperatures less than -50°C (degrees²) associated with Felicia from 0000 UTC 8 August through 1800 UTC 9 August.



(a)



(b)

Figure 39. IR satellite imagery of Hurricane Felicia at (a) 0900 UTC 9 August and (b) visible satellite imagery of Felicia at 1600 UTC 9 August.

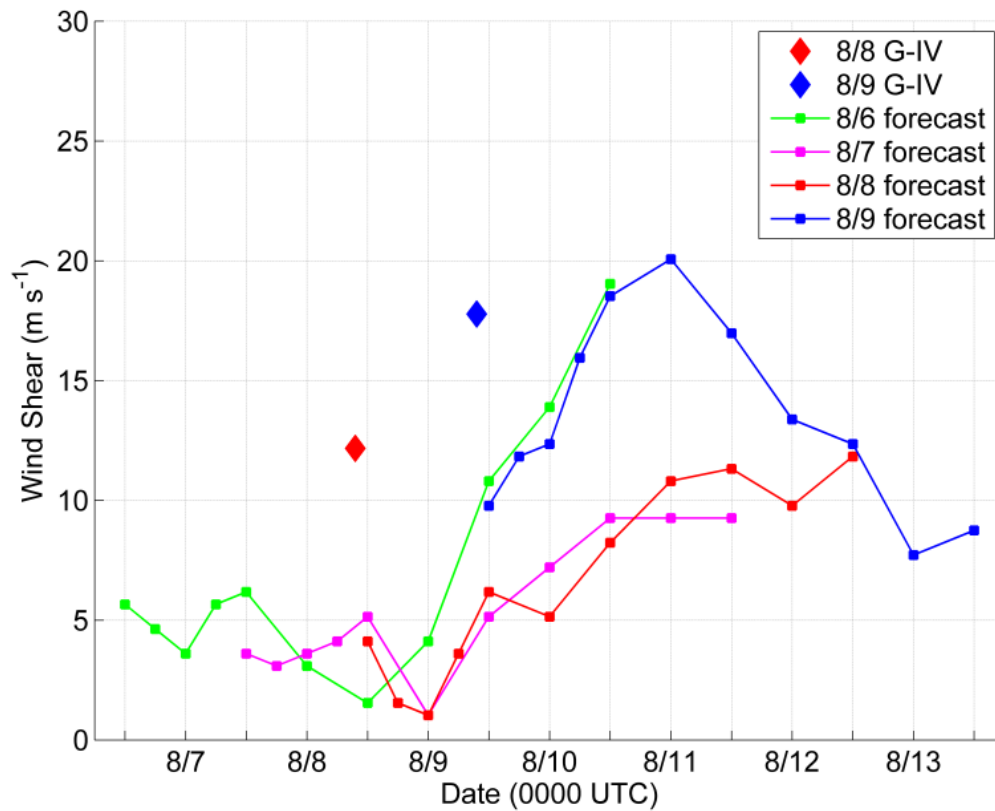


Figure 40. SHIPS 0-96 h operational shear forecasts for 6-9 August at 1200 UTC. The GPS sonde computed 8 and 9 August 850-225 hPa storm relative shear values, averaged around the 3-degree circumnavigation and centered at 1000 UTC, are shown in red and blue diamonds, respectively. All values are in m s^{-1} .

REFERENCES

- Avila, L. A., 1998: Forecasting tropical cyclone intensity changes: An operational challenge. Preprints, Symp. on Tropical Cyclone Intensity Change, Phoenix, AZ, *Amer. Meteor. Soc.*, 1–3.
- Barnes, G. M., E. J. Zipser, D. Jorgensen, and F. Marks, 1983: Mesoscale and convective structure of a hurricane rainband. *J. Atmos. Sci.*, **40**, 2125–2137.
- _____, 2008: Atypical thermodynamic profiles in hurricanes. *Mon. Wea. Rev.*, **136**, 631–643.
- Black, M. L., J. F. Gamache, F. D. Marks Jr., C. E. Samsury, and H. E. Willoughby, 2002: Eastern Pacific Hurricanes Jimena of 1991 and Olivia of 1994: The effect of vertical shear on structure and intensity. *Mon. Wea. Rev.*, **130**, 2291–2312.
- Black, P. G., and R. A. Anthes, 1971: On the asymmetric structure of the tropical cyclone outflow layer. *J. Atmos. Sci.*, **28**, 1348–1366.
- Bogner, P. B., G. M. Barnes, and J. L. Franklin, 2000: Conditional instability and shear for six hurricanes over the Atlantic Ocean. *Wea. Forecasting*, **15**, 192–207.
- Bolton, D., 1980: The computation of equivalent potential temperature. *Mon. Wea. Rev.*, **108**, 1046–1053.
- Bosart, L. F., W. E. Bracken, J. Molinari, C. S. Velden, and P. G. Black, 2000: Environmental influences on the rapid intensification of Hurricane Opal (1995) over the Gulf of Mexico. *Mon. Wea. Rev.*, **128**, 322–352.
- Braun, S. A., 2010: Reevaluating the role of the Saharan air layer in Atlantic tropical cyclogenesis and evolution. *Mon. Wea. Rev.*, **138**, 2007–2037.
- _____, J. A. Sippel, and D. S. Nolan, 2012: The impact of dry midlevel air on hurricane intensity in idealized simulations with no mean flow. *J. Atmos. Sci.*, **69**, 236–257.
- Burpee, R. W., S. D. Aberson, J. L. Franklin, S. J. Lord, and R. E. Tuleya, 1996: The impact of Omega Dropwindsondes on operational hurricane track forecast Models. *Bull. Amer. Meteor. Soc.*, **77**, 925–933.
- Chen, G., and L. F. Chou, 1994: An investigation of cold vortices in the upper troposphere over the western North Pacific during the warm season. *Mon. Wea. Rev.*, **122**, 1436–1448.

- Cione, J. J., and E. W. Uhlhorn, 2003: Sea surface temperature variability in Hurricanes: Implications with respect to intensity change. *Mon. Wea. Rev.*, **131**, 1783–1796.
- Cooperative Institute for Meteorological Satellite Studies and University of Wisconsin-Madison. (2012). CIMSS Tropical Cyclones Data Archive. Retrieved from <http://tropic.ssec.wisc.edu/archive/>
- Dare, R. A., J. L. McBride, 2011: The Threshold sea surface temperature condition for tropical cyclogenesis. *J. Climate*, **24**, 4570–4576.
- DeMaria, M., J-J. Baik, and J. Kaplan, 1993: Upper-level eddy angular momentum fluxes and tropical cyclone intensity change. *J. Atmos. Sci.*, **50**, 1133–1147.
- _____, and J. Kaplan, 1994: A statistical hurricane intensity prediction scheme (SHIPS) for the Atlantic basin. *Wea. Forecasting*, **9**, 209–220.
- _____, 1996: The effect of vertical shear on tropical cyclone intensity change. *J. Atmos. Sci.*, **53**, 2076–2088.
- Dengler, K., 1997: A numerical study of the effects of land proximity and changes in sea surface temperature on hurricane tracks. *Quart. J. Roy. Meteor. Soc.*, **123**, 1307–1321.
- Dolling, K. P., 2012: The Evolution of Hurricane Humberto (2001). Ph.D. dissertation, University of Hawaii at Manoa, Honolulu, HI, 000 pp.
- _____, and G. M. Barnes, 2012: The creation of a high equivalent potential temperature reservoir in Tropical Storm Humberto (2001) and its possible role in storm deepening. *Mon. Wea. Rev.*, **140**, 492–505.
- _____, and G. M. Barnes, 2014: The Evolution of Hurricane Humberto (2001). *J. Atmos. Sci.*, **71**, 1276–1291.
- Dunion, J. P., and C. S. Velden, 2004: The impact of the Saharan air layer on Atlantic tropical cyclone activity. *Bull. Amer. Meteor. Soc.*, **85**, 353–365.
- Emanuel, K. A., 1986: An air-sea interaction theory for tropical cyclones. Part I: Steady state maintenance. *J. Atmos. Sci.*, **43**, 585–605.
- Frank, F. M., 1977: The structure and energetics of the tropical cyclone I. Storm structure. *Mon. Wea. Rev.*, **105**, 1119–1135.

- Frank, W. M., and E. A. Ritchie, 2001: Effects of vertical wind shear on the intensity and structure of numerically simulated hurricanes. *Mon. Wea. Rev.*, **129**, 2249–2269.
- Franklin, J. L., 1990: Dropwindsonde observations of the environmental flow of hurricane Josephine (1984): Relationships to vortex motion. *Mon Wea. Rev.*, **118**, 2732-2744.
- Gallina, G., and C. Velden, 2002: Environmental vertical wind shear and tropical cyclone intensity change utilizing enhanced satellite derived wind information. Preprints, *25th Conf. on Hurricanes and Tropical Meteorology*, San Diego, CA, Amer. Meteor. Soc., 172-173.
- Gray, W. M., 1968: Global view of the origin of tropical disturbances and storms. *Mon. Wea. Rev.*, **96**, 669–700.
- _____, 1989: Summary of ONR sponsored tropical cyclone motion research and future plans. Appendix D of Technical Report NPS 63-89-002, Naval Postgraduate School (R.L. Elsberry, Ed.), Monterey, CA 93943, 68-79.
- Hock, T. F., and J. L. Franklin, 1999: The NCAR GPS Dropwindsonde. *Bull. Amer. Meteor. Soc.*, **80**, 407–420.
- Holland, G. J., and R. T. Merrill, 1984: On the dynamics of tropical cyclone structural changes. *Quart. J. Roy. Meteor. Soc.*, **110**, 723-745.
- Kimberlain, T. B., R. D. Knabb, and D. Wroe, 2010: Tropical Cyclone Report: Hurricane Felicia (EP082009). Retrieved from http://www.nhc.noaa.gov/pdf/TCR-EP082009_Felicia.pdf
- Malkus, J. S., and H. Riehl, 1960: On the dynamics and energy transformation in steady-state hurricanes. *Tellus*, **12**, 1-20.
- Marin, J., D. Raymond, and G. Raga, 2009: Intensification of tropical cyclones in the GFS model. *Atmos. Chem. Phys.*, **9**, 1407-1417.
- Martin, C., 2007: ASPEN User Manual. NCAR, 61pp. {Available online at <http://www.eol.ucar.edu/isf/facilities/software/aspn/ASPEN%20Manual.pdf>}
- McBride, J., and R. Zehr, 1981: Observational analysis of tropical cyclone formation. Part II: Comparison of non-developing versus developing systems. *J. Atmos. Sci.*, **38**, 1132-1151.

- Miller, B. I., 1958: On the maximum intensity of hurricanes. *J. Meteor.*, **15**, 184–195.
- _____, 1964: A study of the filling of Hurricane Donna (1960) over land. *Mon. Wea. Rev.*, **9**, 389-406.
- NOAA_OI_SST_V2 data provided by the NOAA/OAR/ESRL PSD, Boulder, Colorado, USA, <http://www.esrl.noaa.gov/psd/>
- Nolan, D. S., 2007: What is the trigger for tropical cyclogenesis? *Aust. Meteor. Mag.*, **56**, 241–266.
- Palmén, E. H., 1948: On the formation and structure of tropical cyclones. *Geophysics*, **3**, 26–38.
- Patla, J. E., D. Stevens, and G. M. Barnes, 2009: A conceptual model for the influence of TUTT cells on tropical cyclone motion in the Northwest Pacific Ocean. *Wea. Forecasting*, **24**, 1215–1235.
- Powell, M. D., 1990: Boundary layer structure and dynamics in outer hurricane rainbands. Part II: Downdraft modification and mixed layer recovery. *Mon. Wea. Rev.*, **118**, 918–938.
- _____, S. H. Houston, L. R. Amat, and N. Morisseau-Leroy, 1998: The HRD real-time hurricane wind analysis system. *J. Wind Engineer. and Indust. Aerodyn.* **77&78**, 53-64
- Reynolds, R. W., 1988: A real-time global sea surface temperature analysis. *J. Climate*, **1**, 75-86.
- _____, D. C. Marsico, 1993: An improved real-time global sea surface temperature analysis. *J. Climate*, **6**, 114-119.
- Riemer, M., M. Montgomery, and M. Nicholls, 2010: A new paradigm for intensity modification of tropical cyclones: Thermodynamic impact of vertical wind shear on the inflow layer. *Atmos. Chem. Phys.*, **10**, 3163-3188.
- Rogers, R., and Coauthors, 2006: The intensity forecasting experiment: A NOAA multiyear field program for improving tropical cyclone intensity forecasts. *Bull. Amer. Meteor. Soc.*, **87**, 1523–1537.

- Sadler, J. C., 1967: The tropical upper tropospheric trough as a secondary source of typhoons and primary source of trade wind disturbances. *Hawaii Institute of Geophysics*, Rep. **67-12**, 103 pp.
- _____, 1975: The upper tropospheric circulation over the global tropics. Dept. of Meteorology Rep. UHMET-75-05, University of Hawaii, Honolulu, HI, 16 pp.
- _____, 1976: A role of the tropical upper tropospheric trough in early season typhoon development. *Mon. Wea. Rev.*, **104**, 1266–1278.
- _____, 1978: Mid-season typhoon development and intensity changes and the tropical upper tropospheric trough. *Mon. Wea. Rev.*, **106**, 1137–1152.
- Saha, S., et al. 2010. *NCEP Climate Forecast System Reanalysis (CFSR) 6-hourly Products, January 1979 to December 2010*. Research data archive at the National Center for Atmospheric Research, Computational and Information Systems Laboratory. <http://dx.doi.org/10.5065/D69K487J>. Accessed 23 Sept 2014.
- Simpson R., and H. Riehl, 1958: Mid-tropospheric ventilation as a constraint on hurricane development and maintenance. Preprints, *Tech. Conf. on Hurricanes*, Miami Beach, FL, Amer. Meteor. Soc., D4-1-D4-10.
- Sippel, J. A., S. A. Braun, F. Zhang, and Y. Weng, 2013: Ensemble Kalman filter assimilation of simulated HIWRAP Doppler velocity data in a hurricane. *Mon. Wea. Rev.*, **141**, 2683–2704.
- Shieh, O. H., M. Fiorino, M. E. Kucas, and B. Wang, 2013: Extreme rapid intensification of Typhoon Vicente (2012) in the South China Sea. *Wea. Forecasting*, **28**, 1578–1587.
- Shu, S. J., and L. Wu, 2009: Analysis of the influence of the Saharan air layer on tropical cyclone intensity using AIRS/Aqua data. *Geophys. Res. Lett.*, **36**, L09809, doi:10.1029/2009GL037634.
- Tang, B., and K. Emanuel, 2012: A ventilation index for tropical cyclones. *Bull. Amer. Meteor. Soc.*, **93**, 1901–1912.
- Velden C. S., and J. Sears, 2014: Computing deep-tropospheric vertical wind shear analyses for tropical cyclone applications: Does the methodology matter?. *Wea. Forecasting*, **29**, 1169–1180.

- Wang, J., 2005: Evaluation of the dropsonde humidity sensor using data from DYCOMS-II and IHOP_2002. *J. Atmos. Oceanic. Technol.*, **22**, 247-257.
- Wu, L., 2007: Impact of Saharan air layer on hurricane peak intensity. *Geophys. Res. Lett.*, **34**, L09802, doi:10.1029/2007GL029564.
- Zehr, R., 1992: Tropical cyclogenesis in the western north Pacific. NOAA Tech. Rep. NESDIS 61, 181 pp.
- Zhang, C., 1993: Large-scale variability of atmospheric deep convection in relation to sea surface temperature in the tropics. *J. Climate*, **6**, 1898–1913.